

**Laser development and stabilization for the spaceborne
interferometric gravitational wave detector LISA**

Vom Fachbereich Physik der Universität Hannover
zur Erlangung des Grades

Doktor der Naturwissenschaften
– Dr. rer. nat. –

genehmigte Dissertation

von
Dipl.-Phys. Michael Tröbs, M. Phil.

geboren am 01.03.1976 in Hannover

2005

Referent: Prof. Dr. Karsten Danzmann, Universität Hannover
Korreferent: PD. Dr. Holger Lubatschowski, Universität Hannover
Tag der Promotion: 09.02.2005

Kurzzusammenfassung

Michael Tröbs

Laserentwicklung und Stabilisierung für den weltraumgestützten interferometrischen Gravitationswellendetektor LISA

Der weltraumgestützte, interferometrische Gravitationswellendetektor LISA (Laser Interferometer Space Antenna) soll als Ergänzung zu erdgebundenen Detektoren, die im Frequenzbereich oberhalb von 10 Hz arbeiten, Gravitationswellen mit Frequenzen von 0.1 mHz bis 1 Hz detektieren. Dazu benötigt LISA in diesem Frequenzbereich extrem rauscharme, einfrequente Laser mit 1 W polarisierter Ausgangsleistung im transversalen Grundmode. Derartige Laser und Messgeräte zur Rauschcharakterisierung standen nicht zur Verfügung und die Eigenschaften geeigneter Laserkandidaten im LISA Frequenzbereich waren unzureichend bekannt. Deshalb wurden spektrale Rauschdichten aus digitalisierten Zeitserien berechnet und es wurde ein neuartiger Algorithmus entwickelt, der besonders gut für große Datenmengen und die Benutzung einer logarithmischen Frequenzachse geeignet ist, wie hier erforderlich war.

Zwei Laserkonzepte sind für LISA geeignet: ein einstufiger Oszillator hoher Leistung oder ein leistungschwächerer Oszillator, der mit einem Faserverstärker nachverstärkt wird. Ein leistungsschwacher Faserlaser wurde untersucht. Sein Potenzial für LISA konnte erstmals gezeigt werden und weitere Untersuchungen zu Leistungsskalierbarkeit, daraus resultierende Rauscheigenschaften und Frequenzaktuatorbandbreite wurden als notwendige weitere Schritte identifiziert.

Die Rauscheigenschaften von diodengepumpten, nichtplanaren Ringresonatoren (NPROs), die erfolgreich in erdgebundenen Gravitationswellendetektoren eingesetzt werden, waren im LISA Frequenzbereich nicht hinreichend bekannt und wurden untersucht. Erstmals wurden im Rahmen dieser Arbeit ein Laserdemonstrator basierend auf einem einstufigen, leistungsstarken NPRO entwickelt und ein Ytterbium-dotierter Faserverstärker, der von einem leistungsschwachen NPRO geseedet wird, im LISA Frequenzbereich charakterisiert. Beide lieferten einfrequente, polarisierte Strahlung im transversalen Grundmode und zeigten ihre Eignung für LISA.

In beiden Fällen war eine aktive Stabilisierung der Leistung erforderlich. Die Ausgangsleistung des einstufigen Laserdemonstrators wurde stabilisiert und mehrere Rauschquellen wurden erstmals untersucht und charakterisiert. Die wichtigsten waren die Temperaturabhängigkeit der Fotodiodeeffizienz, die Stabilität der Referenz und die Temperaturabhängigkeit der Reflektivität der Strahlteiler zur Leistungsdetektion. Erstmals wurden die LISA Anforderungen im gesamten Frequenzbereich erfüllt. Die gemessenen relativen Leistungsfluktuationen sind die kleinsten bisher veröffentlichten Werte für diesen Frequenzbereich.

Auch die Frequenz des einstufigen Laserdemonstrators wurde stabilisiert. Sie wurde an die Resonanzfrequenz eines optischen Resonators gekoppelt. Durch Vergleich mit einem anderen, auf eine unabhängige Referenz stabilisierten Laser, wurden die verbleibenden Frequenzfluktuationen nach oben abgeschätzt. Neben anderen Rauschquellen wurden die Abhängigkeiten der Referenzfrequenz von Umgebungstemperatur und Leistung im Referenzresonator charakterisiert. Die LISA Anforderungen wurden für Frequenzen oberhalb von 3 mHz erreicht, für Frequenzen bis 1 mHz lag das Frequenzrauschen um bis zu einem Faktor 3 oberhalb der Anforderungen. Die gemessenen Frequenzfluktuationen gehören zu den kleinsten weltweit gemessenen. Als limitierende Rauschquelle konnten Fehlersignaldrifts im Referenzsystem identifiziert werden.

Schlagnworte: LISA, Leistungsstabilisierung, Frequenzstabilisierung

Abstract

Michael Tröbs

Laser development and stabilization for the spaceborne interferometric gravitational wave detector LISA

The spaceborne, gravitational wave detector LISA (Laser Interferometer Space Antenna) will, in addition to ground-based detectors that operate at frequencies above 50 Hz, detect gravitational waves with frequencies from 0.1 mHz to 1 Hz. For this purpose, LISA requires extremely low-noise, single-frequency lasers emitting 1 W of polarized output power in the fundamental transverse mode. Such lasers and measurement equipment for noise characterization did not exist and the properties of suitable laser candidates in the LISA frequency range were not sufficiently known. Hence, spectral densities were calculated from digitized time series, and a novel algorithm was developed that is especially well-suited for large amounts of data and usage of a logarithmically scaled frequency axis, as was necessary in this work.

Two laser concepts are well-suited for LISA: a single-stage, high-power oscillator, or a fiber amplifier seeded by a low-power oscillator. A low-power fiber laser was investigated and its potential for LISA could be shown for the first time. It could also be shown that further investigations regarding power scalability, the resulting noise properties, and frequency actuator bandwidth are necessary.

The noise properties of nonplanar ring oscillators (NPROs) that are successfully used in ground-based gravitational wave detectors, were not sufficiently known in the LISA frequency range. They were investigated and, for the first time, a laser demonstrator based on a single-stage high-power NPRO was developed, its frequency- and power-noise measured, and an Ytterbium-doped fiber amplifier seeded by a low-power NPRO was characterized in the LISA frequency range. Both delivered single-frequency polarized radiation in fundamental transverse mode and showed their suitability for LISA.

In both cases, an active power stabilization was necessary. The output power of the single-stage laser demonstrator was stabilized, and a number of noise sources were for the first time investigated and characterized. The most important were the stability of the reference and the temperature dependency of both the photodiode efficiency and the beam splitter reflectivity. For the first time, the LISA requirements were met in the complete frequency range. The measured relative power fluctuations are the smallest published values for this frequency range.

The frequency of the single-stage laser demonstrator was stabilized. It was locked to a resonance frequency of an optical resonator, and an upper limit for its residual frequency fluctuations was found using beat measurements with a reference laser that was stabilized to an independent optical resonator. Among other noise sources the dependency of reference frequency on ambient air temperature and power in the reference cavity were characterized. The LISA requirement was met for frequencies above 3 mHz. For frequencies down to 1 mHz, the frequency fluctuations were above the requirements, up to a factor of 3. The measured frequency fluctuations are among the smallest that have been measured, world-wide. As limiting noise source, error signal drifts in the reference laser system could be identified.

Key words: LISA, power stabilization, frequency stabilization

Contents

List of Abbreviations	vii
List of Figures	viii
List of Tables	x
1. Introduction	1
2. Signal and noise characterization in the frequency domain	3
2.1. Existing methods	4
2.2. Improved method	6
2.3. Conclusions	7
3. Light sources for LISA	9
3.1. Requirements and possible laser designs	9
3.2. The first laser demonstrator for LISA	11
3.2.1. Setup	11
3.2.2. Output power and polarization	14
3.2.3. Power and frequency actuators	14
3.2.4. Power fluctuations	17
3.2.5. Frequency fluctuations	17
3.2.6. Conclusions	19
3.3. Ytterbium-doped fiber amplifier	21
3.3.1. Setup	22
3.3.2. Power fluctuations	23
3.3.3. Frequency fluctuations	24
3.3.4. Power and frequency actuators	29
3.3.5. Conclusions	34
3.4. Low-power distributed-feedback fiber laser	35
3.4.1. Setup, output power, and polarization	35
3.4.2. Frequency stabilization	36
3.4.3. Frequency actuators	39
3.4.4. Power fluctuations	40
3.4.5. Frequency fluctuations	42
3.4.6. Conclusions	43

3.5. Discussion	45
4. Power stabilization	47
4.1. Experiments	48
4.2. Reference characterization	50
4.3. Results	53
4.4. Noise sources	56
4.4.1. Shot noise	58
4.4.2. Dark current	58
4.4.3. Temperature dependent photo detection efficiency	59
4.4.4. Position dependent photo detection efficiency	61
4.4.5. Temperature dependent beam splitting ratio	67
4.5. Conclusions	69
5. Frequency stabilization	71
5.1. Experiments	72
5.2. Results	74
5.3. Noise sources	75
5.3.1. Temperature fluctuations	76
5.3.2. Power fluctuations	76
5.3.3. Shot noise	80
5.3.4. Error signal offsets	81
5.3.5. Residual amplitude modulation	82
5.4. Conclusions	83
6. Summary and outlook	85
Bibliography	89
A. Improving spectral estimation on logarithmic frequency axes	97
A.1. The WOSA method	99
A.2. Fourier frequencies, frequency resolutions, and bins	100
A.3. Windowing and overlap of segments	103
A.4. Non-integer frequency bin numbers	104
A.5. Calibration of spectral estimates	105
A.6. Aliasing for small frequency bins	106
A.7. Algorithm summary	108
B. Basic properties, design, and characterization of control loops	111
B.1. Basics	111
B.1.1. Transfer functions	111
B.1.2. Schematic representation of a control loop	111
B.1.3. Noise transfer and noise suppression in control loops	112
B.1.4. Bode diagrams and control loop stability	113
B.2. Control loop design	114

B.2.1. Actuator choice and calibration	116
B.2.2. Error signal calibration	116
B.2.3. Loop filter design from little information	117
B.2.4. Transfer function measurement	118
B.2.5. Design procedure for optimized loop filters	119
B.3. Control loop characterization	120
B.3.1. Open loop gain measurement	121
B.3.2. In-loop noise as lower noise limit	122
B.3.3. Out-of-loop noise as upper noise limit	122
Publications	123
Curriculum vitae	125

List of Abbreviations

A/D	Analog/Digital
AI	Adder Input
AOM	Acousto-Optical Modulator
AP	Actuator Point
ASE	Amplified Spontaneous Emission
BS	Beam Splitter
DBR	Distributed Bragg Reflector
DFB	Distributed feedback
DFT	Discrete Fourier Transform
EOM	Electro-optical modulator
ESA	European space agency
EP	Error Point
FWHM	Full Width Half Maximum
Ge	Germanium
HSL	High-Stability Laser
HWP	Half Wave Plate
IBS	Ion Beam Sputtering
InGaAs	Indium Gallium Arsenide
LISA	Laser Interferometer Space Antenna
LO	Local Oscillator
LPSD	Linear frequency axis Power Spectral Density
MOPA	Master Oscillator Power Amplifier
NASA	National Aeronautics and Space Administration
NPRO	Nonplanar Ring Oscillator
NTC	Negative Temperature Coefficient
PBS	Polarizing Beam Splitter
PD	photodiode
PID	Proportional Integrator Differentiator
PZT	Piezo-electric Transducer
QWP	Quarter Wave Plate
RAM	Residual Amplitude Modulation
RC	Reference Cavity
Si	Silicon
TEC	thermo-electric cooler
ULE	Ultra Low Expansion glass
WOSA	Windowed Overlapped Segmented Average

List of Figures

2.1. Spectral density estimate obtained by WOSA method	5
2.2. Spectral density estimate obtained with two frequency resolutions	5
2.3. Spectral density estimate obtained by new LPSD method	6
3.1. Laser crystal holder of the LISA laser demonstrator	12
3.2. Schematic setup of the LISA laser demonstrator	13
3.3. LISA laser demonstrator with open top cover	14
3.4. Pump module for the LISA laser demonstrator	15
3.5. LISA laser demonstrator output power versus pump power	16
3.6. LISA laser demonstrator thermal frequency tuning characteristics	17
3.7. Pump power transfer to laser frequency	18
3.8. NPRO free-running power fluctuations in LISA measurement window	19
3.9. Free-running frequency fluctuations of NPROs	20
3.10. Fiber amplifier setup	22
3.11. Relative power fluctuations of amplifier, seed laser, and pump diode	24
3.12. Phase noise measurement setup	25
3.13. Low-frequency phase noise and limiting noise sources	27
3.14. High-frequency phase noise in fiber amplifier	28
3.15. Combined phase noise measurements scaled as frequency noise	29
3.16. Seed laser power transfer to amplifier output power	30
3.17. Pump power transfer to amplifier output power	32
3.18. Power actuator transfer functions	33
3.19. Measured PZT frequency tuning efficiency	34
3.20. Koheras Adjustik turn-key DFB fiber laser	36
3.21. Frequency stabilization setup for the distributed-feedback fiber laser	37
3.22. DFB laser frequency fluctuations measured at the error point	38
3.23. Thermal frequency tuning of the DFB fiber laser	40
3.24. PZT actuator characteristics of the DFB fiber laser	41
3.25. Relative power fluctuations of the DFB fiber laser	41
3.26. Free-running frequency fluctuations of the DFB fiber laser	43
4.1. Power stabilization setup of the LISA laser demonstrator	49
4.2. Voltage reference internal noise measurement setup	51
4.3. Voltage reference internal noise results	51
4.4. Laboratory temperature fluctuations	52

4.5.	Relative power fluctuations of LISA laser demonstrator	53
4.6.	Relative power fluctuations under different operating conditions	55
4.7.	Measured temperature fluctuations at the power stabilization setup	56
4.8.	Relative power fluctuations achieved with different photodiodes	57
4.9.	Dark noise of Si and InGaAs photodetectors	58
4.10.	InGaAs photodiode temperature noise projection to signal noise	61
4.11.	Spatial efficiency distribution of photodiodes	64
4.12.	Horizontal scan of Ge1 photodiode efficiency through center	65
4.13.	Relative photodiode signal change for different beam positions	66
4.14.	Beam sampling power fluctuations due to temperature fluctuations	69
4.15.	Summary of limiting noise sources in power stabilization	70
5.1.	Combined power- and frequency stabilization setup	72
5.2.	Frequency fluctuations of the LISA laser demonstrator	75
5.3.	Temperature fluctuations projection on frequency fluctuations	77
5.4.	Resonance frequency shift of cavity 1	78
5.5.	Beat frequency for varying optical powers transmitted through cavity 1	79
5.6.	Laser power fluctuations projected on frequency fluctuations	80
5.7.	Contributions of error signal offsets to frequency fluctuations	81
5.8.	Effect of EOM temperature drift on beat frequency	82
5.9.	Summary of limiting noise sources in frequency stabilization	83
A.1.	Segmentation of the data stream	99
A.2.	Non-overlapping segmented data stream with window	103
A.3.	Data stream with overlapping segments and window	104
A.4.	Hanning window frequency response magnitude	105
A.5.	Spectrum estimate obtained by WOSA method	107
A.6.	Spectrum estimate obtained with two different resolutions	107
A.7.	Spectrum estimate obtained by new LPSD method	108
B.1.	Schematic representation of a control loop	112
B.2.	Different noise sources in a control loop	112
B.3.	Bode plot of a frequency stabilization open loop gain	114
B.4.	Estimation of error signal slope	117
B.5.	Measuring the frequency dependent error signal slope	119
B.6.	Measured transfer function of the control path	120
B.7.	Optimized open loop gain design	121
B.8.	Scheme used to measure the open loop gain of a control loop	122

List of Tables

3.1. Requirements for the LISA laser system	11
3.2. Required and measured parameters for the LISA laser demonstrator . . .	21
3.3. Required and measured parameters for fiber amplifier	35
3.4. Required and measured parameters for low-power DFB fiber laser	44
3.5. Required and measured parameters for the LISA light source	45
4.1. Photodiode summary for power stabilization	49
4.2. Temperature coefficients for voltage reference AD587	52
4.3. Magnitudes of relative photodiode efficiency temperature coefficients . . .	60
4.4. Comparison of spatial photodiode inhomogeneity measurements	62
4.5. Temperature coefficients for beam samplers	67
5.1. Finesse measurements at optical cavities	73
A.1. Commonly used symbols	98
A.2. Naming convention for spectra	105
B.1. Elements commonly employed in control theory	115

1. Introduction

In the beginning of astronomy, the visible part of the electro-magnetic spectrum was used to observe the sky. Today it is observed also in the radio-frequency, infrared, ultraviolet, X-ray, and gamma ray range. With each new wavelength range that was used for astronomy, more valuable insight into the universe was gained. The radio telescope at Arecibo (Puerto Rico, West Indies) for example, provided first evidence for the existence of gravitational waves (Nobel prize in 1993 awarded to Russell A. Hulse and Joseph H. Taylor, Jr). The direct detection of gravitational waves will open a completely new window to further investigate the universe.

Gravitational waves have been predicted by Einstein in his general theory of relativity, published in 1915. They are emitted by accelerated masses in analogy to electromagnetic radiation emitted by accelerated electrical charges. A gravitational wave alternately stretches and shrinks distances, though on an extremely small scale – by a factor of 10^{-21} for very strong sources. That's roughly equivalent to measuring a change the size of an atom in the distance from the Sun to Earth.

Currently, four earth-based interferometric gravitational wave detectors are being commissioned: GEO600, LIGO, TAMA300, and VIRGO. In principle, they are Michelson interferometers that use additional techniques to improve the sensitivity (Black and Gutenkunst, 2003).

The Laser Interferometer Space Antenna (LISA) will be a space-based Michelson interferometer with 5 million km armlength. It will comprise three satellites in heliocentric orbits. LISA forms an ESA/NASA collaborative project, selected as an ESA Cornerstone and included in NASAs 'Beyond Einstein' initiative, with a launch in 2012/2013. The primary objective of the LISA mission is to detect and observe gravitational waves from massive black holes and galactic binaries in the frequency range 10^{-4} to 10^{-1} Hz. This low-frequency range is inaccessible to ground-based interferometers because of the unshieldable background of local gravitational noise and because ground-based interferometers are limited in length to a few kilometres.

LISA will measure distance changes between test masses by measuring the phase changes in a fraction of a mW of light reflected from the test masses. Light reflected from the test masses produces a force on them. Fluctuating laser power leads to fluctuating forces which could limit LISA's sensitivity. Relative power fluctuations of less than $2 \cdot 10^{-4} / \sqrt{\text{Hz}}$ can be tolerated (ESA-SCI 11, 2000, p. 77). Celestial mechanics of the LISA orbits will cause relative armlength variations in the order of 10^{-2} (=50000 km) and these would produce spurious signals from laser phase fluctuations (Danzmann and Rüdiger, 2003). From LISA's strain sensitivity goal of 10^{-23} , one can calculate an upper

limit of allowed laser frequency fluctuations in the $\mu\text{Hz}/\sqrt{\text{Hz}}$ range which is very difficult to achieve and may even be impossible to implement only with hardware. Three mechanisms will be used for laser frequency noise suppression: frequency stabilization to optical cavities, to the mean armlength, and time delay interferometry. As requirement for the frequency stabilization to optical cavities, frequency fluctuations below $30 \text{ Hz}/\sqrt{\text{Hz}}$ have been set from 1 mHz to 1 Hz (ESA-SCI 11, 2000, p. 76).

LISA requires laser sources with 1 W of output power in a diffraction limited single-frequency beam that can be stabilized in output power and frequency. In ground-based interferometric gravitational wave detectors, diode-pumped nonplanar ring oscillators (NPROs) (Kane and Byer, 1985; Freitag et al., 1995) have proven as reliable laser sources, and they have also been identified as suitable laser candidates for LISA (Peterseim, 1999; ESA-SCI 11, 2000). It has also been identified that active stabilization schemes will be necessary for laser power and frequency. The most promising configurations for a LISA laser are a stand-alone high-power NPRO or a fiber amplifier seeded by a low-power NPRO and the high-power version has been selected as baseline (ESA-SCI 11, 2000, p. 278). While noise properties of NPROs have been studied for Fourier frequencies in the acoustic regime, little information on the noise properties of NPROs and amplifiers was available in the LISA measurement band, and there has been no experimental laser development targeted to the LISA specifications so far.

The goal of this work was to implement a laboratory model of a LISA laser based on a high-power NPRO, characterize its noise properties, demonstrate the required power and frequency stabilities in a laboratory setup and identify noise sources in the stabilization schemes. Before lasers could be developed or stabilized in power or frequency, means had to be developed to characterize their noise properties in the LISA measurement band from 0.1 mHz to 1 Hz, since there are no commercial spectrum analyzers available for noise characterizations below 1 mHz. Noise properties were characterized in this work by digitally sampling data and computing spectral densities from the time series. For this purpose, an improved algorithm was developed that is especially well-suited for large amounts of data and a logarithmically scaled frequency axis, as was necessary within this work.

In Chapter 2, several methods of spectral estimation from time series are reviewed and the advantages of the newly developed algorithm are shown in comparison to the standard method.

In Chapter 3, the development and characterization of the laser demonstrator based on a stand-alone high-power NPRO is described. In addition, the second configuration for a LISA laser has been investigated: a low-power laser seeding a fiber amplifier. A fiber amplifier was set up, its noise properties have been investigated and suitable actuators for power and frequency have been identified. The experiments and results are reported on in Section 3.3. In Section 3.4, the characterization of a distributed-feedback fiber laser is described and its suitability as low-power seed oscillator for LISA is evaluated. In Section 3.5, the single-stage concept is compared to the two-stage concept.

The experiments and results related to the power stabilization of the LISA laser demonstrator are described in Chapter 4, and the frequency stabilization related experiments and results are reported on in Chapter 5.

2. Signal and noise characterization in the frequency domain

The space-based gravitational wave detector LISA has been designed to detect gravitational waves with frequencies ranging from 10^{-4} to 10^{-1} Hz. Laser power fluctuations and frequency fluctuations and many other noise sources can disturb the measurement of gravitational waves and need to be suppressed in the LISA measurement window. Hence, a frequency-resolved characterization of such fluctuations is necessary. Commonly, spectral densities are used to specify the amount of fluctuations of a quantity.

For frequencies down to 1 mHz, commercial spectrum analyzers (e. g. SR785 by Stanford Research Systems) can be used for noise characterizations. There exist however no commercially available spectrum analyzers for the complete LISA measurement band down to 0.1 mHz and means had to be developed in order to characterize laser sources for LISA.

Two experimental methods commonly used to measure the spectral distribution of an experimental quantity are (a) using analog bandpass filters or (b) digitizing the quantity with an A/D converter and applying digital algorithms to the time series. While (a) is used for high-frequency signals, (b) is a general method that finds widespread application, i.e. in commercial spectrum analyzers. Only (b) is considered here.

In Section 2.1 existing methods of spectral estimation are reviewed and results and drawbacks of the popular method of “windowed overlapped segmented averages” are presented.

Assume, the output power of a laser is measured, converted to a voltage and recorded. The data obtained is called time series (here, a voltage as function of time). Spectral representations of the fluctuations show the amount of fluctuations versus the fluctuation frequency (also called Fourier frequency). Four normalizations are commonly used: power spectra, power spectral densities, linear spectra and linear spectral densities.

Spectra preserve the heights of sinusoidal peaks while spectral densities preserve noise floors (for example shot noise). In the present example, power spectra have the units V^2 and power spectral densities have units V^2/Hz . The linear quantities are the square root of the corresponding quadratic (power) quantities.

The calibration of spectral estimates is discussed in more detail in Appendix A.5.

2.1. Existing methods

It is often useful to plot spectral estimates on a logarithmically uniform frequency axis. Special algorithms have been developed in the context of acoustical research (Brown, 1991; Brown and Puckette, 1992; Teaney et al., 1980) and their spectral estimates are known as “constant-Q” estimates. A survey of other spectral estimation methods with logarithmically uniform frequency resolution not specifically tailored to musical research can be found in Carnal and Rochelle (1984).

A popular method for spectral estimation with uniform frequency resolution for the case of abundant equidistant samples is the so-called ‘overlapped segmented averaging of modified periodograms’. Here a periodogram means the discrete Fourier transform (DFT) of one segment of the time series, while modified refers to the application of a time-domain window function and averaging is used to reduce the variance of the spectral estimates. This method is attributed to Welch (Welch, 1967) and is also known under various acronyms such as WOSA (for ‘windowed overlapped segmented average’). It is widely used in commercial signal analyzers, oscilloscopes and other equipment. Specialized methods for the case of non-equidistant or very few samples (Thompson, 1971; Giovannelli et al., 1996) or other methods such as the Blackman-Tukey method (Blackman and Tukey, 1959) and the multitaper method (Thompson, 1982) exist, but are not considered here. A description of the two latter methods and a comparison to the WOSA method can be found in Manolakis et al. (2000, Chapter 5).

Modern data acquisition equipment easily allows the collection of very long time series. This leads to spectra covering several decades of frequency which are often plotted on a logarithmic frequency axis in order to display a maximum of information.

The results from a direct application of the WOSA method are, however, equidistant in the frequency domain. A trade-off is necessary between frequency resolution of the spectrum and the number of averages. Especially with a logarithmically scaled frequency axis spanning several decades the problem becomes obvious, as can be seen in Fig. 2.1: While at low frequencies a narrow frequency resolution is necessary, this resolution leads to an inconvenient density of data-points at higher frequencies, where instead better averaging is desirable.

The situation can be improved by arbitrarily splitting the frequency axis and using a coarser frequency resolution for the higher Fourier frequency part of the spectral estimate as is shown in Fig. 2.2: The coarser frequency resolution allows more averages for Fourier frequencies above 5 mHz which results in a smoother curve.

For Figs. 2.1–2.3 the measured input voltage noise of an operational amplifier sampled with a digital voltmeter has been used. For illustrative purposes, two sinusoidal signals, both with $20 \mu\text{V}_{\text{rms}}$ amplitude and frequencies of 1.23×10^{-4} Hz and 2.5×10^{-2} Hz, and a 3.5 dB notch at 0.16 Hz have been additionally introduced by digital processing of the measured data.

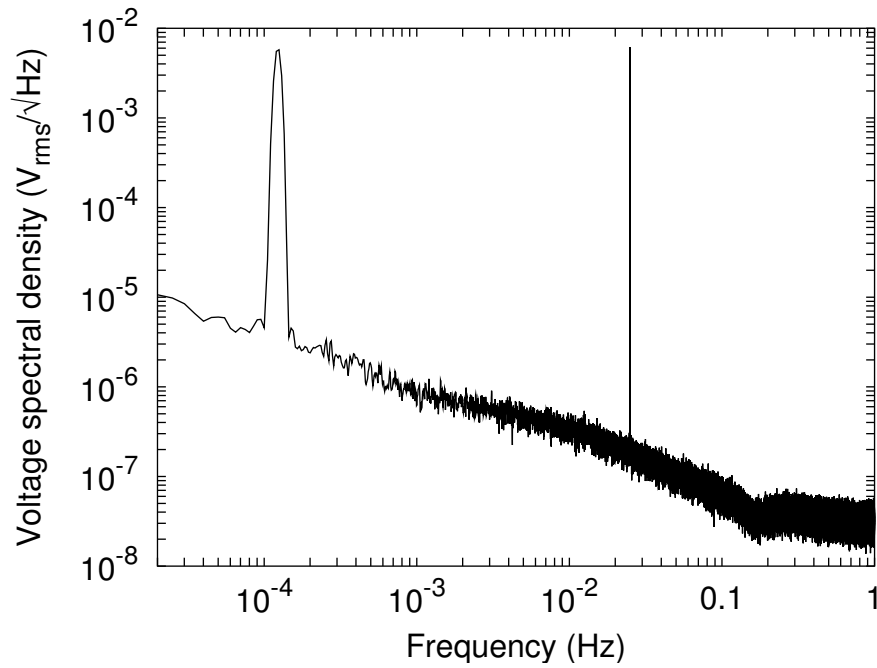


Figure 2.1.: Spectral density estimate obtained by Welch's method of Windowed, Overlapped Segmented Average (WOSA); $5 \mu\text{Hz}$ resolution, 10 averages.

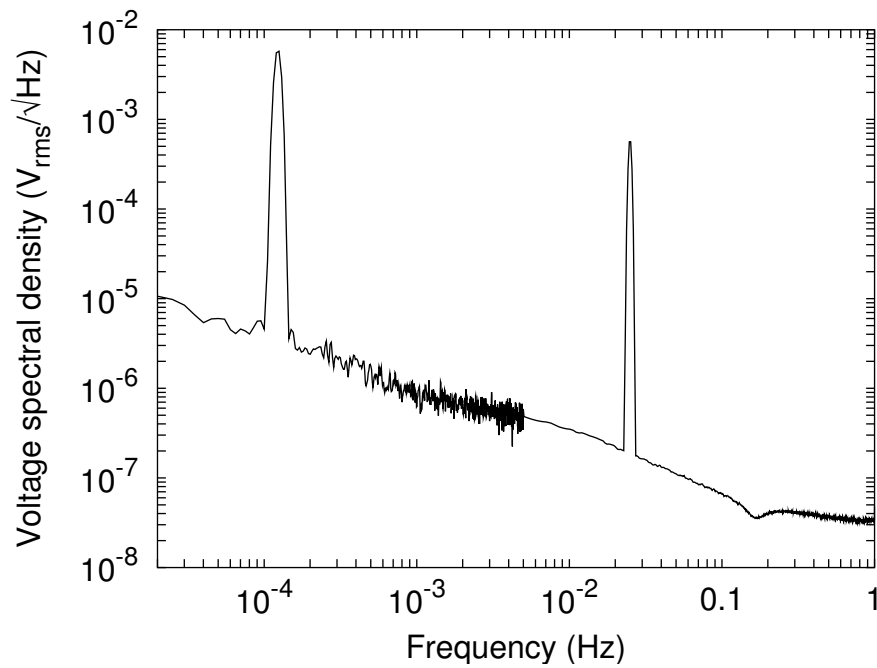


Figure 2.2.: Spectral density estimate obtained by combining the results of the WOSA method with two different frequency resolutions; $5 \mu\text{Hz}$ and $500 \mu\text{Hz}$ resolution, 10 and 1266 averages.

2.2. Improved method

In this section, an extension of the WOSA method that is especially suited for the case of very long time series (at least a few thousand samples) and a logarithmic frequency axis is presented. A typical result is shown in Fig. 2.3. While the WOSA method uses

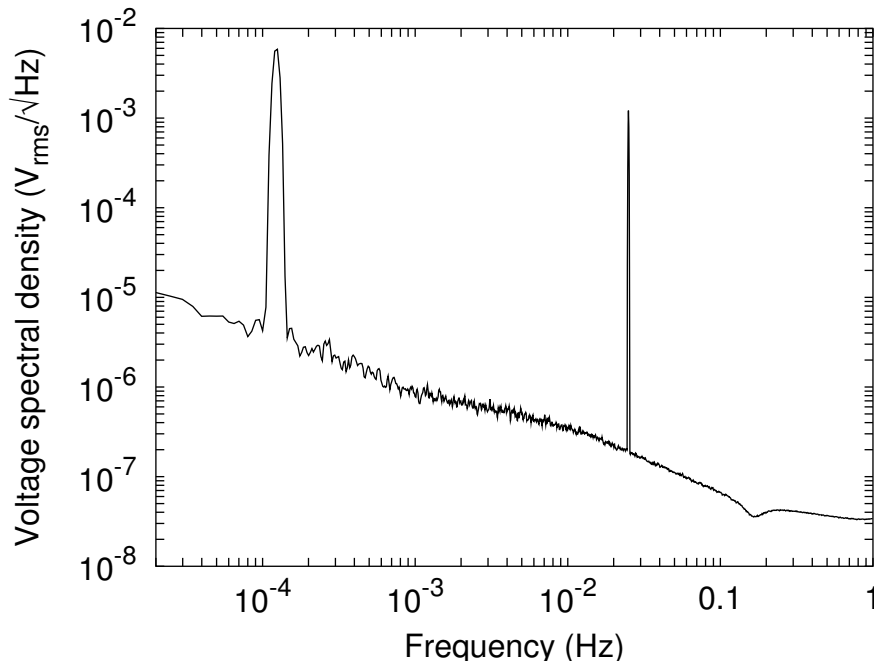


Figure 2.3.: Spectral density estimate obtained by the new LPSD method. The resolution bandwidth is adjusted to the frequency to obtain more averages at higher frequencies; 5 μ Hz to 5.4 mHz resolution, 10 to 12982 averages.

the same frequency resolution for every Fourier frequency, the new method named LPSD (for Logarithmic frequency axis Power Spectral Density) adjusts the frequency resolution for every Fourier frequency in the estimate. The property of the WOSA method that the distance between adjacent Fourier frequencies equals the resolution bandwidth, is approximately maintained.

It turns out that typically for the higher Fourier frequencies, suitable combinations of frequency bandwidth and number of averages can be found without restrictions. In the lower end of the spectrum (the lowest Fourier frequency $f_{\min} \geq 1/T$ and the lowest resolution bandwidth $r_{\min} \geq 1/T$ are both limited by the total measurement time T) however, one needs to abandon the aim of equally spaced Fourier frequencies on the logarithmically scaled axis because the distance between adjacent Fourier frequencies would be smaller than the smallest bandwidth possible with the given amount of data. A parameter has been introduced in the algorithm, the desired number of averages that determines a Fourier frequency above which a uniform spacing on a logarithmically scaled axis is possible. For lower Fourier frequencies this is not possible and a heuristic compromise is used as is described in Appendix A.2.

The computational cost of the LPSD method scales as $\mathcal{O}(N \cdot J)$ with input data size N and number of Fourier frequencies J as will be described in Appendix A. For $J = 419$ a non-optimized implementation takes less than 9 seconds for $N = 10^5$ and less than two minutes for $N = 10^6$ on a typical 2 GHz PC. For the many cases within this work where LPSD has been used, the time required for a program run was always negligible compared with the time necessary to collect the input data.

The LPSD method for spectral estimation is described in detail in Appendix A.

2.3. Conclusions

LISA requires frequency resolved noise characterizations. As requirements, spectral densities are given that are commonly plotted on a logarithmically scaled frequency axis in order to display a maximum of information.

There are no commercially available spectrum analyzers that are suitable for noise characterization in the LISA measurement window down to 0.1 mHz. Instead, the quantities under investigation were digitized with an A/D converter and digital algorithms were applied to the time series.

The standard WOSA method uses a fixed frequency resolution for every frequency of the spectral representation. On a logarithmic frequency axis this resolution cannot be displayed at high frequencies. Instead more averages are desirable to reduce the variance of the estimate.

Equally spaced Fourier frequencies on a logarithmically scaled axis are typically not possible for the entire frequency range. The new method LPSD introduces a parameter, the desired number of averages that determines the Fourier frequency above which a uniform spacing on a logarithmically scaled axis is possible. For lower Fourier frequencies this is not possible and a heuristic compromise has been used as is described in Appendix A.2.

The spectral measurements in this work were performed by digitally sampling data and calculating spectral densities from the data. A novel algorithm was developed that is especially well-suited for large amounts of data and the usage of a logarithmically scaled frequency axis, both of which were necessary in this work. The novel technique based on discrete Fourier transforms for the first time calculates spectral densities with a logarithmically uniform frequency axis and an increasing number of averages towards higher frequencies. This approach allows spectral estimation at very low frequencies that are inaccessible to commercial spectrum analyzers and at the same time it produces spectral estimates that are more accurate than those of the standard WOSA method.

3. Light sources for LISA

In this Chapter, the first experimental laser development for LISA is presented. It was focussed on characterizations of power fluctuations and frequency fluctuations of different laser sources.

In Section 3.1, an important subset of LISA requirements is reviewed, their physical origins discussed, and suitable laser candidates are presented. The two concepts are either a high-power nonplanar ring oscillator or a fiber amplifier seeded by a low-power laser.

The development, implementation, and characterization of the first laser demonstrator for LISA based on a high-power NPRO is presented in Section 3.2. For the first time, a fiber amplifier is investigated and its noise properties characterized in the LISA frequency range. In Section 3.3, excess power noise, excess frequency noise, and suitable actuators for power and frequency are discussed. As an alternative to a low-power NPRO in a master-oscillator power-amplifier configuration, a distributed-feedback fiber laser is investigated and reported on in Section 3.4.

3.1. Requirements and possible laser designs

LISA is in principle a Michelson interferometer with 5 million km armlength. It comprises three satellites in heliocentric orbits. With 30 cm diameter telescopes and 1 W of infrared laser power in TEM₀₀ mode, some 10⁻¹⁰ W will be detected after 5 million km at the distant satellite (Danzmann and Rüdiger, 2003) and it is hopeless to directly reflect light back to the first spacecraft. Instead, the distant spacecraft phase-locks its own laser to the incoming light. Shot noise of the incoming light plays a major role in the total noise budget. To achieve a strain sensitivity of 10⁻²³ (averaged over 1 year, with a signal-to-noise ratio of 5), 1 W of light power is required for 30 cm diameter telescopes (ESA-SCI 11, 2000). A wavelength of 1064 nm has been chosen, since Nd:YAG lasers emitting at that wavelength have proven to be reliable, robust, and efficient in earth-based applications and can be radiation hardened by co-doping with Cr³⁺ (Rose et al., 1995). Linearly polarized light and the frequency tuning capability are required for phase locking of the different lasers on board of the satellites.

Each satellite contains two test masses, one for each interferometer arm. The test masses, cubes of the approximate dimensions 4 by 4 by 4 cm³ made of an Au/Pt alloy of low magnetic susceptibility, reflect the light arriving from the remote spacecraft and define the reference mirror of the interferometer arm. The laser power reflected from

the test masses produces a force on them. On their back face, an interferometer using a few 100 μW of light measures the position of the test mass with respect to the satellite. Fluctuations in the laser power will thus introduce fluctuating forces on the test masses which could limit the sensitivity of LISA. A requirement for relative power fluctuations of $2 \cdot 10^{-4}/\sqrt{\text{Hz}}$ has been defined (ESA-SCI 11, 2000, p. 77).

Although nonplanar ring oscillators achieve shot-noise limited operation at MHz frequencies (Kane, 1990) technical noise such as pump power noise is dominating at low frequencies (Hunnekuhl, 2004). Accordingly, an active power stabilization is required for LISA and hence power actuators in the laser system are required.

Celestial mechanics of the LISA orbits will cause relative armlength variations in the order of 10^{-2} (=50000 km) and these would produce spurious signals from laser frequency fluctuations (Danzmann and Rüdiger, 2003). From LISA's strain sensitivity goal of 10^{-23} one can calculate an upper limit of allowed laser frequency fluctuations in the $\mu\text{Hz}/\sqrt{\text{Hz}}$ range (ESA-SCI 11, 2000, p. 76) which requires active frequency stabilization to an external reference. Since LISA requires active frequency stabilization and an offset-phase lock of its lasers, a frequency actuator is required. The lasers on board of the LISA satellites will be frequency-locked to an external reference cavity, or to the mean armlength (Sheard et al., 2003) or to a remote laser in a transponder scheme (Danzmann and Rüdiger, 2003) or to a combination of all these. For the design of the frequency stabilization control loop the knowledge of the frequency actuator transfer function is required. Nevertheless, the frequency stability required by LISA is very difficult to achieve and may even be impossible to implement in hardware. Hence, in addition, a sophisticated algorithm, which is described elsewhere (Giampieri et al., 1996; Tinto et al., 2002; Armstrong et al., 2003), will be required to cancel the remaining laser frequency noise and obtain the measurement signal. The free-running frequency noise of the laser system should be as low as possible.

Requirements such as lifetime, power and mass budget or efficiency have not been considered in this stage of the development. They remain for technologically more advanced versions of the LISA laser system.

Table 3.1 shows a summary of the requirements for the LISA laser system. The upper limits of power and frequency fluctuations require active stabilizations to external references and the requirements given relate to the stabilized light sources. The remaining requirements shall also be fulfilled by the free-running (unstabilized) lasers. All requirements are discussed in detail below.

The most promising candidates for the generation of output characteristics as given in Table 3.1 are a stand-alone high-power NPROs (Kane and Byer, 1985; Freitag et al., 1995) operating at 1064 nm or a fiber amplifier seeded by a low-power NPRO (ESA-SCI 11, 2000). Hence, in Section 3.2 the design, implementation and characterization of a laser system based on a stand-alone NPRO emitting 1 W out of a single-mode polarization-maintaining fiber are discussed.

When a master oscillator power amplifier configuration containing a fiber-based amplifier is used, then the use of a fiber-based master oscillator is attractive. A distributed feedback (DFB) fiber laser is discussed in Section 3.4. The laser frequency has been stabilized to a Fabry-Perot cavity, the frequency actuator characteristics have been in-

Parameter	Requirement
Output power	1 W
Longitudinal mode	single-frequency
Transverse mode	TEM ₀₀
Wavelength	1064 nm
Frequency tuning range	10 GHz
Polarization contrast	> 100 : 1
Rel. power fluctuations	$< 2 \cdot 10^{-4} / \sqrt{\text{Hz}}$ (0.1 mHz – 10 Hz)
Frequency fluctuations	$< 30 \text{ Hz} / \sqrt{\text{Hz}}$ (1 mHz – 1 Hz)

Table 3.1.: Requirements for the LISA laser system.

investigated and the free-running frequency fluctuations have been measured.

In Section 3.3 investigations of a fiber amplifier are presented. The excess fluctuations in power and frequency have been measured and actuators for power and frequency have been identified and characterized.

3.2. The first laser demonstrator for LISA

A laser system based on a stand-alone high-power NPRO has been selected as baseline for the LISA laser (ESA-SCI 11, 2000, p. 278) and in this section, the setup and characterization of a laboratory version of such a laser system is described.

The laser setup is described in Section 3.2.1, followed by the characterization of its output power and polarization in Section 3.2.2. In Section 3.2.3, actuators for laser power and frequency, thermal laser frequency tuning, and the effect of laser pump power changes on laser frequency are discussed. In Section 3.2.4 the measured power fluctuations and in Section 3.2.5 the measured frequency fluctuations are presented. The measured fluctuations of a low-power NPRO (Mephisto 500 by Innolight) has been added in both cases for comparison.

3.2.1. Setup

The laser demonstrator for LISA was based on an NPRO that was longitudinally diode pumped through the crystal front facet. The operation of NPROs has been described in detail by Kane and Byer (1985) and Nilsson et al. (1989). In order to obtain high output powers, the thermally induced lens of the NPRO was partially compensated by a concave front facet with -1500 mm radius of curvature. The drawback of the curved front facet is a higher pump threshold, since the resonator now requires a thermal lens for stable operation. The region directly behind the front facet was made of undoped YAG to avoid spatial hole burning and to ensure single-frequency operation (Freitag et al., 1995). Up to 1.9 W of output power have been obtained directly out of the laser crystal at 4.4 W of pump power (see Fig. 3.5).

Figure 3.1 shows the beam path within the laser crystal and the laser crystal holder in more detail. The oscillating field is reflected at the dielectrically coated front facet of the laser crystal. At the remaining three facets, the beam is reflected by total internal reflection. The nonplanar beam path leads to a reciprocal polarization rotation within one round trip. The two magnets placed below the laser crystal (the front magnet is not shown) generate a magnetic field of 0.3 T in the plane of the laser crystal. The non-vanishing Verdet constant of YAG leads to nonreciprocal polarization rotation, which leads to different eigenpolarizations for the two round-trip directions (Nilsson et al., 1989). The two round-trip directions experience different losses at the dielectrically coated front facet. Since Nd:YAG is a homogeneously broadened laser material, unidirectional operation and single-frequency operation result. A piezo-electric trans-

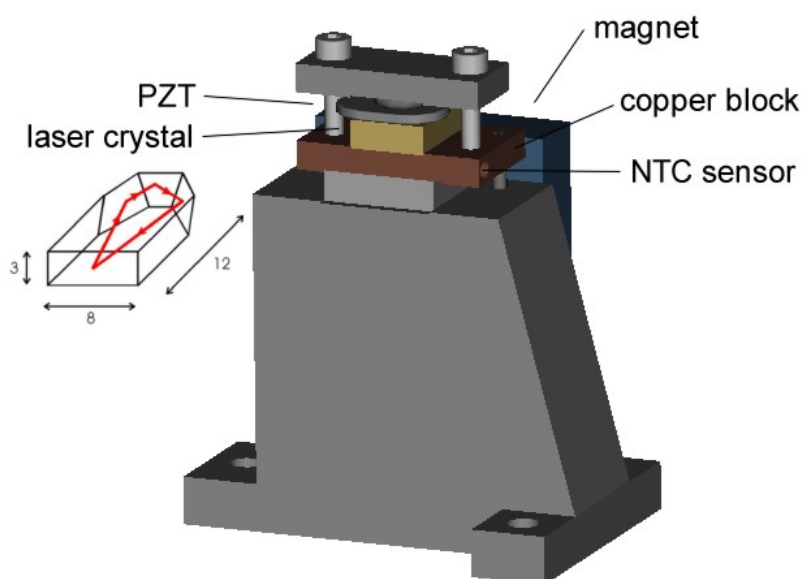


Figure 3.1.: Laser crystal holder of the LISA laser demonstrator.

ducer (PZT) was glued onto the laser crystal as fast frequency actuator. When a voltage is applied to the PZT, the laser frequency is shifted due to stress-induced birefringence in the laser crystal (Freitag, 1994). The laser crystal is pressed onto a copper plate that contains a temperature sensor. This temperature sensor and the thermo-electric cooler (TEC) below the copper plate were used in a control loop with a unity gain frequency of approximately 1 Hz to stabilize the temperature of the laser crystal and hence the laser frequency. Variations in laser crystal temperature setpoint were used as slow laser frequency actuator.

Fig. 3.2 shows the schematic setup of the LISA laser demonstrator. The pump light from fiber coupled laser diodes (for details see below) was delivered by a multimode fiber (100 μm core diameter, $\text{NA}=0.22$), collimated with a lens ($f=30$ mm) and focussed into the laser crystal with a second lens ($f=25$ mm). The absorption length in the laser crystal was estimated to approximately 3 mm. The laser radiation was transmitted through a

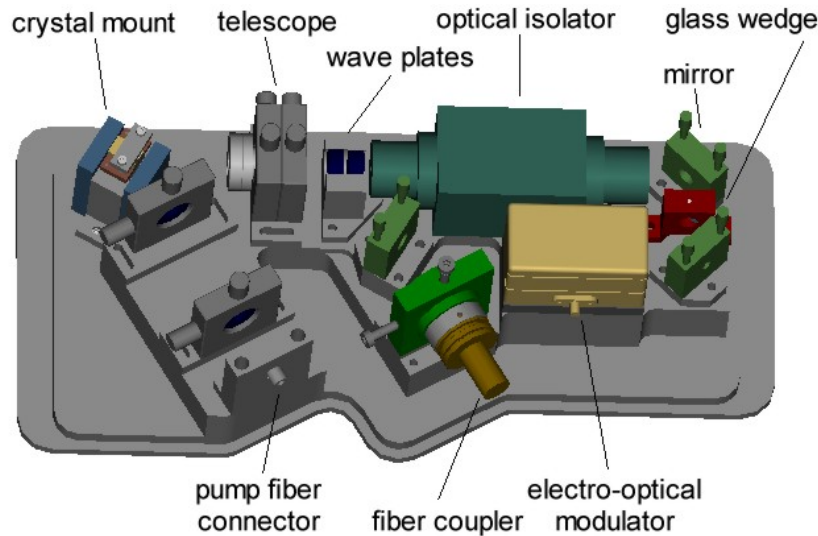


Figure 3.2.: Schematic setup of the LISA laser demonstrator.

telescope that generated a collimated beam with 1 mm beam diameter. A quarter-wave plate and a half-wave plate were used to transform the elliptically polarized light into linearly polarized light and to adjust the polarization axis to that of the subsequent optical isolator that protected the laser from backreflections. Two mirrors were used to align the light through the electro-optical modulator (EOM, model 4003 by New Focus) that was required for frequency stabilization. Optionally, a glass wedge could be placed between the two mirrors to couple out light without phase modulation for a beat measurement. A third mirror was used to couple the light into a single-mode polarization-maintaining fiber with angle-polished ends (8° FC-APC type) to avoid backreflections and parasitic etalons. The fiber coupler (60SM-1-4-A4.5-03 by Schäfter & Kirchhoff) was mounted on an XY-translation stage to center the coupler to the optical beam. Three pressure screws and three tension screws in the coupler allowed its correct alignment to the optical beam axis and the collimating lens inside the coupler could be adjusted in beam direction to achieve optimum focussing into the single-mode fiber.

Figure 3.3 shows a picture of the laser demonstrator. The fiber connectors for pump light and laser light are visible as well as electrical connectors for the EOM, the temperature stabilization of the laser crystal, and actuator signals for the PZT. The demonstrator has a mass of 6 kg and a footprint of $300 \times 140 \text{ mm}^2$.

The pump module for the laser is shown in Fig. 3.4. It was manufactured by Bright-power and emits up to almost 10 W of pump power (Rugi et al., 2003). It contains eight laser diodes (c-mounts) coupled into a multi-mode fiber (100 μm core diameter, $\text{NA}=0.22$). The laser diodes share a common water-cooled heat sink. At a cooling water temperature of 20° and 4 W of output power an emission wavelength of 806.5 nm with a full width at half maximum (FWHM) of 1.5 nm was measured. Two identical constant current laser diode drivers (Mephisto control electronics by Innolight modified to drive 4 diodes in series) were used to drive four laser diodes each.



Figure 3.3.: LISA laser demonstrator with open top cover.

3.2.2. Output power and polarization

Figure 3.5 shows the output power of the laser demonstrator as function of pump power. The upper trace shows the laser output power directly out of the laser crystal and the lower trace shows the output power out of the single-mode fiber.

A slope efficiency of 58% was achieved for the power emitted from the laser crystal and 42% for the power out of the fiber. A laser threshold of 1.36 W of pump power was measured. The relatively high pump threshold is due to the unstable resonator design that requires a thermal lens for operation. With increasing pump power the mode radius within the laser crystal changes as well as the beam divergence outside the laser crystal. This affects the mode matching between laser mode and single-mode fiber. The coupling efficiency was optimized for high output powers. At 130 mW emitted from the fiber, 59% coupling efficiency were measured, whereas at 1.2 W, 73% coupling efficiency were obtained.

The polarization of the light out of the single-mode fiber has been measured for output powers ranging from 0.1 W to 1.2 W. The light was linearly polarized, and the ratio of power in the axis perpendicular to the main axis relative to the total power was smaller than $1.2 \cdot 10^{-3}$ (1:830).

3.2.3. Power and frequency actuators

Power and frequency actuators are necessary for LISA, as has been discussed above. As power actuator, the pump power of the laser demonstrator has been used. A current modulation input in one of the laser diode drivers was used to vary the current of four laser diodes within the pump module. The transfer function from current modulation input to laser diode current showed low-pass characteristics with a corner frequency of



Figure 3.4.: Pump module for the LISA laser demonstrator.

5 kHz.

Although pump power variations have been used as frequency actuator in nonplanar ring oscillators (Willke et al., 2000), they will not be used in this work to change the laser frequency, since LISA requires separate actuators for power and frequency. Instead, laser crystal temperature changes and a PZT on the laser crystal will be used as frequency actuators.

The thermal frequency tuning has been measured using a wavemeter (WA-1500 by EXFO, former Burleigh). In Fig. 3.6 the measured laser frequency is plotted versus laser crystal temperature. Continuous frequency tuning of up to 9 GHz was measured. Single-frequency operation was verified using a scanning Fabry-Perot interferometer. Only at the limits of the continuous tuning ranges, mode-hops occurred.

The mean thermal tuning coefficient between 20°C and 40°C was determined by fits of linear functions to the continuous regions and averaging of their slopes. A mean thermal tuning coefficient of $-3.2 \text{ GHz/K} \pm 0.2 \text{ GHz/K}$ was obtained. The measured value agrees with the thermal tuning coefficient of -3.1 GHz/K given in literature (Freitag, 1994) and the largest error contribution is given by the nonlinearity of the negative temperature coefficient (NTC) resistor that was used to determine the laser crystal temperature.

The free-spectral range of the laser was also determined from the data shown in Fig. 3.6 by calculating the frequency differences between the fitted linear functions at a fixed temperature. As mean value for the free spectral range $5.81 \text{ GHz} \pm 0.01 \text{ GHz}$ was obtained. A free-spectral range smaller than the continuous tuning range of the laser can be explained by a shift of the emission spectrum of Nd:YAG (Freitag, 1994; Hunnekuhl, 2004). An overall tuning range of 30 GHz was measured which is significantly larger than

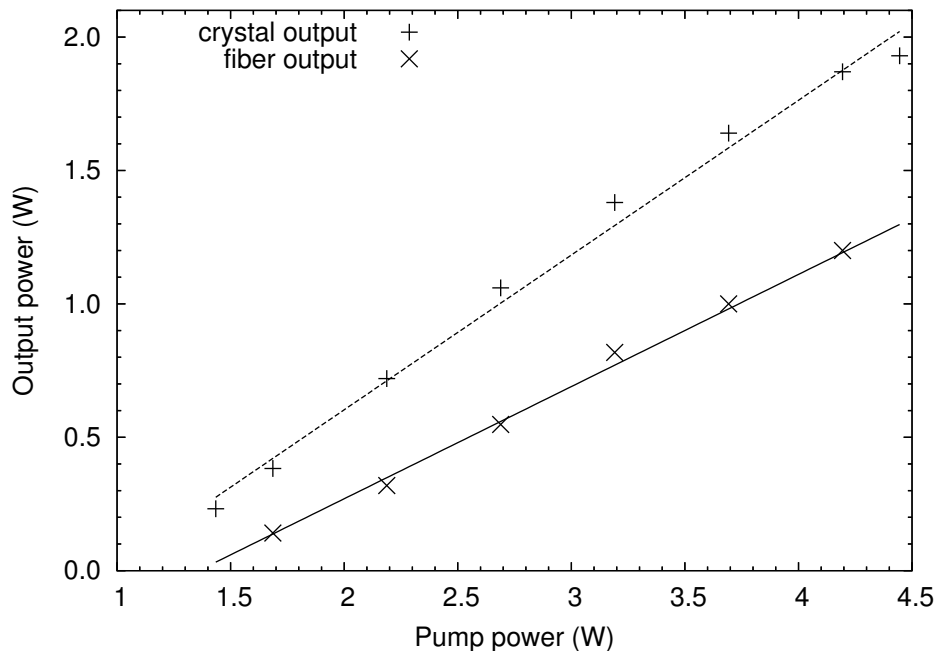


Figure 3.5.: LISA laser demonstrator output power versus pump power.

the requirement of 10 GHz.

The PZT frequency tuning coefficient was determined using the frequency stabilization setup described in Chapter 5. A PZT tuning coefficient of 1.9 MHz/V with a flat transfer function up to 100 kHz has been measured. Its sign depends on the orientation of the PZT. The measurements are described in detail in Chapter 5.

Besides changing the laser output power, a change in pump power of the LISA laser demonstrator induces frequency changes due to a local change of the temperature distribution as has been investigated previously (Day, 1990; Quetschke, 2003; Hunnekuhl, 2004). While this effect has been purposefully used (Willke et al., 2000; Hunnekuhl, 2004; Heurs et al., 2004) it represents an unintended cross-coupling within the LISA laser demonstrator.

Figure 3.7 shows the measured transfer function from pump power modulation to frequency modulation with a fit. The pump current of the laser demonstrator has been sinusoidally modulated (with ten different modulation frequencies) and the resulting beat frequency with a frequency stabilized laser has been recorded. Simultaneously, the resulting output power variations have been measured and the amplitudes of pump power change and frequency change have been stored. In Fig. 3.7 the amplitude ratio of frequency change to output power change has been plotted. The measured data have been fitted with a single pole. As fit parameters, a pole frequency of 0.14 Hz and a DC response of 1 MHz/mW have been obtained.

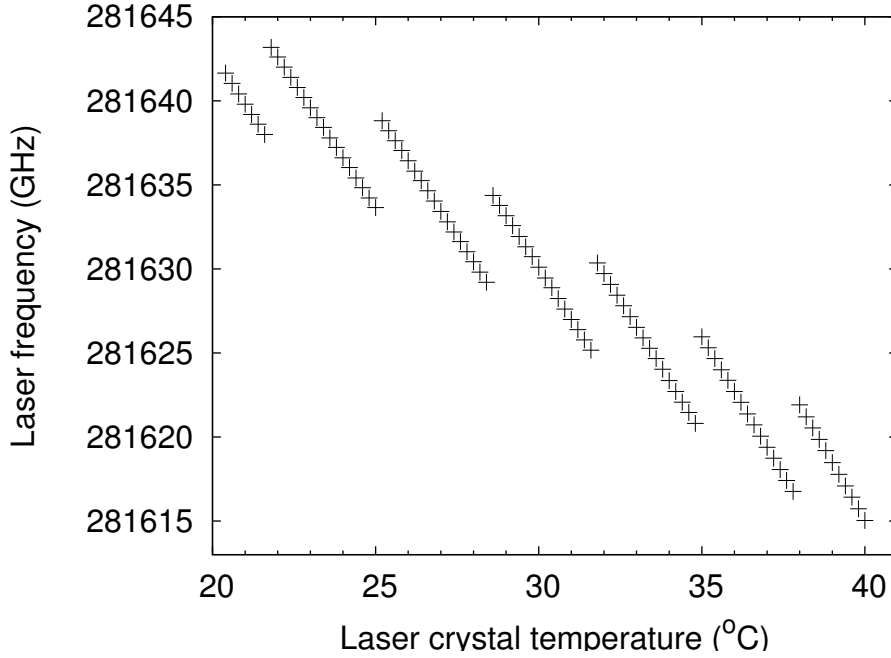


Figure 3.6.: LISA laser demonstrator thermal frequency tuning characteristics.

3.2.4. Power fluctuations

Figure 3.8 shows the free-running relative power fluctuations of the LISA laser demonstrator and the simultaneously measured relative pump power fluctuations. For frequencies below 1 mHz the relative power fluctuations show a flat spectral density at a level of $6 \cdot 10^{-3}/\sqrt{\text{Hz}}$ decreasing with approximately $1/f$ for higher frequencies. It is visible that pump power fluctuations transfer to laser output power fluctuations, since both traces show the same noise level. The laser output power has been measured by sampling a fraction of the beam with a glass wedge and a temperature-stabilized Si photodiode. The pump power fluctuations have been measured using the two monitor photodiodes built into the pump module. In order to obtain the pump power fluctuations displayed in Fig. 3.8 the power fluctuations of both monitor diodes have been calculated, and their weighted geometrical mean has been plotted.

The third trace in Fig. 3.8 shows the free-running power fluctuations of the low-power NPRO that will later be used in Chapter 5. They have been measured with a temperature-stabilized Si photodiode. This trace will later be used in Section 3.5.

3.2.5. Frequency fluctuations

Figure 3.9 shows the free-running frequency noise of the laser demonstrator (labelled HSL for High Stability Laser) and a low-power NPRO (Mephisto 500 by Innolight) operated at 100 mW of output power (labelled M2). Free-running means that the laser frequency was not stabilized to an external reference. Instead, the laser crystal temper-

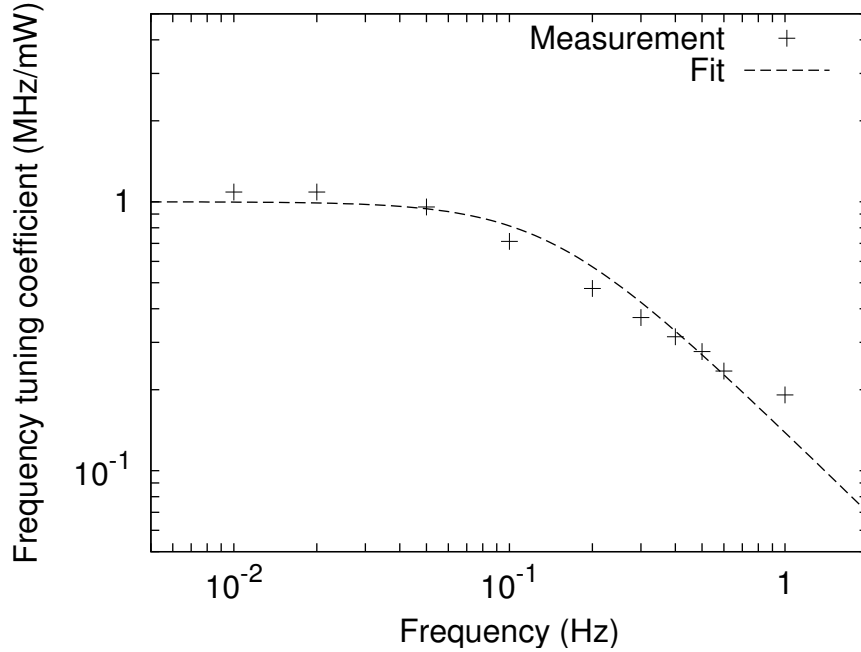


Figure 3.7.: LISA laser demonstrator transfer function from output power to laser frequency.

ature was stabilized and the pump current provided by a constant current source. The graphs were obtained by a difference frequency measurement between the laser under investigation and a frequency stabilized laser. A time series of the beat frequency was recorded and the program LPSD was used to compute spectral densities of frequency fluctuations. The free-running frequency fluctuations of the LISA laser demonstrator were up to a factor of 50 higher than the frequency fluctuations measured for the low-power NPRO. Both lasers used identical laser crystal temperature stabilizations and similar laser crystal mounts but different pump sources. The low-power NPRO was pumped by a single 1 W laser diode (Siemens SFH 48701) with its own temperature stabilization control loop and the laser demonstrator used a pump module containing 8 laser diodes (Osram SPLCG81-2 emitting up to 2 W each) without active temperature stabilization.

The different pump sources might be the cause for the different free-running frequency fluctuations as will be discussed in this paragraph. Since the laser power fluctuations shown in Fig. 3.8 were caused by pump power variations one can use Fig. 3.8 and the transfer function in Fig. 3.7 to estimate the influence of pump power fluctuations on frequency fluctuations. Relative power fluctuations of $1\%/ \sqrt{\text{Hz}}$ as shown in Fig. 3.8 and an output power of up to 1.9 W shown in Fig. 3.5 yield up to $19 \text{ mW}/\sqrt{\text{Hz}}$ of output power fluctuations. Multiplied by 1 MHz/mW taken from Fig. 3.7 this yields power fluctuation induced frequency fluctuations of $19 \text{ MHz}/\sqrt{\text{Hz}}$ at 0.1 mHz which is about two orders of magnitude below the measured free-running frequency fluctuations.

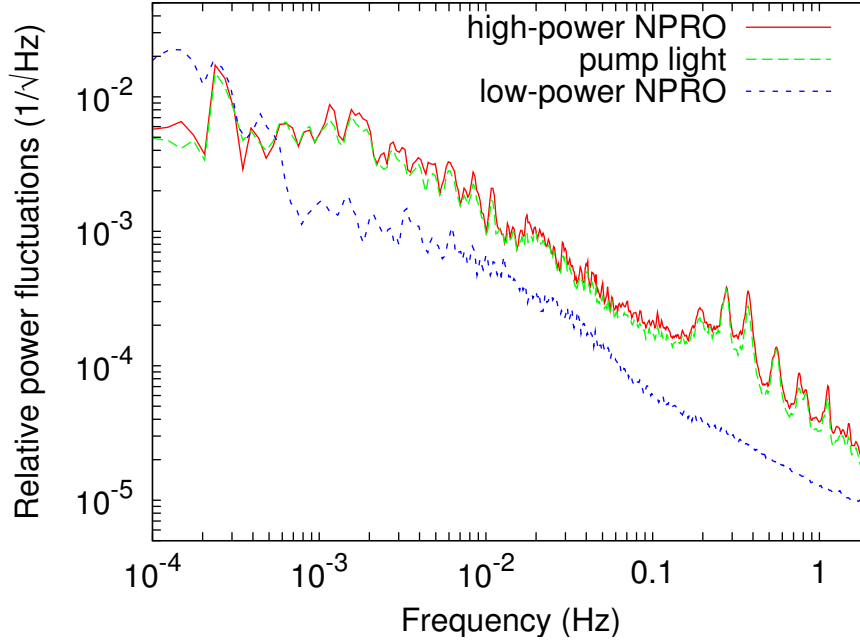


Figure 3.8.: LISA demonstrator free-running relative power fluctuations (labelled high-power NPRO), simultaneously measured relative pump light fluctuations (labelled pump light) and relative power fluctuations of the low-power NPRO that will be utilized in Chapter 5 (labelled low-power NPRO).

Hence, pump power fluctuations do not dominate the frequency fluctuations of the laser demonstrator.

3.2.6. Conclusions

In conclusion, the first laser demonstrator for LISA has been designed, implemented, and characterized. The goal was to implement a laboratory version of a LISA laser. Space qualification aspects as radiation hardness, power consumption, efficiency, mass, etc. were not considered.

Table 3.2 lists the key requirements for the LISA laser system and the measured performance of the laser demonstrator. It emitted up to 1.2 W of single-frequency TEM₀₀ radiation out of a polarization maintaining fiber from 4.4 W of pump power, which represents 20% more output power than was required. A polarization contrast of 830:1 has been measured, which is more than a factor of 8 higher than the requirement of 100:1. The wavelength of the radiation was measured as 1064.5 nm and the measured frequency tuning range of 30 GHz is a factor of 3 larger than the requirement.

The assessment of the wavelength deviation of 0.5 nm between measurement and requirement requires simultaneous consideration of center wavelength and tuning range of all LISA lasers. The reasoning behind both specifications (wavelength and tuning range) is the need to offset phase-lock all LISA lasers, i. e. it is not important that the

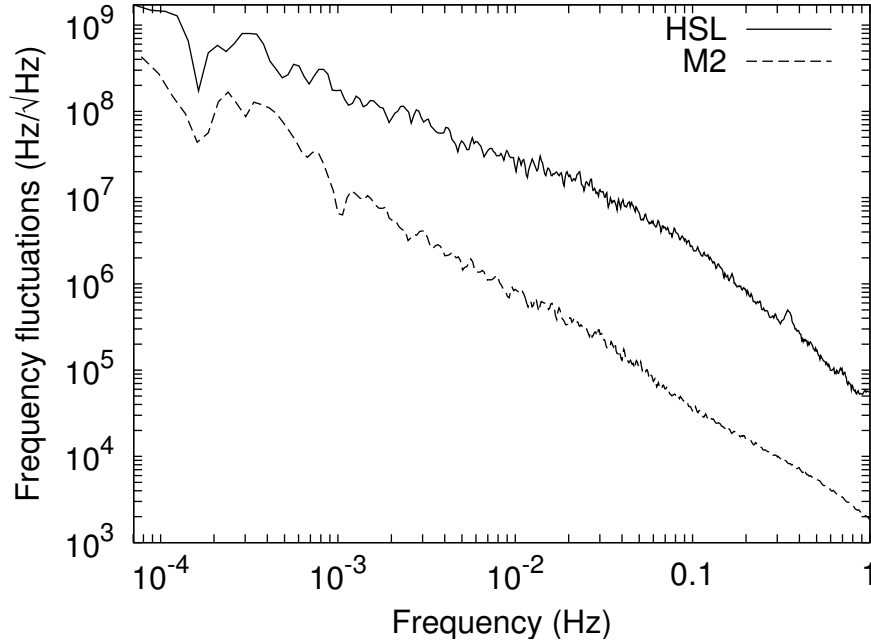


Figure 3.9.: Free-running frequency fluctuations of a high power NPRO with 2 W output power labelled HSL and an NPRO emitting 100 mW labelled M2.

laser emits at exactly 1064.0 nm wavelength. Instead, it must be possible, to phase-lock all six lasers employed within LISA (two on each spacecraft). The specifications given in Table 3.1 are not sufficient to ensure this. Modified specifications are required that need to consider

- the difference frequency for offset phase-locking,
- the frequency tuning ranges, and
- the center frequencies of the individual lasers.

The specifications for relative power fluctuations and frequency fluctuations represent the requirements of the stabilized laser system. For comparison, the measured fluctuations of the free-running laser have been given. Relative output power fluctuations of up to $10^{-2}/\sqrt{\text{Hz}}$ have been measured for Fourier frequencies ranging from 0.1 mHz to 1 Hz. In order to reach the requirement of $2 \cdot 10^{-4}/\sqrt{\text{Hz}}$, the power stabilization needs to suppress laser power fluctuations by up to a factor of 50. One possible scheme (that has been implemented) is to sample a small fraction of the beam, compare the photodetector signal with a reference voltage, amplify the difference, and feed back to the current of the pump laser diodes. Since only a small loop gain (a factor of 50) is required, a control loop with a low bandwidth can be used and the control theory aspect seems uncritical.

Frequency fluctuations of the free-running laser of up to $2 \cdot 10^8 \text{ Hz}/\sqrt{\text{Hz}}$ for Fourier frequencies between 1 mHz and 1 Hz have been measured. They need to be suppressed by more than 6 orders of magnitude to reach the requirement of $30 \text{ Hz}/\sqrt{\text{Hz}}$. One possibility

Parameter	Unit	Requirement	Measurement
Output power	W	1	1.2
Longitudinal mode		single-frequency	single-frequency
Transverse mode		TEM ₀₀	TEM ₀₀
Wavelength	nm	1064	1064.5
Frequency tuning range	GHz	10	30
Polarization contrast	1	> 100 : 1	830:1
Rel. power fluctuations	1/ $\sqrt{\text{Hz}}$	$< 2 \cdot 10^{-4}$	$< 10^{-2}$
Frequency fluctuations	Hz/ $\sqrt{\text{Hz}}$	< 30	$< 2 \cdot 10^8$

Table 3.2.: Required and measured parameters for the LISA laser demonstrator. The upper limit for relative power fluctuations is given for frequencies ranging from 0.1 mHz to 10 Hz, the upper limit for frequency fluctuations is specified for frequencies between 1 mHz and 1 Hz. The measured free-running (un-stabilized) power and frequency fluctuations are compared with the LISA requirements.

for the suppression of frequency fluctuations is the implementation of a control loop that locks the laser frequency to a stable reference frequency. Apart from a stable reference this level of suppression requires a larger actuator bandwidth than required for the power stabilization (due to the higher loop gain requirement) and a careful design of the stabilization setup. The corresponding investigations and results are reported on in Chapter 5.

In conclusion, the laser demonstrator based on a stand-alone NPRO fulfilled the free-running specifications for LISA. The free-running power and frequency noise properties of a high-power NPRO have been characterized for the first time in the LISA measurement band. Stabilization schemes need to be implemented for both power and frequency to reduce the fluctuations. The suppression of more than 10^6 necessary for the frequency fluctuations requires great care in the stabilization but should be possible.

3.3. Ytterbium-doped fiber amplifier

A fiber amplifier seeded by a low-power laser represents a promising laser candidate for LISA. Before this work, the power fluctuations and the frequency fluctuations of fiber amplifiers in the LISA measurement window below 1 Hz were not known.

To date, frequency-resolved power noise of fiber amplifiers has only been measured in the kHz to MHz range and significant excess noise has been reported for frequencies up to 100 kHz in Yb-doped fiber amplifiers (Liem et al., 2003; Weßels et al., 2002), in a Nd:glass fiber amplifier (Zawischa et al., 1999) as well as in injection locked Nd:YAG lasers (Zawischa et al., 2002; Nocera, 2004). LISA requires relative power noise measurements down to 0.1 mHz which will be presented in section 3.3.2.

When using a master oscillator power amplifier scheme, the use of a pre-stabilized

master oscillator is attractive, but only possible if the frequency noise produced by the amplifier is negligible compared to the LISA specifications.

To date, linewidth measurements have been performed to investigate the phase noise properties of a solid-state amplifier (Roth et al., 1998) and of fiber amplifiers (Rochat, 2000; Höfer et al., 2001). However, these measurements do not provide sufficient information to evaluate the suitability of such systems for LISA. Spectrally resolved measurements in the frequency range from 0.1 mHz to 1 Hz are required. Recently, spectrally resolved phase noise measurements of a fiber amplifier for frequencies between 1 Hz and 1 MHz have been reported (Augst et al., 2004).

In Section 3.3.1 the Ytterbium-doped fiber amplifier that was used for the experiments is described followed by power noise measurements of the seed laser, the amplifier output, and the amplifier pump diode in Section 3.3.2. In Section 3.3.3 phase noise measurements are presented, and in Section 3.3.4 appropriate actuators for power and frequency stabilization of the master oscillator fiber amplifier system are discussed.

3.3.1. Setup

Figure 3.10 shows a schematic of the fiber amplifier setup. The fiber amplifier used

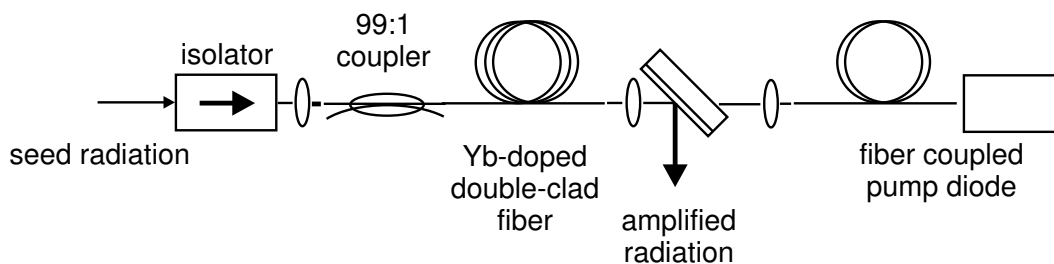


Figure 3.10.: Setup of the Ytterbium-doped fiber amplifier.

3 m of Yb-doped single-mode double-clad fiber (6500 mol ppm Yb_2O_3) with $5.2\ \mu\text{m}$ core diameter, $105\ \mu\text{m}$ pump cladding diameter and numerical apertures of 0.15 and 0.38 for core and pump cladding, respectively.

The amplifier was seeded by an NPRO (Mephisto 800 by Innolight) and it was pumped at a wavelength of 976 nm counterdirectionally to the seed signal by a peltier-cooled and fiber-coupled pump diode (DFx03 by Dilas) using a $200\ \mu\text{m}$ core diameter fiber with a numerical aperture of 0.2. Lenses with focal lengths of 20 mm for pump light collimation and of 8 mm for focusing were used. Due to the pump light absorption and the fact that undoped fibers of the same geometry were not available, the coupling efficiency could not be measured. Hence, the amount of absorbed pump power was not exactly known. From 8.3 W of pump power incident to the pump light telescope, 2.2 W were transmitted through the amplifier. With an estimate of 65% for the pump light coupling efficiency based on practical experience, an amount of 3.2 W of absorbed pump power could be estimated.

To monitor the optical seed power, a fiber coupler has been incorporated into the input port of the amplifier. All fiber ends were angle-polished by 8° to avoid optical back

reflections. In the experiments 1 W of output power has been generated from 10 mW of seed power.

The amount of amplified spontaneous emission (ASE) produced from the amplifier was measured to be below 0.1% of the total output power in the wavelength range from 1030 nm to 1090 nm. From the optical output power spectrum of the fiber amplifier an upper limit for the influence of amplified spontaneous emission on the amplifier output power fluctuations was calculated. For this upper limit the beat between amplifier signal and ASE at the signal wavelength was computed and the ASE-induced power fluctuations were found to be below $10^{-8}/\sqrt{\text{Hz}}$ (for a description of the computation see Weßels (2004, p. 34)).

Within the amplification bandwidth (1030 nm to 1090 nm) of the amplifier, its wavelength is determined by the seed laser wavelength and the tunability of the seed laser determines the tunability of the amplified emission. Hence, center frequency and tuning range of the amplified emission were not measured, but values taken from the NPRO datasheet. The output spectrum of the amplifier is determined by the spectrum of the seed laser. Since a single longitudinal mode was used as seed source, the output had to be in single longitudinal mode as well, as was verified using a scanning Fabry-Perot interferometer. The transverse mode properties of the amplifier output were limited to the fundamental mode by the single-mode core of the double-clad fiber and therefore were not measured. The polarization contrast of the amplifier output was measured to be better than 300:1.

3.3.2. Power fluctuations

The power noise of seed laser and amplifier output have been measured simultaneously. A photodetector was placed behind the second output port of the fiber coupler, and a glass wedge was used to direct a portion of the amplifier output to a second photodetector. In order to be insensitive to polarization changes the glass wedge was used under a small angle of incidence. For the low-frequency measurements up to 1 Hz Fourier frequency, temperature-stabilized InGaAs PIN photodiodes were used, their signals recorded and LPSD has been used to compute relative power noise spectral densities. For the higher frequency part, InGaAs PIN photodiodes with a flat frequency response up to 100 kHz were used and their signals were directly fed into a commercial spectrum analyzer (SR785 by Stanford Research Systems). For the five frequency decades above 1 Hz, up to five measurements were appended for each curve.

Figure 3.11 shows the results of the power noise measurements. The curve labelled “Amplifier” denotes the relative power fluctuations of the amplifier output, “Pump” the fluctuations of the pump diode, and “NPRO” the fluctuations of the seed laser. The “bump” between 10 kHz and 20 kHz in the NPRO trace was caused by the NPRO drive electronics. The noise floor above 10 Hz is likely to be dominated by NPRO pump power noise as has been shown for the NPROs discussed in Hunnekuhl (2004). The curve shows peaks at 50 Hz and multiples that originate from the electrical power grid. The remaining peaks in the frequency range between 50 Hz and 3 kHz are likely to be caused by acoustic noise and vibrations of mechanical components within the optical

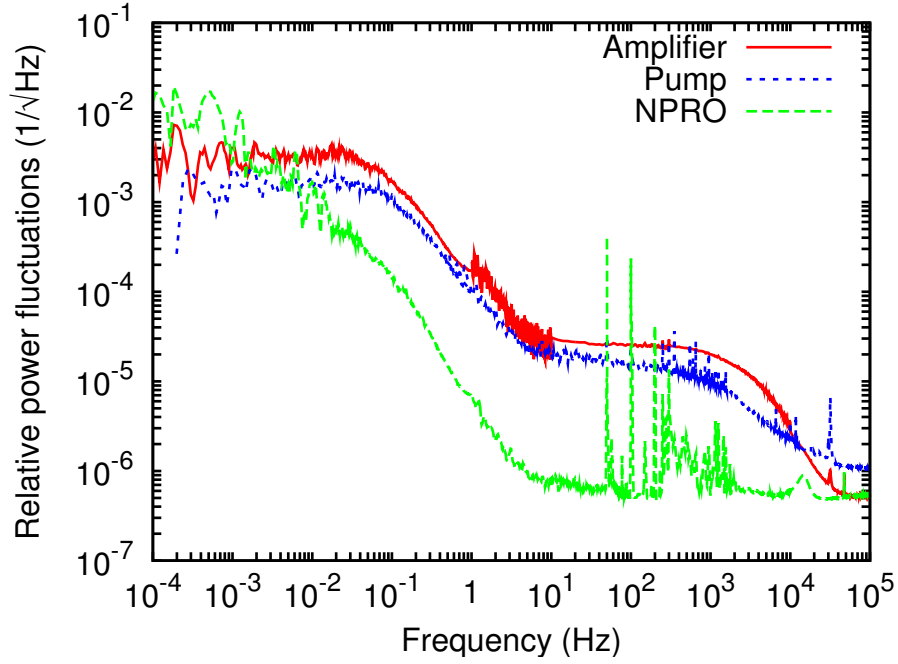


Figure 3.11.: Relative power fluctuations of fiber amplifier, seed laser, and pump diode.

setup. It is visible that the pump power fluctuations are not more than a factor of two below the amplifier fluctuations, which indicates that pump power fluctuations are the dominant noise source for amplifier power fluctuations. The cross-over of amplifier power fluctuations and pump power fluctuations at 10 kHz is no contradiction. For frequencies above the inverse effective life-time of the upper laser level in the amplifier, pump power noise is low-pass filtered as will be discussed in Section 3.3.4. The pump power noise measurements showed non-stationary behavior and for frequencies above 1 Hz variations up to a factor of three have been observed when the pump power was changed by a fraction of a percent. One should note that all three traces measure power fluctuations of fiber-coupled signals. Hence, the effect of varying coupling efficiency is included.

3.3.3. Frequency fluctuations

In principle the frequency (and hence the phase) of the amplifier output in an oscillator amplifier system is determined by the frequency of the oscillator. Frequency fluctuations of the oscillator directly cause frequency fluctuations of the amplifier. Fluctuations of the amplifier pump power, temperature fluctuations or acoustic noise represent other, significantly smaller sources for frequency noise at the amplifier output. The setup presented in the following section allows the measurement of this excess noise.

Setup

Heterodyne Mach-Zehnder interferometers as shown in Fig. 3.12 have been used for the phase measurements. The setup in Fig. 3.12a has been used for the low-frequency measurements from 10^{-4} Hz up to 0.5 Hz and the one in Fig. 3.12b for measurements from 0.1 Hz up to 100 kHz. In both setups light of a 1064 nm NPRO (Mephisto 800 by

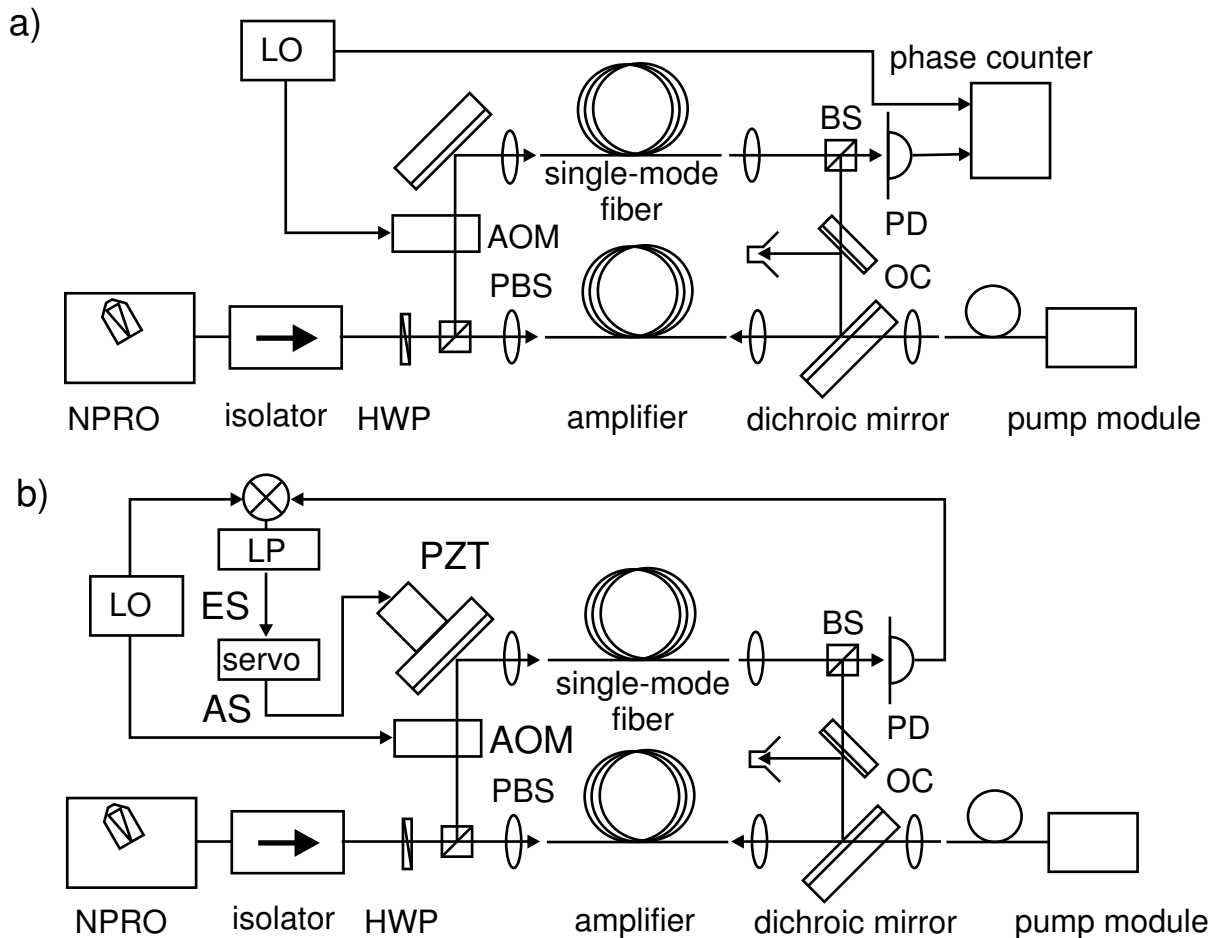


Figure 3.12.: Phase noise measurement setup; a) low-frequency measurement up to 0.5 Hz with phase counter b) interferometer locked, phase measurement from error signal (ES) or actuator signal (AS); acousto-optical modulator AOM, beam splitter BS, half-wave plate HWP, 40 MHz local oscillator LO, non-planar ring oscillator NPRO, output coupler OC, polarizing beam splitter PBS, photodiode PD, piezo-electrically actuated mirror PZT.

Innolight) was shielded from backreflections by an optical isolator. The subsequent half-wave plate (HWP) in combination with the polarizing beam splitter (PBS) was used to adjust the power distribution in the two interferometer arms. One arm contained the fiber amplifier, the other arm contained an acousto-optic modulator (AOM) driven by a 40 MHz local oscillator (LO). The light of both arms was brought to interference

at a beam splitter (BS) and detected by an InGaAs photodiode (PD). In order to obtain interferometer arms with similar length, which reduces the influence of seed laser frequency fluctuations on the interferometer output phase, a 5 m long angle-polished single-mode fiber was inserted after the AOM.

For the low-frequency measurements a phase counter (53132A by Agilent) was used to measure the phase between the 40 MHz signal from the LO and the 40 MHz signal from the PD with the advantage that the interferometer does not need to be locked. Locking the interferometer over many hours would require an actuator with a large dynamic range which was not available. Since the phase counter could be read out with 1 Hz, spectral estimates up to the Nyquist frequency of 0.5 Hz could be obtained. The possible effect of aliasing has been estimated to less than $0.14 \text{ rad}/\sqrt{\text{Hz}}$ using the high-frequency measurements described below and found to be negligible.

For the high-frequency measurements the interferometer was locked to constant output phase with the advantage that phase information can be obtained at high frequencies. The drawback is that the dynamic range of the PZT-mirror limited the measurement time to a few minutes. As shown in Fig 3.12b, mirror M1 has been replaced by a mirror with a longitudinal PZT actuator. The 40 MHz photodiode signal has been mixed down with the LO signal in a double-balanced mixer with subsequent 100 kHz low-pass filter. A preamplifier (SRS560 by Stanford Research Systems) and an integrator as servo have been used to lock the interferometer output phase. By changing the gain of the preamplifier, the unity gain frequency of the interferometer control loop could be varied between 47 Hz and 3 kHz.

When the interferometer was locked with a bandwidth of 47 Hz, the error signal was used as measure for the fiber amplifier phase noise for Fourier frequencies above 400 Hz. Phase noise measurements between 0.02 Hz and 400 Hz have been performed by locking the interferometer with 3 kHz unity gain frequency and measuring the PZT actuator signal. The respective signal was fed to a commercial spectrum analyzer (SR785 by Stanford Research Systems).

Results

Figure 3.13 shows the measurement results obtained with setup a. The solid curve shows the excess phase noise produced by the pumped fiber amplifier while the curve “unpumped” is an estimate for the measurement sensitivity of the setup, measured with the unpumped amplifier. In comparison to preliminary experiments (not shown) with the unpumped amplifier, the noise floor could be reduced by up to an order of magnitude to reach the level presented here by placing the setup in an isolation housing thereby suppressing air convection. Towards 0.1 mHz and 0.5 Hz, the solid curve approaches the curve “unpumped”, which means that the measurement result is limited by the sensitivity of the setup. Towards 0.5 Hz the measurement sensitivity was limited by the phase counter: the curve “func. gen.” has been obtained by feeding two identical 40 MHz signals from a function generator to the phase counter. Towards 0.1 mHz the measurement was limited by frequency noise of the seed laser because the interferometer was not fully balanced: a dependency of interferometer phase to frequency changes of 46.8 rad/GHz

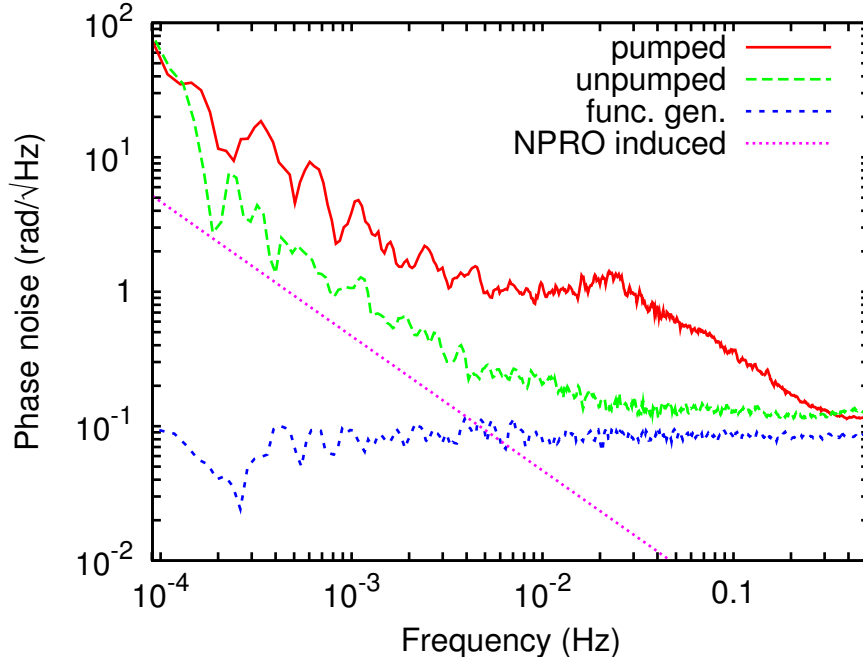


Figure 3.13.: Low-frequency phase noise in fiber amplifier and limiting noise sources measured with heterodyne interferometer shown in Fig. 3.12 a).

which corresponds to an optical interferometer armlength difference of 2.2m was measured. The laser frequency noise density as function of Fourier frequency f follows a $1/f$ -slope and was estimated as $10 \text{ kHz}/\sqrt{\text{Hz}}$ at 1 Hz (Burdack et al., 2004). The curve “NPRO induced” shows the resulting phase noise induced by the seed laser frequency noise, where the measured coefficient and the cited typical frequency fluctuations have been used.

Figure 3.14 shows the results of the phase noise measurements obtained with setup b. The solid curve represents the measured phase noise of the pumped fiber amplifier, the dashed curve represents the phase noise of the unpumped fiber amplifier, which is a measure for the sensitivity of the setup. It is visible that the curve of the pumped amplifier is significantly above the curve of the unpumped amplifier, i. e. the interferometer is sensitive enough to measure excess phase noise of the fiber amplifier. The roll-off at 7 kHz of the curve labelled “pumped” can be explained by filtering effects due to the effective lifetime of the upper laser level in the fiber amplifier as discussed below. The transfer function from pump power to phase at the interferometer output was measured. The resulting transfer function has the shape of a low-pass filter with a corner frequency of 7 kHz. The transfer function from pump power to amplifier output power also shows low-pass filter characteristics with the same corner frequency which indicates that the same physical mechanism might be present in both cases: pump power variations slower than the corner frequency are translated to output power and phase variations of the amplifier.

For faster frequencies than 7 kHz, the inversion cannot follow the pump power vari-

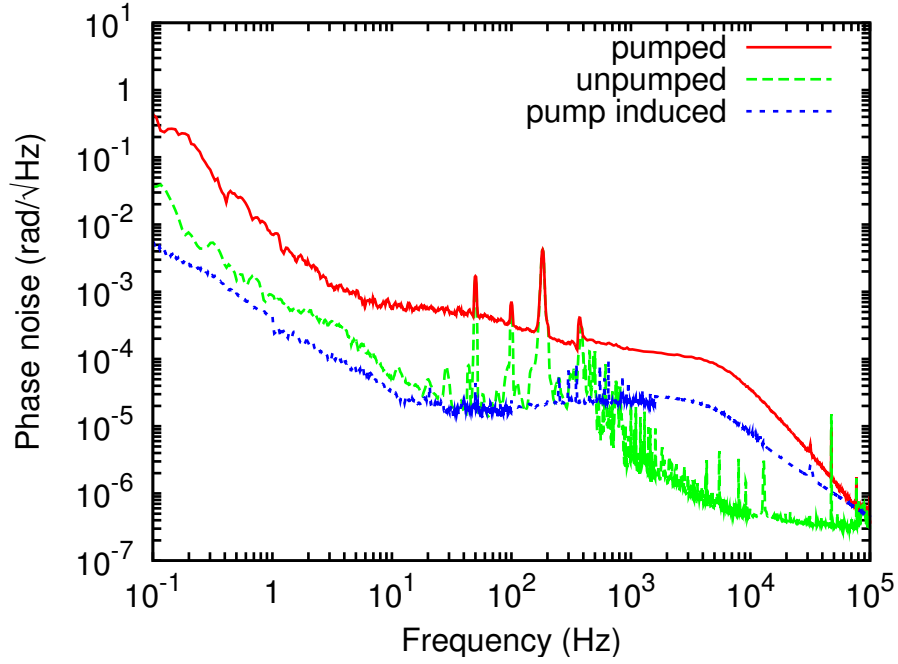


Figure 3.14.: High-frequency phase noise in fiber amplifier measured with locked heterodyne interferometer as shown in Fig. 3.12 b).

ations and the effective lifetime of the Yb^{3+} -ions acts as a low-pass filter. Multiple mechanisms are possible for phase changes due to pump power changes: heat generating processes from the upper laser level, direct modulation of the refractive index due to modulation of the inversion, and the nonlinear refractive index in combination with pump induced amplifier power fluctuations. The magnitude of latter effect has been estimated and found to be negligible. From the nonlinear refractive index of glass, $n_2(\text{glass}) = 3 \cdot 10^{-20} \text{ m}^2/\text{W}$ (Fellegara et al., 1997), the transfer function from pump power changes to phase changes was measured and a transfer function a factor 170 below the measured transfer function was found.

The trace “pump induced” shows the influence of pump power noise on phase noise of the pumped amplifier. It was obtained by multiplying the measured power noise of the pump radiation (see Section 3.3.2) by the transfer function from pump power noise to phase noise (see Section 3.3.4). The trace “pump induced” indicates that pump power noise is a relevant contributor to the phase noise of the pumped amplifier.

The data from Figs. 3.13 and 3.14 have been converted from phase noise $S_\phi(f)$ in units of $\text{rad}/\sqrt{\text{Hz}}$ to frequency noise $S_\nu(f)$ in units of $\text{Hz}/\sqrt{\text{Hz}}$ by Eq. (3.1). In the derivation, ν denotes laser frequency, ϕ laser phase, and f Fourier frequency.

$$\begin{aligned}
 \nu &= \frac{\omega}{2\pi} = \frac{1}{2\pi} \frac{d}{dt} \phi \\
 S_\nu &= \frac{1}{2\pi} s S_\phi = \frac{1}{2\pi} (2\pi f) S_\phi = f \cdot S_\phi \\
 S_\nu(f) &= f \cdot S_\phi(f)
 \end{aligned} \tag{3.1}$$

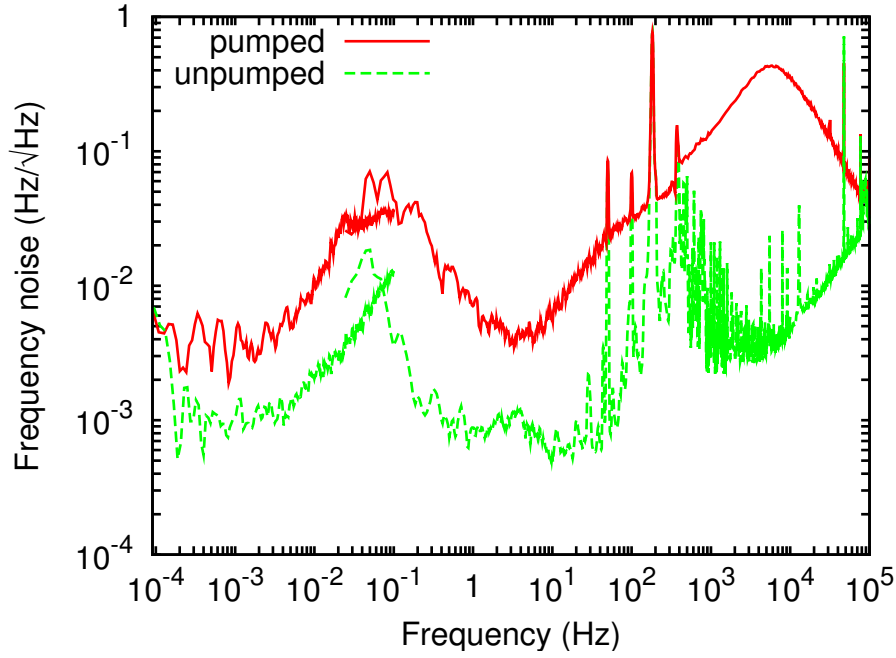


Figure 3.15.: Combined phase noise measurements of fiber amplifier (Figs. 3.13 and 3.14) scaled as frequency noise.

The resulting frequency noise spectral densities have been plotted in Fig. 3.15. Since the phase noise measurement in Fig. 3.13 was limited by the sensitivity of the interferometer (demanding a signal-to-noise ratio of 3) for frequencies towards 0.5 Hz, the data between 0.1 Hz and 0.5 Hz have not been shown. Despite having been measured with two different setups, the two sets of measurements fit well. The highest excess frequency noise of the fiber amplifier has been measured as $0.4 \text{ Hz}/\sqrt{\text{Hz}}$ at 6 kHz.

The excess frequency noise of the fiber amplifier in the kHz frequency range is mainly dominated by pump power noise as has been analyzed in the high-frequency phase noise measurements shown in Fig. 3.14. In the mHz range pump power noise does not seem to be the dominating noise source. Instead, comparisons of ambient air temperature fluctuations above the amplifier for unpumped and pumped operation indicate higher temperature noise levels for pumped operation, which could be the dominating noise source for phase noise at mHz frequencies. Measurements showing lower phase-noise of the pumped amplifier might be obtained by further reducing the air convection or even by operation in vacuum.

3.3.4. Power and frequency actuators

The frequency and power stabilities presented in the preceding sections need to be actively improved for LISA to reach its design sensitivity. The simultaneous control of frequency and power requires separate actuators for both parameters. The frequency can be controlled by controlling the seed laser frequency. A PZT crystal glued onto the laser

crystal of the NPRO is a commonly used actuator for its frequency. As will be shown in the following, the control of the output power requires two actuators: modulation of seed laser pump current and modulation of amplifier pump current are possible actuators.

The investigations discussed in Section 3.3.3 have shown that pump power variations also induce amplifier phase variations. In non-planar ring oscillators it is known that pump power variations change the laser frequency and a parasitic effect of signals applied to the NPRO PZT on the laser output power has also been measured (Quetschke, 2003). Experiments on pump power induced laser frequency control have been reported by Willke et al. (2000) and Heurs et al. (2004).

The design of optimized control loops requires the knowledge of the dynamic behavior of the laser system. Therefore, transfer functions from the seed laser PZT to laser frequency and from seed laser pump power and amplifier pump power to output power are presented.

Figure 3.16 shows the measured transfer function from relative seed laser power variations to relative amplifier output power variations. It has been obtained by modulating

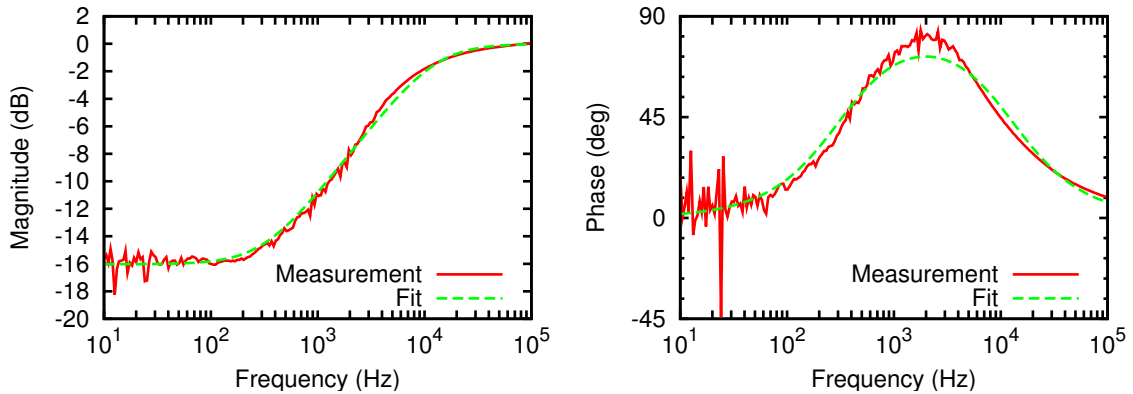


Figure 3.16.: Measured transfer function from relative seed laser power variations to relative amplifier output power variations.

the seed laser pump current, measuring the seed laser output power and the amplifier output power. The transfer function has the shape of a high-pass filter with DC-bypass.

In a saturated amplifier, slow seed laser power variations of 1 mW translate to output power variations of 1 mW, since an increase in seed power reduces the inversion and hence the gain in the amplifier. The transfer function for the relative power variations is hence $1/G$. For modulation frequencies above the inverse lifetime of the upper laser level, the inversion cannot follow the seed power changes, and a seed power modulation of ΔP_s translates to

$$\Delta P_o = G \times \Delta P_s \quad (3.2)$$

of output power modulation where

$$G = \frac{P_o}{P_s} \quad (3.3)$$

is the gain of the amplifier. Hence, the amplifier acts as a linear amplifier for high modulation frequencies. Then, using Eqs. (3.2) and (3.3) the transfer function from relative seed power variations to relative output power variations equals 1:

$$\frac{\Delta P_o/P_o}{\Delta P_s/P_s} = \frac{\Delta P_o}{\Delta P_s} \cdot \frac{P_s}{P_o} = G \cdot \frac{1}{G} = 1 \quad (3.4)$$

Hence, for a fully saturated amplifier the amplifier gain $G = g_{\text{sat}}$ can be read from the difference between the low-frequency and the high-frequency amplifier response as discussed below.

The high-pass filter shape with DC bandpass shown in Fig. 3.16 can mathematically be modelled by the product of a real zero at frequency f_2 and a real pole at frequency f_3 with a scaling factor H_2 as shown in Eq. (3.5).

$$H_2(f) = H_2 \left(1 + i \frac{f}{f_2} \right) \left(1 + i \frac{f}{f_3} \right)^{-1} \quad (3.5)$$

Equation (3.5) has been fitted to the measured complex transfer function and $f_2 = 313$ Hz and $f_3 = 12.6$ kHz have been obtained. This and the following mathematical models can be found in e.g. Dorf (1992).

From the high-frequency limit

$$H_2(f) \approx H_2 f_3 / f_2 \quad \text{for } f \gg f_2, f_3 \quad (3.6)$$

and the fact that the relative transfer function approaches 1, it follows that the scaling factor is given by $H_2 = f_2 / f_3$.

The fit of Eq. 3.5 to the data of Fig. 3.16 and all following fits have been carried out with the complex logarithm of the data to account for the large variations in magnitude as explained below. From the measured magnitude r and phase ϕ , the complex transfer function $z = r \cdot \exp(i\phi)$ has been obtained, where r , ϕ , and z depend on frequency. When performing a least square fit of $H_2(f)$ to the complex transfer function z obtained from Fig. 3.16, a faithful representation of the measured data by the fit function is complicated by the large variations in magnitude, i.e. a fit to the data between 10 Hz and 100 Hz is likely to be inaccurate due to the low magnitude in this frequency range. More accurate fits are obtained by fitting the logarithm $\log(z) = \log(r) + i\phi$ of the measured data to the logarithm of the fit function. Another possibility for fitting analytic functions to measured data is given by the program LISO developed by G. Heinzel (Heinzel, 1999, Appendix C) that uses real and imaginary part of complex numbers for fitting and allows different weightings for the data.

With the fitted values for f_2 and f_3 in Eq. (3.5) a saturated gain of $g_{\text{sat}} = 40$ results. The amplifier on the other hand produced 1 W of output power from 10 mW of seed power which corresponds to an overall gain of $G = 100$ (20 dB). This means the amplifier was not fully saturated. As model for the not fully saturated amplifier a purely linear amplifier with gain g_{lin} and a fully saturated amplifier with gain g_{sat} in series are

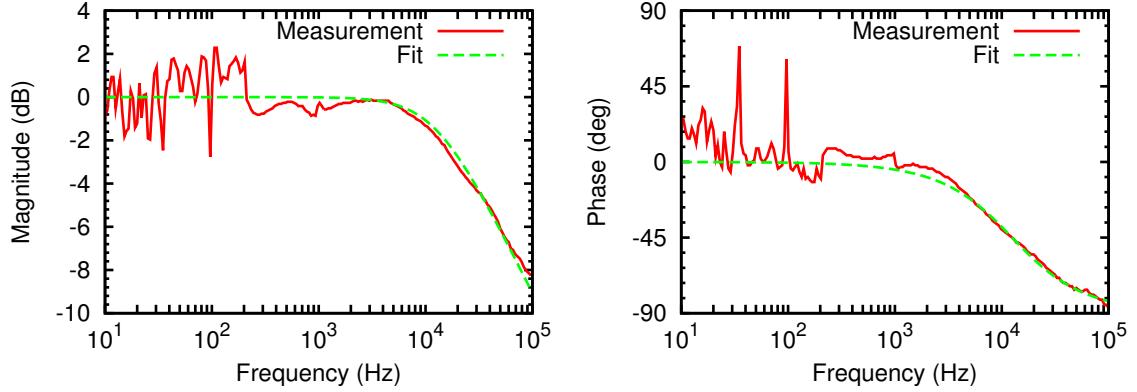


Figure 3.17.: Measured transfer function from relative pump power variations to relative amplifier output power variations.

used. The overall gain $G = g_{\text{lin}} \cdot g_{\text{sat}}$ then is the product of linear gain $g_{\text{lin}} = 2.5$ and saturated gain $g_{\text{sat}} = 40$. This can be compared to the theoretical saturation power

$$P_{\text{sat}} = I_{\text{sat}} \cdot \pi r^2 \quad (3.7)$$

where $r = 2.6 \mu\text{m}$ is the radius of the fiber core, and (Weßels, 2004, p. 44)

$$I_{\text{sat}} = \frac{h\nu}{\tau\sigma_{\text{em}}} \quad (3.8)$$

is the saturation intensity with Planck constant h , laser frequency ν , lifetime of the upper laser level τ , and emission cross-section $\sigma_{\text{em}} = 0.3 \cdot 10^{-24} \text{m}^2$ of Ytterbium at the laser wavelength of 1064 nm. For 1064 nm wavelength (corresponding to a frequency $\nu = 282 \text{THz}$) and a lifetime of the upper laser level of $\tau = 850 \mu\text{s}$, a theoretical saturation power of 15.5 mW results. With 10 mW of seed power as were used, the amplifier was not fully saturated.

For frequencies below f_2 , seed laser power modulation is not a suitable actuator because relative seed laser power modulations are suppressed by the saturated gain of the amplifier and large absolute seed laser power variations would be required. Above f_3 power modulation of the seed laser is a good power actuator of the overall system.

Figure 3.17 shows the transfer function from relative amplifier pump power variations to relative amplifier output power variations. The pump current of the fiber amplifier pump diode has been modulated and the transfer function to amplifier output power has been measured. The transfer function has the shape of a low-pass filter, where the corner frequency f_4 is given by the inverse effective lifetime of the upper laser level in the amplifier.

The pole shown in Eq. (3.9) has been fitted to the measured complex transfer function and $f_4 = 12.5 \text{kHz}$ has been obtained.

$$H_3(f) = \frac{H_3}{1 + i\frac{f}{f_4}} \quad (3.9)$$

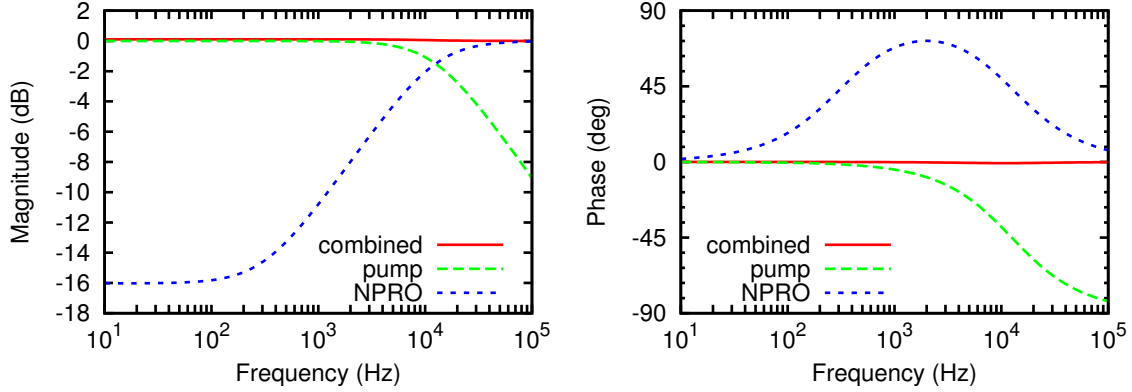


Figure 3.18.: Transfer function from relative seed laser power variations to relative amplifier output power, relative amplifier pump power to relative amplifier output power, and combined transfer function.

Since amplifier pump current variations directly modulate the amplifier inversion and hence the amplifier gain, the transfer function of relative pump power variations to relative output power variations approaches 0 dB towards DC ($H_3 = 1$). The higher corner frequency of 12.5 kHz compared to 7 kHz as measured in Section 3.3.3 is due to a higher pump power in the transfer function measurements since the effective lifetime of the upper laser level depends on the pump power (Desurvire, 1994).

Pump current is a good actuator for the amplifier output power for frequencies below f_4 . For higher frequencies, high pump current changes would only lead to small amplifier output power variations.

Seed laser pump current modulation and amplifier pump current modulation are each not sufficient as actuators but the sum of both is a suitable actuator. To prove this, the sum of the fit-functions (Eqs. (3.5), (3.9)) has been plotted in Fig. 3.18. The magnitude and phase of the sum have been plotted as trace “combined” in Fig. 3.18. The magnitude of the combined transfer function is flat and the phase is zero with only a tiny wiggle at the cross-over frequency around 12.5 kHz. One should note that the complex functions have been added.

Figure 3.19 shows the measured transfer function from signals applied to the seed laser PZT to laser frequency behind the amplifier. Two measurements were performed to obtain Fig. 3.19: the shape of the graphs has been determined with the setup shown in Fig. 3.12 b), where the interferometer output phase was locked with a bandwidth of 47 Hz and the transfer function from laser PZT to interferometer phase error signal has been measured. Due to the unequal interferometer arms, laser frequency changes directly translate to phase changes at the interferometer output. The overall gain of the transfer function (the frequency tuning coefficient at DC) was obtained using a scanning Fabry-Perot interferometer.

The measured transfer function was flat and the DC-frequency tuning coefficient was measured as 1.67 MHz/V. Typically, the first mechanical resonance of the PZT can be found around or above 100 kHz and a PZT resonance of an NPRO can be fitted by a

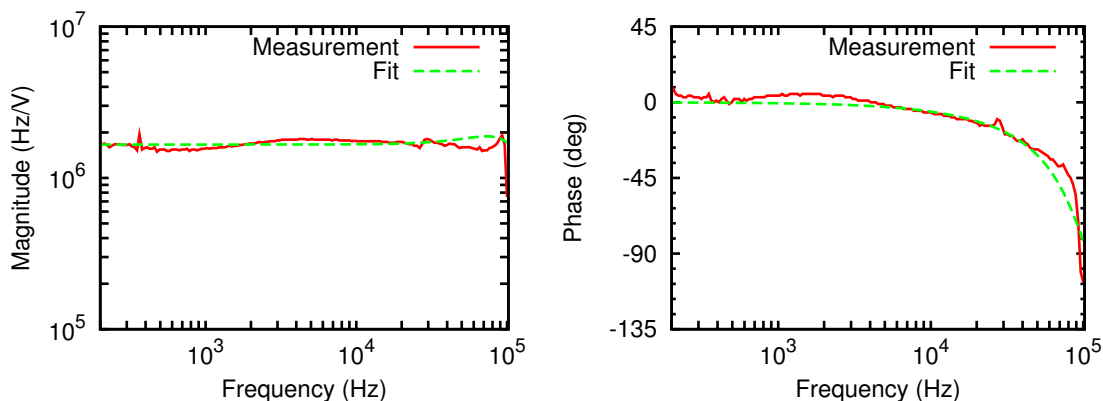


Figure 3.19.: Measured frequency tuning efficiency of seed laser PZT; the data have been measured as transfer function from seed laser PZT to interferometer output phase with 47 Hz locking bandwidth of the interferometer; the DC level has been determined in a separate measurement using a scanning Fabry-Perot interferometer.

complex pole. However, since the transfer function is flat up to 100 kHz and data at higher frequency were not available, no faithful fit was possible.

The PZT is a suitable frequency actuator for a master oscillator fiber power amplifier system using an NPRO and an Yb-doped fiber amplifier since it changes the frequency of the amplifier output radiation with a flat transfer function up to a frequency of approximately 100 kHz.

3.3.5. Conclusions

In conclusion, sensitive power- and frequency-noise measurements of an Yb-doped fiber amplifier have been presented and actuators for power and frequency stabilization have been investigated. Table 3.3 shows the LISA requirements and the measured values of the fiber amplifier. The amplifier emitted 1 W of output power in a single longitudinal and transverse mode with a polarization contrast of 300:1 from 10 mW of seed power. Due to the broad amplification bandwidth of Yb-doped glass, the center wavelength and frequency tunability are determined by the respective properties of the seed laser. Both center wavelength and tuning range were taken from the datasheet provided by the manufacturer (Mephisto datasheet by Innolight¹).

The free-running relative output power fluctuations of up to $8 \cdot 10^{-3}/\sqrt{\text{Hz}}$ were up to a factor of 40 above the upper limit of $2 \cdot 10^{-4}/\sqrt{\text{Hz}}$ for frequencies between 0.1 mHz and 10 Hz. Suitable actuators for stabilization of the amplifier output power have been identified: the seed laser pump current and the amplifier pump current.

The excess frequency noise produced by the fiber amplifier in the LISA measurement window was below $0.1 \text{ Hz}/\sqrt{\text{Hz}}$, which is significantly (at least four orders of magnitude) below the free-running frequency fluctuations of a free-running NPRO.

¹http://www.innolight.de/products/mephisto/INNOLIGHT_Mephisto.pdf

Parameter	Unit	Requirement	Measurement
Output power	W	1	1
Longitudinal mode		single-frequency	single-frequency
Transverse mode		TEM ₀₀	TEM ₀₀
Wavelength	nm	1064	1064.5
Frequency tuning range	GHz	10	30
Polarization contrast	1	> 100 : 1	> 300 : 1
Rel. power fluctuations	1/ $\sqrt{\text{Hz}}$	$< 2 \cdot 10^{-4}$	$< 8 \cdot 10^{-3}$
Frequency fluctuations	Hz/ $\sqrt{\text{Hz}}$	< 30	< 0.1

Table 3.3.: Required and measured parameters for fiber amplifier. The upper limit for relative power fluctuations is given for frequencies ranging from 0.1 mHz to 10 Hz, the upper limit for frequency fluctuations is specified for frequencies between 1 mHz and 1 Hz. The free-running (unstabilized) power and frequency fluctuations are compared to the LISA requirements.

The master-oscillator power-amplifier system is a suitable laser source for the gravitational wave detector LISA. The excess power fluctuations of the amplifier have to be stabilized to reach the LISA specifications and the excess frequency fluctuations of the amplifier are negligible compared to the frequency fluctuations of free-running non-planar ring oscillators. Suitable actuators for both power and frequency have been identified and characterized.

3.4. Low-power distributed-feedback fiber laser

The suitability of a DFB fiber laser as a master oscillator for LISA has been investigated. The laser is described in Section 3.4.1. It has been investigated concerning the requirements given in Table 3.1 and the experiments and results are discussed below.

The measurement of the dynamic frequency actuator characteristics and the measurement of the free-running frequency fluctuations required the frequency stabilization of the fiber laser, as will be discussed below and is described in Section 3.4.2. Hence, the DFB fiber laser was frequency-stabilized to a stable Fabry-Perot cavity. To my knowledge, the frequency stabilization results presented in Section 3.4.2 are the best published for fiber lasers. The frequency actuator characteristics are described in Section 3.4.3. Relative power fluctuation measurements are discussed in Section 3.4.4 and in Section 3.4.5 the free-running frequency fluctuations of the fiber laser are reported.

3.4.1. Setup, output power, and polarization

The Ytterbium-doped DFB fiber laser (Adjustik Y10 by Koheras A/S (Denmark)) as shown in Fig. 3.20 was characterized. It was pumped at 980 nm by a laser diode and emitted at a wavelength of 1063.8 nm. The laser was operated at 20°C and emitted up



Figure 3.20.: Koheras Adjustik turn-key DFB fiber laser.

to 7.9 mW of output power at a maximum pump current of 220 mA. An average slope efficiency of 0.043 W/A and a threshold current of 44.3 mA were calculated from a linear fit to the measured output power data. Up to a pump current of 180 mA (5.8 mW of output power) a built-in power stabilization was fully operational, for higher currents its noise suppression was reduced, since drops in laser output power could not be compensated anymore. The polarization contrast of the output power was determined by measuring the maximum and minimum transmission through a rotatable polarizer with a rotatable quarter-wave plate between laser and polarizer. For the DFB laser output, a polarization contrast of 990:1 was obtained. When a polarization-maintaining fiber was attached to the laser, it was observed that the output polarization state was not fixed. According to the manufacturer², the laser unit that was available for the experiments was internally not coupled to polarization maintaining fiber, which resulted in non-stationary polarization states of the fiber laser output.

Single-frequency operation was achieved by a Bragg grating written into the active fiber. The laser frequency could be manually tuned by changing the laser temperature. In addition the laser was equipped with a PZT, which strained the fiber Bragg grating and tuned the laser frequency when a voltage was applied. This analogue modulation input was used for frequency stabilization.

3.4.2. Frequency stabilization

To date, frequency stabilization results of erbium-doped fiber lasers with 1.5 μm wavelength have been reported. A standing-wave laser with grating feedback and coupled cavities has been frequency locked to the side of acetylene absorption lines (Gilbert, 1991), a ring laser has been frequency-locked to an external fiber Fabry-Perot resonator (Park et al., 1993) using the Pound-Drever-Hall technique (Drever et al., 1983), a DFB laser has been frequency locked to a Mach-Zehnder interferometer (Cranch, 2002), and a

²Personal communication with Jens Engholm Pedersen, Koheras A/S, March 13th, 2003

distributed Bragg reflector (DBR) laser has been locked to an unbalanced-arm scanning Michelson interferometer (Chung et al., 2001). The free-running frequency noise of two identical Bragg grating lasers has been measured for Fourier frequencies up to 100 kHz (Ball et al., 1994).

The Pound-Drever-Hall scheme (Drever et al., 1983) has been used for frequency stabilization of the fiber laser to a high-finesse optical cavity. Figure 3.21 shows the experimental setup. The light emitted from the DFB fiber laser was sent through an

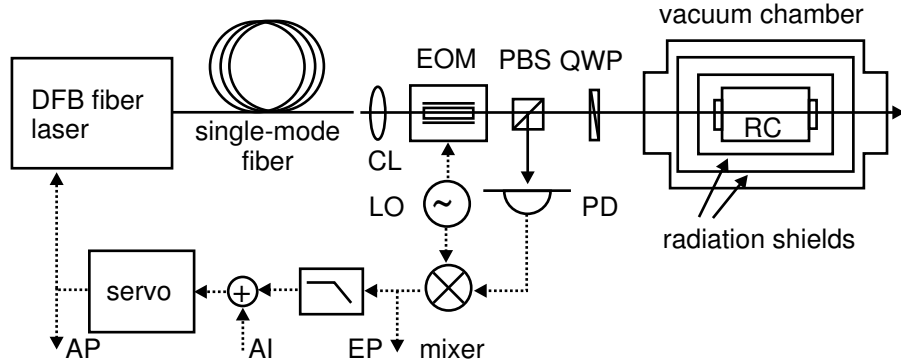


Figure 3.21.: Frequency stabilization setup for the distributed-feedback fiber laser; collimating lens CL, electro-optical phase modulator EOM, polarizing beam splitter PBS, quarter-wave plate QWP, reference cavity RC, photodiode PD, local oscillator LO, error point EP, adder input AI, actuator point AP.

EOM (model 4003 by New Focus) for phase modulation and coupled into the optical reference cavity (RC) made of ultra-low expansion glass (ULE by Corning). Its free spectral range was 714 MHz and its finesse was measured as 9400 as will be described below and in Section 5.1. The cavity was surrounded by radiation shields and placed in a vacuum tank (with a residual pressure of less than 10^{-6} mbar) to reduce temperature fluctuations, acoustic disturbances, and changes in optical resonator length due to residual pressure changes. The radiation shields consisted of gold-coated steel cylinders separated by ceramic spacers (Peterseim, 1999). The EOM was driven by the LO at a frequency of 10 MHz and produced sinusoidal phase modulation with a modulation index of approximately 0.3. Using the PBS and the quarter-wave plate (QWP) in front of the reference cavity, the reflected light was detected by the photodiode (PD). Its signal was mixed with the local oscillator signal and filtered by a 4-pole Tschebyscheff low-pass with a corner frequency of 1 MHz to remove the sum frequency at 20 MHz. The resulting error signal was sent to the servo amplifier that drove the laser frequency actuator. With a servo consisting of a 2-pole low-pass filter at 7.5 kHz and an integrator to 1.7 kHz, a unity-gain frequency of 3 kHz was achieved.

The frequency error signal slope has been calibrated as 6.3 V/MHz at DC. Since the error signal was generated from the sidebands reflected from the cavity input mirror and the carrier leaking out of the reference cavity (Drever et al., 1983), the storage time of the cavity affects the dynamic response of the reference cavity. The storage time of the

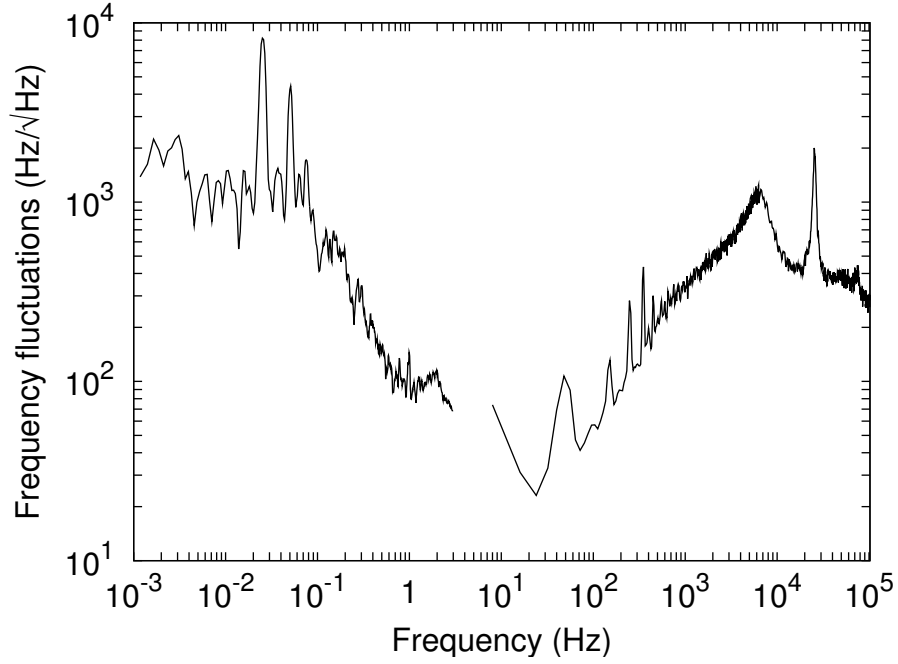


Figure 3.22.: Residual frequency fluctuations of the DFB fiber laser measured at the error point during frequency lock. The frequency stabilization bandwidth was 3 kHz.

reference cavity causes a pole (a low-pass) in the slope of the error signal, where the pole frequency is given by the half-width of the cavity linewidth. The frequency of this pole has been measured as 38 kHz and it has been taken into account in Fig. 3.22 that shows the frequency deviation between reference cavity and laser measured at the error point (EP). The transfer function measurement has also been used to measure the finesse of the cavity. The calibrated in-loop error signal shown as left trace in Fig. 3.22 is a lower limit for the residual frequency fluctuations of the laser, since the error signal does not account for changes of the reference frequency or noise inserted into the control loop between reference cavity and error point. An upper limit for the laser frequency fluctuations cannot be given since neither a second laser at the same wavelength for a beat experiment was available, nor was it possible to generate a second, independent error signal. The left trace was generated from a time series sampled with 10 Hz, resulting in a spectral density with frequencies up to 5 Hz, and the upper trace was combined from measurements using a commercial spectrum analyzer (SR785 by Stanford Research Systems) using resolution bandwidths of 8 Hz and 128 Hz, which resulted in the gap between 5 Hz and 8 Hz. The unity gain frequency of the frequency stabilization loop has been measured as 3 kHz. Hence, for frequencies below 3 kHz, the frequency noise was suppressed by the control loop and for frequencies above 3 kHz the calibrated error signal showed the free-running frequency noise. The peak at 25 kHz was caused by a mechanical resonance in the laser PZT that was not suppressed by the control loop.

The residual frequency noise at the error point that was used to calculate the lower frequency trace in Fig. 3.22 showed peak-to-peak frequency noise of less than 3 kHz during a measurement time in excess of one hour. Residual laser frequency deviations from the reference frequency have been reported: 30 MHz in 30 minutes by Chung et al. (2001), 900 kHz over 10 minutes by Park et al. (1993), and less than 200 kHz in 30 min by Gilbert (1991). Compared to the lowest frequency deviations of 200 kHz reported in Gilbert (1991) the result achieved here represents an improvement of more than a factor of 6.

Although LISA requires significantly lower residual frequency noise than has been shown here, the residual frequency noise that was obtained is sufficiently small for the present application, namely the characterization of the frequency actuator and measurement of the free-running frequency noise of the DFB fiber laser.

3.4.3. Frequency actuators

The laser frequency was manually temperature tunable over 22.7 GHz from 1063.8 nm at 20°C to 1063.88 nm at 31.2°C laser temperature at a pump current of 175 mA, which corresponded to a thermal frequency tuning coefficient of 2 GHz/K. In addition to tuning the laser frequency by manually changing the laser temperature, the laser was equipped with a PZT, which strained the fiber and tuned the laser frequency when a voltage was applied. This analogue modulation input was used for frequency stabilization. The tuning coefficient was measured as 533 MHz/V. Voltages ranging from 0 V to 90 V could be applied to the actuator. Both thermal and piezo-electric tuning coefficients were measured using a wavemeter (WA-1500 by EXFO, former Burleigh). Single-frequency operation was in both cases verified using a scanning Fabry-Perot interferometer (Spectra-Physics 470).

Figure 3.23 shows the fiber laser frequency as function of laser temperature at a pump current of 220 mA. The laser frequency was measured with a wavemeter (WA-1500 by EXFO, former Burleigh) and single-frequency operation was verified with a scanning Fabry-Perot interferometer. A thermal tuning coefficient of 2 GHz/K was obtained from the slope of a linear function that was fitted to the measured data.

Due to the demanding requirements on laser frequency stability in the LISA mission, the frequencies of the LISA lasers will be actively stabilized. For an optimized control loop design, in addition to the ‘static’ frequency tuning coefficient, the knowledge of the dynamic frequency response of the laser frequency actuator is required. It can be extracted from the transfer function from actuator point (AP) to error point (EP) in Fig. 3.21. In addition to the actuator characteristics this transfer function also contains the pole caused by the reference cavity as described in the preceding section. This pole frequency has been measured as 38 kHz in an independent measurement, corresponding to a reference cavity linewidth of 76 kHz (FWHM).

An error signal for frequency stabilization can only be obtained when the laser frequency is within the cavity linewidth, which is not the case when the laser frequency is free-running. Hence, in order to measure the frequency response of the frequency actuator, the laser frequency was locked to the cavity (Fig. 3.21) using the Pound-Drever-Hall

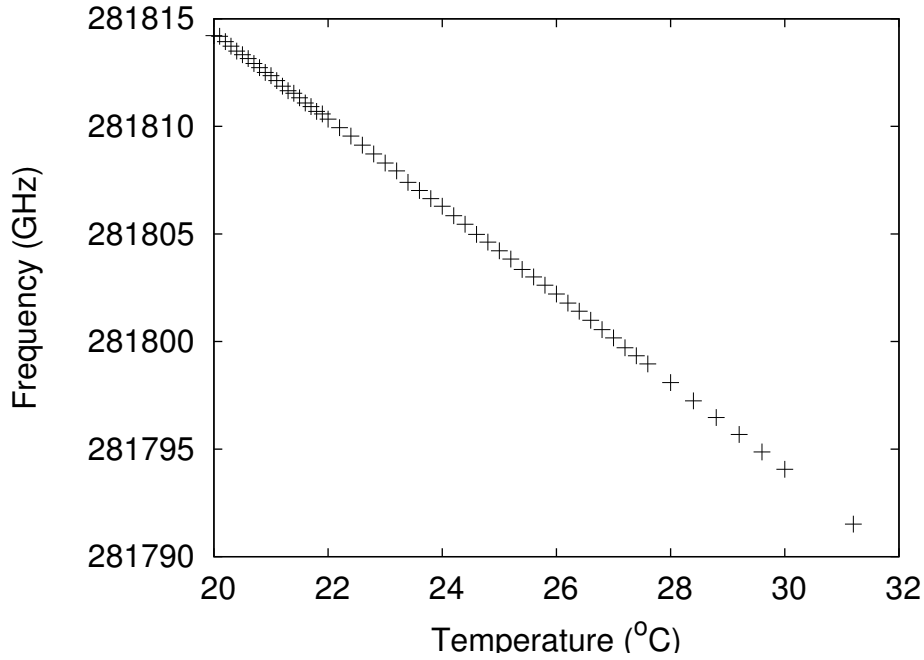


Figure 3.23.: Thermal frequency tuning of the DFB fiber laser. A tuning coefficient of -2 GHz/K was measured.

stabilization scheme (Drever et al., 1983) as described in the preceding section. While the laser frequency was locked, a sinusoidal disturbance signal was inserted into the loop at the adder input (AI) in Fig. 3.21 and its transfer from actuator point AP to error point EP was measured. The resulting transfer function is shown in Fig. 3.24. From 30 Hz to 1 kHz the transfer function is flat, at about 3 kHz it shows a roll-off (a single pole) and at 25 kHz it shows a resonance. The pole was caused by the capacitance of the laser PZT and a resistor at the servo output. The resonance was a mechanical resonance of the laser PZT.

The complex transfer function $H(f)$ from actuator point to error point has been fitted using Gnuplot with a single pole at $f_1 = 2.6$ kHz and a complex pole with frequency $f_2 = 25.3$ kHz and quality factor $Q = 24.2$ for the mechanical resonance.

3.4.4. Power fluctuations

The output power of the DFB fiber laser was measured with a Silicon photo diode (IPL 10050, see Chapter 4) equipped with a transimpedance amplifier. The photodiode signal was subtracted from the signal of a stable voltage reference (AD587) and the difference was amplified and recorded. LPSD was used to calculate spectral densities. Figure 3.25 shows the measured relative power fluctuations. The measurements were performed at an early stage of the work when the temperature dependent detection efficiency of 1%/K temperature change for Silicon photodiodes had not yet been inves-

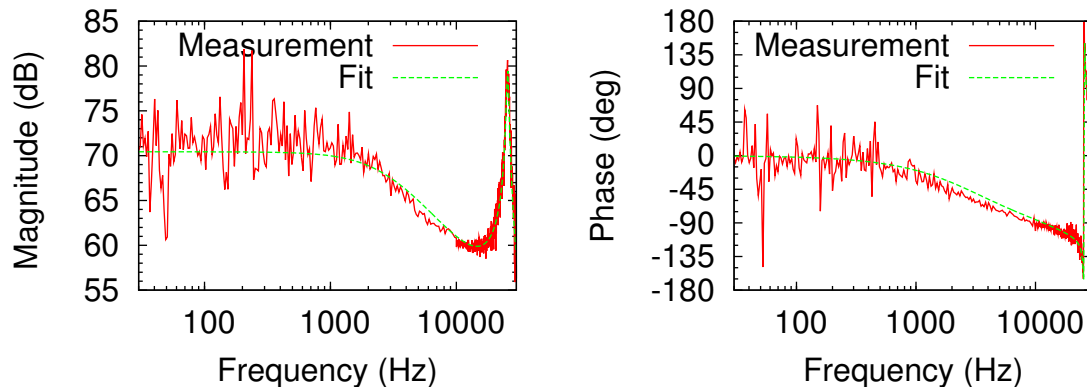


Figure 3.24.: Transfer function of the frequency-locked fiber laser from PZT actuator point to error point of the feedback loop as shown in Fig. 3.21.

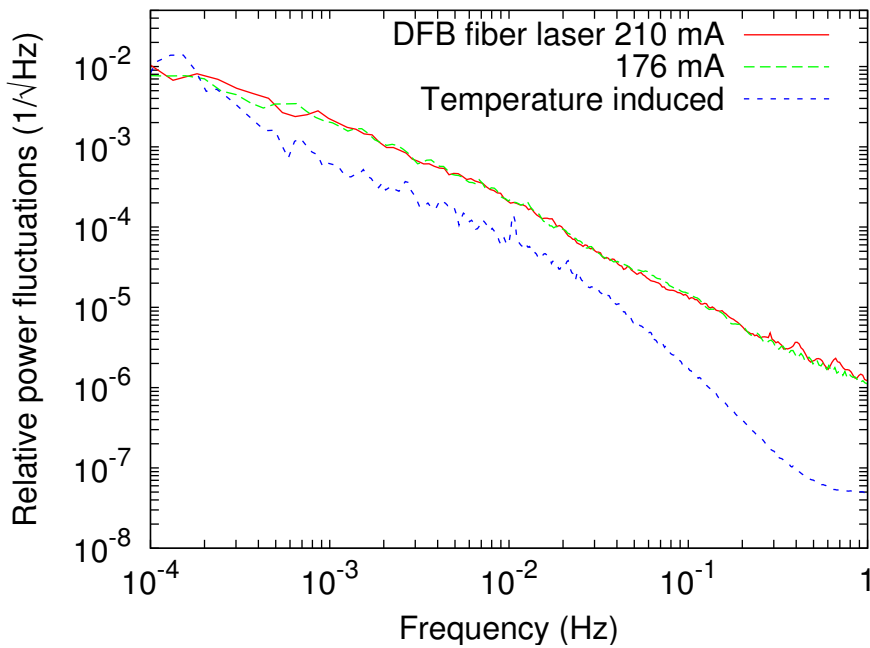


Figure 3.25.: Relative power fluctuations of the DFB fiber laser at two different pump currents measured using non-temperature-stabilized Silicon photodiodes. The effect of temperature fluctuations of the photodiode mount are also shown.

tigated. The power fluctuations were measured using photodiodes without temperature stabilization. Hence, temperature changes of the photodiode led to changes in efficiency which yielded apparent power fluctuations of the laser.

In a separate measurement the temperature fluctuations of the photodiode mount were measured and their effect on the photodiode signal plotted as lowest trace in Fig. 3.25. At 1 Hz the temperature induced power fluctuations were more than order of magnitude below the measured power fluctuations. Towards lower frequencies the factor between measured and induced power fluctuations decreased to about 2 to 3 for frequencies below 30 mHz. This means that the measurement of laser power fluctuations was not fully limited by temperature fluctuations, but temperature fluctuations contributed a significant part (1/3 to 1/2) to the measured power fluctuations. For frequencies below 30 mHz the measured laser power fluctuations should be considered as an upper limit.

For both pump currents, 176 mA and 210 mA the same upper limit of relative power fluctuations can be read from Figure 3.25.

3.4.5. Frequency fluctuations

Due to LISA's laser frequency noise requirements in the $\mu\text{Hz}/\sqrt{\text{Hz}}$ range for frequencies between 1 mHz and 1 Hz, the free-running frequency noise of the laser source should be as low as possible. Since neither a second laser for a beat measurement was available, nor was it possible to generate a frequency error signal when the DFB fiber laser was free-running in frequency, the free-running frequency noise was obtained by locking the laser frequency with the setup shown in Fig. 3.21 and measuring the calibrated actuator signal spectral density. Fig. 3.26 shows the results. If the frequency reference (cavity) and the lock of the laser frequency to the reference frequency can be considered stable, the frequency actuator has to counteract the free-running frequency noise, and the actuator spectral density equals the free-running noise spectral density for Fourier frequencies within the control loop bandwidth. The frequency reference and the frequency lock can be considered sufficiently stable if their noise contributions are small compared to the measured actuator noise. The curve labelled "error point" shows the fiber laser frequency noise measured at the error point and it is visible that this curve lies well below the free-running frequency noise. The curve labelled "reference" has been obtained in an independent measurement, where two identical NPROs have been frequency-locked to the reference cavity used in this experiment and a second, identical, but independent cavity (Tröbs et al., 2002) and the difference frequency fluctuations between both lasers have been measured. The resulting curve is an upper limit for the frequency stability of the frequency reference. It also lies well below the measured actuator spectral densities.

The two upper curves show the free-running frequency noise of the DFB fiber laser obtained from the actuator signal. The laser showed a larger free-running frequency noise for a pump current of 210 mA than for 176 mA, especially for Fourier frequencies above 0.2 Hz. Both power and frequency fluctuations are likely to be caused by pump power fluctuations. From Figure 3.25 that shows identical relative laser power fluctuations for both pump currents it can be concluded that the relative pump power fluctuations were identical for both pump currents. At a higher pump current the absolute fluctuations

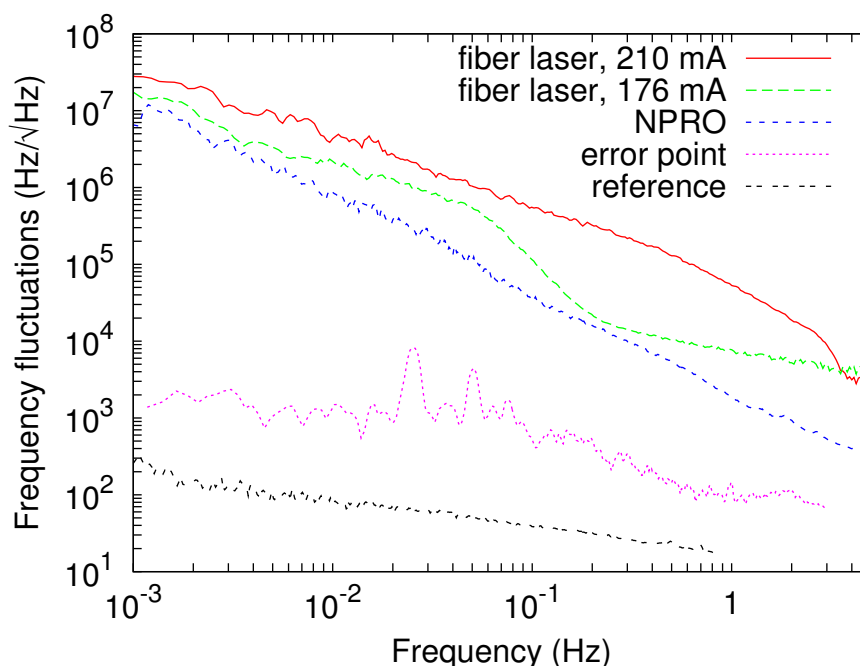


Figure 3.26.: Free-running frequency fluctuations of the DFB fiber laser at two different pump currents obtained from the actuator signal during frequency lock. The frequency stabilization bandwidth was 3 kHz.

of the pump power were hence increased and increased pump power fluctuations led to increased frequency fluctuations. The cause for the reduced frequency fluctuations at 176 mA pump current for frequencies above 0.1 Hz is unknown.

The trace labelled “NPRO” shows the measured free-running frequency noise of a nonplanar ring oscillator emitting 100 mW. Free-running means that the laser was not frequency-locked to an external reference. A beat measurement was performed of the NPRO under test and another NPRO that was locked to the thermally shielded reference cavity described in Section 3.4.2. The free-running frequency noise of the DFB laser at 210 mA pump current was up to a factor of 15 above the free-running frequency noise of the NPRO.

3.4.6. Conclusions

In conclusion a DFB fiber laser at 1063.8 nm has been investigated. Table 3.4 lists the requirements for the LISA laser demonstrator and the measured values of the DFB fiber laser. It emitted up to 7.9 mW in single longitudinal and transverse mode. This amount of output power might not be sufficient for a single-stage amplification to the required power level of 1 W, so that a second, intermediate amplification stage needs to be included.

The DFB fiber laser showed a polarization contrast of up to 990:1, which was signifi-

Parameter	Unit	Requirement	Measurement
Output power	W	1	$7.9 \cdot 10^{-3}$
Longitudinal mode		single-frequency	single-frequency
Transverse mode		TEM ₀₀	TEM ₀₀
Wavelength	nm	1064	1063.8
Frequency tuning range	GHz	10	22.7
Polarization contrast	1	> 100 : 1	990:1
Rel. power fluctuations	$1/\sqrt{\text{Hz}}$	$< 2 \cdot 10^{-4}$	$< 10^{-2}$
Frequency fluctuations	$\text{Hz}/\sqrt{\text{Hz}}$	< 30	$< 3 \cdot 10^7$

Table 3.4.: Required and measured parameters for low-power fiber laser. The upper limit for relative power fluctuations is given for frequencies ranging from 0.1 mHz to 10 Hz, the upper limit for frequency fluctuations is specified for frequencies between 1 mHz and 1 Hz. The free-running (unstabilized) power and frequency fluctuations are compared to the LISA requirements.

cantly above the requirement for LISA. The unit that was available for testing included non-polarization maintaining fiber, so that the output polarization state was not fixed. For use with LISA or for further experiments using such a fiber oscillator, a unit containing only polarization-maintaining fibers would be more advantageous, since polarization variations can be excluded.

For the assessment of center frequency and tuning range it is not important that the laser emits exactly at 1064.0 nm wavelength. Instead, it must be possible to phase-lock all six lasers employed within LISA as was already discussed in Section 3.2.6.

In order to measure the dynamic frequency response of the laser PZT frequency actuator, the laser frequency has been stabilized to the resonance frequency of a stable Fabry-Perot cavity. To my knowledge, the smallest deviations between reference frequency and laser frequency were obtained for frequency-stabilized fiber lasers, i. e. the closest lock of laser frequency to reference frequency was achieved. When the laser frequency was stabilized to a stable Fabry-Perot cavity, the dynamic frequency actuator efficiency was measured. The first mechanical resonance of the laser PZT has been found at 25 kHz, which leads to a PZT bandwidth of a factor of 4 lower than usually encountered in NPROs. A PZT with a higher resonance frequency would be more advantageous for frequency stabilization to the LISA requirements.

The free-running frequency fluctuations of the laser could not be measured by a beat experiment with another stabilized laser, since no second laser at the same wavelength was available. Hence, instead, the fiber laser was frequency locked to a stable Fabry-Perot cavity and the actuator signal was recorded. Since the actuator signal has to counteract the free-running frequency fluctuations, those can be obtained from the actuator signal. Frequency fluctuations of up to $3 \cdot 10^7 \text{ Hz}/\sqrt{\text{Hz}}$ have been measured. This is six orders of magnitude higher than the LISA requirement and up to a factor of 15 above the free-running frequency noise of a low-power NPRO (see Fig. 3.26), but up to a factor of

7 below the free-running frequency noise of the high-power NPRO.

In conclusion, a DFB fiber laser was investigated and characterized as seed oscillator for LISA. In order to measure the frequency actuator bandwidth and the free-running frequency noise, the laser had to be frequency-locked to a Fabry-Perot cavity and the best coupling to the resonance frequency published for fiber lasers was obtained. The fiber laser has demonstrated its potential as seed laser in a power-oscillator master-amplifier laser system for LISA. The frequency actuator bandwidth should be increased to enable even more precise locking to a stable reference, a power modulation input is required to stabilize the output power to an external reference and investigations of the noise properties are necessary when the power is amplified to the 1 W level.

3.5. Discussion

The most promising candidates for LISA lasers are a stand-alone high-power NPRO or a fiber amplifier seeded by a low-power laser. Both concepts have been investigated and can now be compared. As single-stage concept a laboratory version of a LISA laser based on an NPRO has been designed, implemented, and characterized. As fiber amplifier an Ytterbium-doped amplifier has been characterized that can be seeded by a low-power NPRO or by the DFB fiber laser that was characterized.

Table 3.5 shows the LISA specifications for its laser source and the measured data of the single-stage high power NPRO (labelled NPRO), the low-power DFB fiber oscillator (labelled DFB laser), and the fiber amplifier (labelled Amplifier) seeded by a low power NPRO. Single longitudinal and single transverse mode output has been achieved by

Parameter	Unit	Req.	NPRO	DFB laser	Amplifier
Power	W	1	1.2	$7.9 \cdot 10^{-3}$	1
Long. mode			single-frequency		
Transv. mode			TEM ₀₀		
Wavelength	nm	1064	1064.5	1063.8	1064.5
Tuning range	GHz	10	30	22.8	30
Polarization	1	> 100 : 1	830:1	990:1	> 300 : 1
Rel. power fluct.	$1/\sqrt{\text{Hz}}$	$< 2 \cdot 10^{-4}$	$< 10^{-2}$	$< 10^{-2}$	$< 5 \cdot 10^{-3}$
Freq. fluct.	Hz/ $\sqrt{\text{Hz}}$	< 30	$< 2 \cdot 10^8$	$< 3 \cdot 10^7$	< 0.1

Table 3.5.: Required (Req.) and measured parameters for the single stage NPRO (NPRO), the low-power fiber laser (DFB laser), and the Ytterbium-doped fiber amplifier (Amplifier). The upper limit for relative power fluctuations is given for frequencies ranging from 0.1 mHz to 1 Hz, the upper limit for frequency fluctuations is specified for frequencies between 1 mHz and 1 Hz. The free-running (unstabilized) power and frequency fluctuations have been compared with the LISA requirements.

the NPRO-based laser demonstrator, the DFB oscillator, and the amplifier seeded by a

low-power NPRO.

For wavelength and tuning range more precise requirements are necessary. A frequency overlap must exist for all offset-phase-locked lasers and specifications can be given, when the parameters of the offset-phase-lock have been defined. Hence, wavelength and tuning range will not be further discussed here.

The DFB fiber oscillator seems in principle suitable for LISA, however, due to its low output power and the low bandwidth of the frequency actuator, more investigations and probably changes are necessary that are out of the scope of this work. Hence, in the following, the single-stage high-power NPRO will be compared with the fiber amplifier seeded by a low-power NPRO.

Both the single-stage high-power NPRO and the amplifier seeded by a low-power NPRO fulfilled the unstabilized LISA requirements and both need to be stabilized in output power. The power fluctuations of the high power NPRO need to be suppressed by a factor of up to 100 and in the case of low-power NPRO and amplifier, the power fluctuations of the amplifier need to be suppressed by a factor of 50. The relative seed laser power fluctuations are suppressed by the amplifier gain (100 in the experiments). Using the measured output power fluctuations of the low-power NPRO shown in Fig. 3.8 of up to $2 \cdot 10^{-2}/\sqrt{\text{Hz}}$, this results in residual power fluctuations due to the low-power NPRO in the same order of magnitude as the LISA requirements. The power stabilization of the master-oscillator power-amplifier combination requires in principle the use of two actuators: the amplifier pump power for low frequencies and the seed laser pump power for high frequencies. Due to the low noise suppression required, the use of the amplifier pump power as single actuator should be sufficient. It should be possible to stabilize both systems with comparable effort and, based on Table 3.5, no clear advantage or disadvantage can be identified for the one or the other system.

In addition to power, both systems, the single-stage NPRO and the fiber amplifier seeded by a low-power NPRO need to be stabilized in frequency. In both cases the frequency stabilization uses the same actuators. Since the low-power NPRO shows smaller frequency fluctuations in the LISA measurement window than the high-power NPRO, more loop gain is required to stabilize the high-power NPRO. Due to sufficient frequency actuator bandwidth in both cases, this should not pose difficulties.

For spaceborne systems, a small number of components is advantageous, because this reduces system complexity and launch costs. Since the single-stage NPRO showed higher frequency fluctuations than the low-power NPRO, greater care needs to be taken when the frequency of the higher power NPRO is stabilized. If on the other hand, its frequency can be stabilized to the levels required, it should also be possible to stabilize the master-oscillator power-amplifier system. Since the fiber amplifier did not represent an optimized system, more development would be necessary to increase its efficiency, since high efficiency is desired for spaceborne systems and the single-stage high-power NPRO will be stabilized in power and frequency, as is reported on in Chapters 4 and 5.

4. Power stabilization

Although NPROs achieve shot-noise limited operation at MHz frequencies, the laser output is dominated by technical noise such as pump power noise in the LISA measurement window between 0.1 mHz and 1 Hz (Harb et al., 1997). The NPRO-based laser demonstrator discussed in Section 3.2 showed relative output power fluctuations up to 10^{-2} while LISA can only tolerate fluctuations below $2 \cdot 10^{-4}/\sqrt{\text{Hz}}$ (ESA-SCI 11, 2000, p. 77). Hence, an active power stabilization (see e.g. Appendix B) is required for LISA. A fraction of the optical power will be split off the main beam and detected by a photodetector. The resulting signal will be compared to a reference voltage, the difference appropriately amplified and fed back to act on the laser pump power.

Instead of using the pump power as actuator for the laser output power, a number of external actuators have been used for laser power stabilization such as an EOM in combination with a polarizing beam splitter (Conti et al., 2000), an AOM (Kasai and Ishizu, 1994), or an external power modulator called “quantum-well modulator” (Shoop et al., 1992).

Power stabilization by electronic feedback to the pump diode current has been demonstrated for NPROs (Kane, 1990; Harb et al., 1994; Rowen et al., 1994; Rottengatter, 1998), for a ring Nd:YVO₄-KTP green laser (Zhang et al., 2001), and an injection locked Nd:YAG laser (Seifert, 2002). Results have been presented for frequencies above 1 Hz, which is not applicable to LISA.

Without detecting the laser output power, low-power-noise operation of Nd:YVO₄ microchip lasers has been achieved at MHz frequencies by pump-noise suppression (Becher and Boller, 1999). When its frequency was stabilized by acting on the pump current, an NPRO pumped by a single-mode diode laser showed power noise suppression for frequencies above 2 Hz (Heurs et al., 2004; Heurs, 2004). A smaller suppression of power noise of 10 dB was found, when a multi-mode diode laser was used as pump source (Willke et al., 2000). Active pump power stabilization has shown a suppression of up to 6 dB in the output of an NPRO (Rottengatter, 1998). The power noise suppression demonstrated by the various “indirect methods” cited above is however not sufficient for LISA and a detection of the output power and its active stabilization is necessary.

To date, no frequency resolved power fluctuations have been reported for the LISA measurement window ranging from 0.1 mHz to 1 Hz. A relative power stability of $6 \cdot 10^{-3}$ over 1 h has been achieved for a laser diode at 1330 nm wavelength emitting 5 mW of output power (Corredera et al., 2000). The emission of a Kr⁺ laser was power stabilized to better than $2.5 \cdot 10^{-5}$ over 5 h in the visible (Fischer and Lei, 1993) at power levels up to 1 mW. Both references show that power stabilization of lasers to a high accuracy

is possible, however, the lasers and the powers that have been used are not suitable for LISA and the results have not been presented as spectral densities of relative power fluctuations, as is required for LISA.

In this Chapter, the active power stabilization of the NPRO-based laser demonstrator discussed in Section 3.2 will be described. The output power emitted from the laser demonstrator will be monitored, the resulting signal compared with a reference voltage, the difference appropriately amplified, and the pump power of the laser used as actuator. The setup and the experiments will be described in Section 4.1.

Since the stability of the laser output power is limited by the stability of the voltage reference, they are characterized in Section 4.2. Two different noise sources are analyzed: Internal noise that is generated within the reference and the effect of external noise on the reference. The dominating external noise source were temperature fluctuations of the reference.

Power stabilization results obtained with the laser demonstrator are presented in Section 4.3. The best results that have been obtained are described as well as the influence of external noise sources and the usage of different photodiodes. Silicon (Si), Germanium (Ge), and Indium Gallium Arsenide (InGaAs) photodiodes were used. Contrary to expectations, the results obtained with InGaAs photodiodes showed larger power fluctuations than the ones measured with Ge and Si photodiodes.

Detailed noise investigations have been performed to identify the cause for the reduced performance when InGaAs photodiodes were used and to identify the influence of various noise sources on the measured power fluctuations. Although the cause for the reduced performance with InGaAs photodiodes was not uncovered, important noise sources have been identified and characterized. Practically of most concern were the temperature dependencies of photodiode efficiency (Section 4.4.3) and beam splitting ratio (Section 4.4.5). Position-dependent photodiode efficiencies were investigated in Section 4.4.4 to estimate the effect of beam jitter on photodiode signals. Other noise sources that were investigated include the inevitable shot noise (Section 4.4.1) and photodiode dark current (Section 4.4.2).

4.1. Experiments

Figure 4.1 shows the power stabilization setup of the LISA laser demonstrator schematically. The light emitted from the laser demonstrator (1 W of output power) was collimated to a beam with 1 mm radius. A Glan-air polarizer (PBS) with a polarization contrast of 10^7 as specified by the manufacturer (Bernhard Halle Nachfl. GmbH, Berlin) ensured purely s-polarized light¹. A fraction of the beam was sampled by a quartz glass wedge (0.5° wedge angle) and directed to a temperature-stabilized photodetector. A pin-hole (not shown) shielded the photodetector from the reflection of the back surface and a neutral density filter was used to reduce the photocurrent to values between 0.5 mA and

¹Later, the measurements were repeated without the polarizer and the same results could be obtained. This showed that polarization changes were not the limiting noise source. However, in all measurements shown in this Chapter, the polarizer was used within the setup.

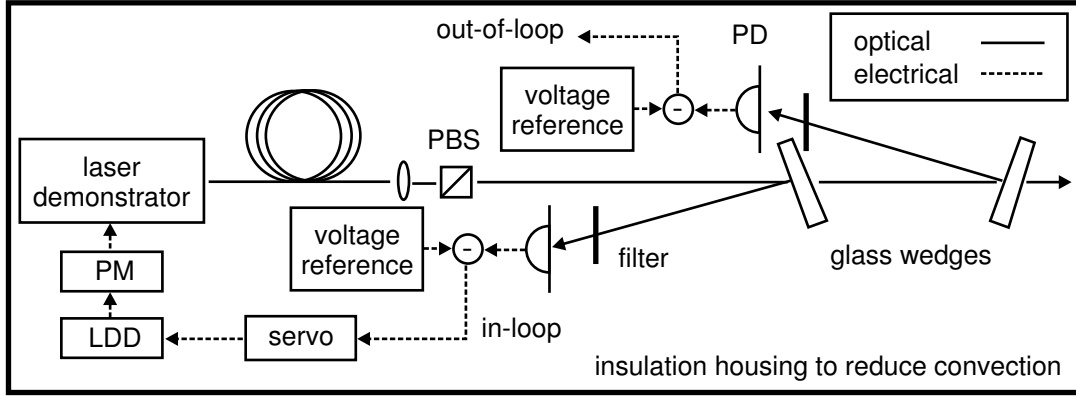


Figure 4.1.: Power stabilization setup of the LISA laser demonstrator; Glan-air polarizer PBS, photodetector PD, laser diode driver LDD, pump module PM.

2 mA depending on the photodetectors used. The photodetector signal was subtracted from a filtered voltage reference (AD587) to generate the (so-called in-loop) error signal. A servo consisting of an integrator was used to feed back the error signal to the pump current of the laser demonstrator via the current modulation input of the laser diode driver. A second, nominally identical error signal was generated independently and used as out-of-loop measurement. From the in-loop signal a lower limit for the residual power fluctuations was obtained while the out-of-loop signal gave an upper limit as discussed in Appendix B.

Large area p-i-n photodiodes (Donati, 2000, Section 5.2.5) with transimpedance amplifiers without bias voltage were used as photodetectors. Information on the photodiodes are shown in Table 4.1. In the experiments, always the same type of photodiode was used for in-loop and out-of-loop detector. The Indium Gallium Arsenide (InGaAs) and

Material	Model	Manufacturer	Remark
InGaAs	G8605-15	Hamamatsu	5 mm diam., int. NTC, TEC
Ge	J16TE2-8A6-R05M-SC	Judson	5 mm diam., int. NTC, TEC
Si	IPL 10050	IPL	41.3 mm ² , ext. NTC, TEC

Table 4.1.: Photodiode summary for power stabilization.

the Germanium (Ge) photodiodes included a TEC and an NTC resistor² that were used for temperature stabilization. The Silicon (Si) photodiodes were mounted on external heat sinks that included an NTC resistor as temperature sensor. Again, a TEC was used in a control loop to stabilize the temperature of the photodiode heat sink.

Temperature stabilization unity gain frequencies of 0.1 Hz for the Ge and Si photodetectors and 0.2 Hz for the InGaAs photodetectors were achieved. As loop filters, Proportional Integrator Differentiator (PID) laser crystal temperature controllers (manufactured by Innolight) were used. The Ge and InGaAs photodiodes only contained one

²negative temperature coefficient resistor

temperature sensor, so that an upper limit for their temperature stability could not be given. The external heat sink of the Silicon photodiode was equipped with a second temperature sensor and residual temperature fluctuations below $2 \text{ mK}/\sqrt{\text{Hz}}$ for frequencies between 0.1 mHz and 1 Hz have been measured.

When the laser was power stabilized, the in-loop error signal, the out-of-loop error signal, the actuator signal, and the temperature of the ambient air were measured. From the time-series, linear spectral densities were computed as described in Appendix A. The in-loop error signal specifies the residual differences between reference power and laser power. It can, in principle, be made arbitrarily small if the loop gain is sufficiently high. It is thus a lower limit of the power stability, since, e.g., drifts in the reference or sensor are not measured. The out-of-loop signal, on the other hand, is an upper limit for the laser power fluctuations, since it is derived independently from the in-loop signal and hence also included reference drifts or noise in the error signal generation process (see e.g. Appendix B).

The results that will be presented in Section 4.3 have been obtained using a common voltage reference for in-loop and out-of-loop photodiodes. Hence, an independent characterization of the reference voltage fluctuations is required to ensure a faithful measurement of the relative laser power stability.

4.2. Reference characterization

Since the relative laser power fluctuations cannot be reduced below the relative fluctuations of the employed voltage references, they are characterized in this section.

Two noise contributions add to reference signal fluctuations: internal noise of the voltage references and temperature induced drifts. An upper limit for the internal noise of the voltage reference has been measured with the setup shown schematically in Figure 4.2. A reference producing 10 V was used in combination with a low-pass filter (2-pole with 0.3 Hz cut-off and quality factor of 0.5) to decrease the noise at high frequencies. The signals of two identical filtered voltage references were subtracted, amplified, and recorded. The LPSD algorithm has again been used to calculate linear spectral densities. They are shown in Fig. 4.3. Two versions of the voltage reference AD587 have been investigated. For the trace labelled AD587JN, the difference voltage of two AD587JN references was sampled and for the other trace, the difference voltage of two AD587KN voltage references was evaluated. The “KN” devices are slightly more expensive, selected chips, while “JN” represents the cheapest standard grade. Selected premium devices called “LN” do also exist, but were not available for the experiments. As can be seen in Fig. 4.3, both versions JN and KN show basically the same voltage fluctuations. The level of relative signal fluctuations is below $6 \cdot 10^{-6}/\sqrt{\text{Hz}}$ for frequencies between $8 \cdot 10^{-5}$ Hz and 1 Hz. One should note that the relative signal fluctuations shown in Fig. 4.3 represent the quadratic sum of the voltage fluctuations of both references. When using independent voltage references for in-loop and out-of-loop signals, the noise added to the out-of-loop signal will be below $6 \cdot 10^{-6}/\sqrt{\text{Hz}}$. The measured internal voltage reference noise was below the measured power fluctuations of the LISA laser demonstrator.

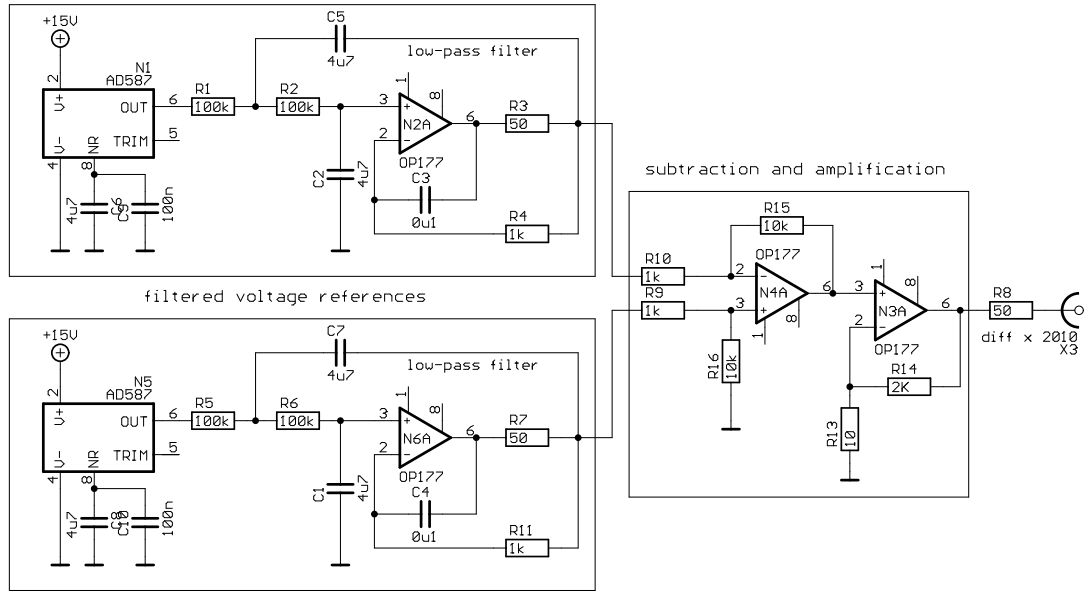


Figure 4.2.: Circuit to measure the internal noise of a voltage reference.

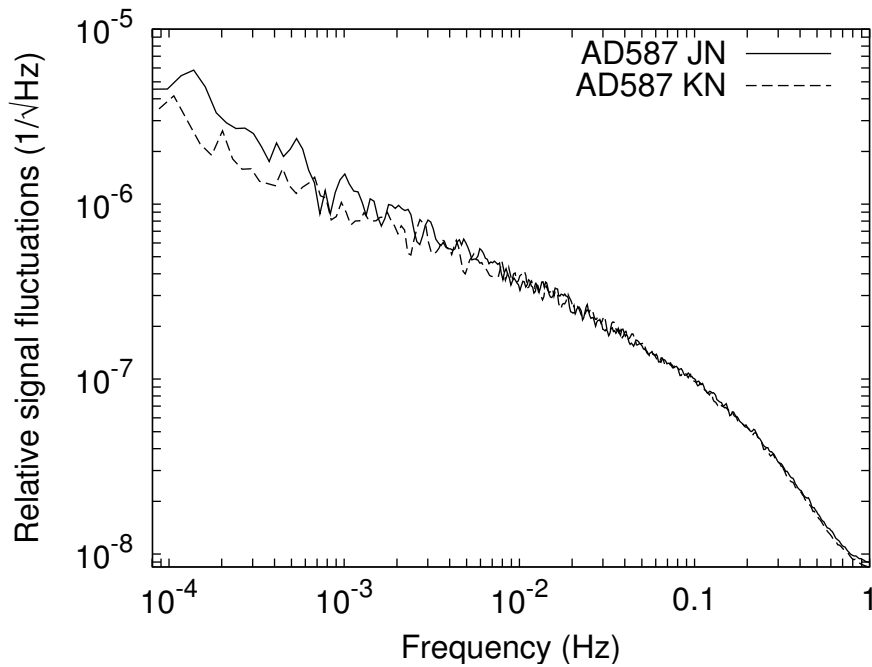


Figure 4.3.: Voltage reference internal noise measured with the setup shown in Fig. 4.2 for AD587JN and AD587KN.

AD587	Temperature coefficient (from datasheet)
JN	20 ppm/K
KN	10 ppm/K

Table 4.2.: Temperature coefficients for voltage reference AD587.

The other noise contribution to the reference voltage is given by thermally induced signal fluctuations. The relevant temperature dependencies are shown in Table 4.2. AD587JN references show a temperature coefficient of up to 20 ppm/K while the KN type only shows temperature coefficients up to 10 ppm/K.

Figure 4.4 shows the measured temperature fluctuations of the ambient air in the laboratory (dashed trace) and the air at the voltage reference (solid trace) enclosed in a housing. The traces have been obtained by recording time series of the respective temperatures and calculating spectral densities from them using LPSD. The bottom

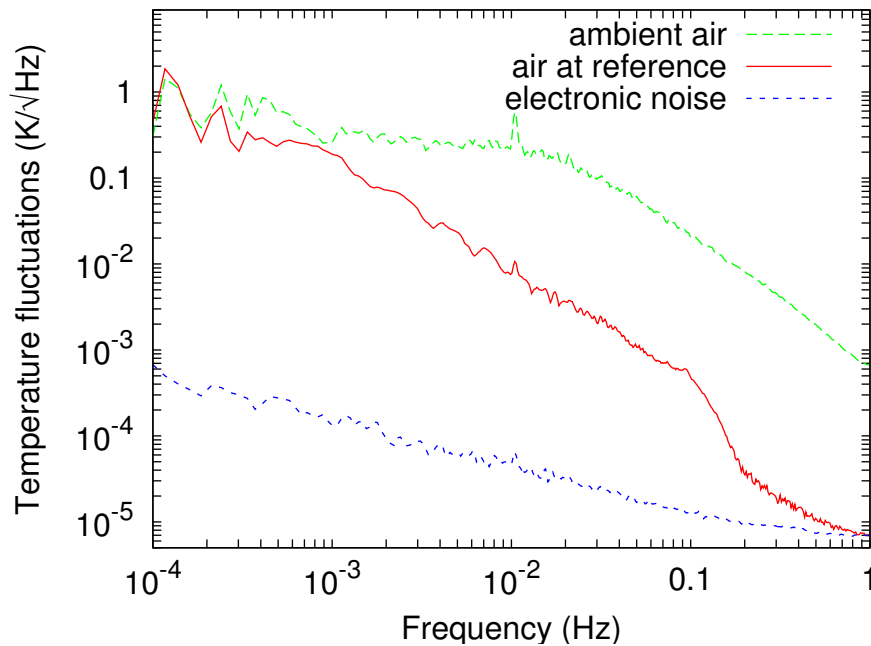


Figure 4.4.: Temperature fluctuations of ambient air, at voltage reference in housing and temperature sensor readout noise.

trace in Fig 4.4 represents the electronic noise of the temperature readout electronics. It has been measured by attaching a 10 k Ω precision resistor instead of a 10 k Ω NTC resistor to the readout electronics and measuring the resulting output voltage spectral density. With a 10 k Ω resistor, the temperature dependency of the signal produced by the readout electronics is dramatically reduced and the signal shows the noise stemming from the readout electronics. At 0.1 mHz, the temperature fluctuations measured inside and outside the housing were identical. For higher frequencies, the housing reduced

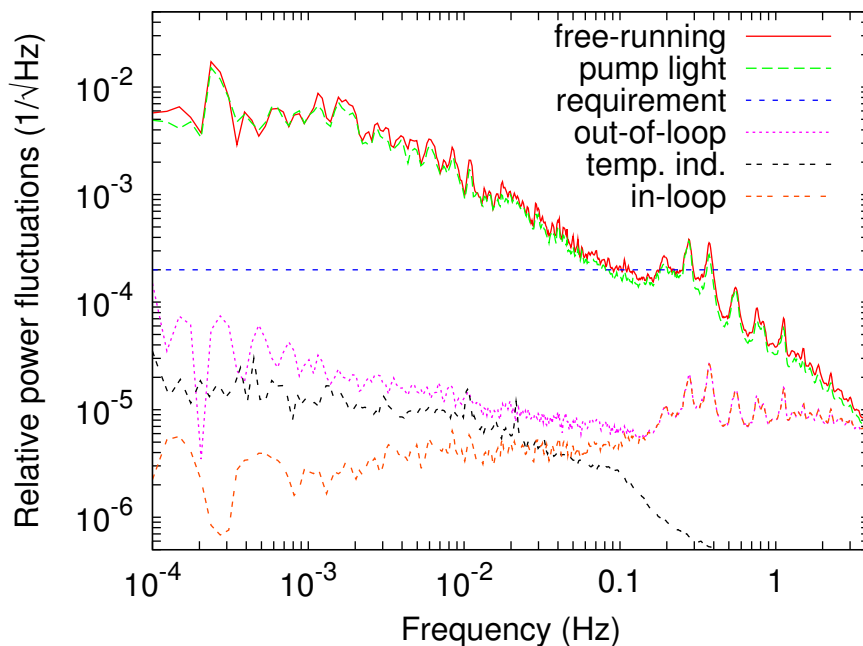


Figure 4.5.: Relative power fluctuations of LISA laser demonstrator; free-running, stabilized (out-of-loop and in-loop), pump power fluctuations, and LISA requirement of $2 \cdot 10^{-4}/\sqrt{\text{Hz}}$.

the temperature fluctuations of the ambient air. At 10 mHz, they were reduced by a factor of 25 and at 0.1 Hz a reduction of a factor of 40 can be read from the graph. Using the highest measured temperature fluctuation of $2 \text{ K}/\sqrt{\text{Hz}}$ as upper limit for the fluctuations and a temperature coefficient of 10 ppm/K for the KN type reference, one obtains temperature induced relative signal fluctuations of $2 \cdot 10^{-5}/\sqrt{\text{Hz}}$ for a single reference. Two voltage references subjected to independent temperature fluctuations will then show $2\sqrt{2} \cdot 10^{-5}/\sqrt{\text{Hz}}$ signal fluctuations, which is significantly below the LISA requirement of $2 \cdot 10^{-4}/\sqrt{\text{Hz}}$. In addition, an active temperature stabilization for the voltage references can be implemented, but was not necessary in the experiments described here.

4.3. Results

Figure 4.5 shows the relative power fluctuations of the LISA laser demonstrator that were obtained using a power stabilization employing Si photodiodes. The photodiodes were temperature-stabilized and the setup was surrounded by a cover that reduced temperature fluctuations at the experiment. The top trace shows the free-running relative laser power fluctuations that have been obtained from the actuator signal. For frequencies below 2 mHz, it showed a flat noise floor at approximately $6 \cdot 10^{-3}/\sqrt{\text{Hz}}$ and a $1/f$ -decrease towards higher frequencies. The bottom curve (labelled “in-loop”)

shows the relative power fluctuations measured at the error point of the control loop. For Fourier frequencies below 4 Hz, the in-loop error signal lies below the free-running relative power fluctuations, which confirms the unity gain frequency of 4 Hz.

The laser was pumped by a fiber-coupled diode laser module (shown in Fig. 3.4) that contained two groups of laser diodes, each group with a monitor photodiode. The relative power fluctuations of the pump light have been measured using these monitor photodiodes and plotted as trace labelled “pump light” in Fig. 4.5.

The relative power fluctuations of pump light and laser light were identical, showing that the relative laser power fluctuations were induced by pump power fluctuations as has also been reported (Harb et al., 1994). The peaks visible between 0.2 Hz and 2 Hz can also be found in the pump light. The characteristics of the pump light were transferred to the laser light and are also visible in the in-loop error signal, since this signal shows the free-running power fluctuations suppressed by the loop gain. The pump light showed varying characteristics from measurement to measurement as has also been observed for the pump diode used in Section 3.3. Due to these varying characteristics, the free-running laser power fluctuations also showed different behavior from measurement to measurement. At 1 mHz, free-running relative power fluctuations ranging from $1 \cdot 10^{-3}/\sqrt{\text{Hz}}$ to $5 \cdot 10^{-3}/\sqrt{\text{Hz}}$ have been measured.

The loop gain of the control loop showed a slope of $1/f$ with f denoting Fourier frequency and a unity gain frequency of 4 Hz. The trace labelled “out-of-loop” showed the relative power fluctuations calculated from an independently obtained error signal. For frequencies above 0.1 Hz, in-loop and out-of-loop error signal showed the same noise level, for lower frequencies the out-of-loop signal showed an increase of power fluctuations. The increased noise level was caused by residual temperature fluctuations at the photodiode and the dependency of photodiode efficiency on temperature. The corresponding measurements are described below and in Section 4.4.3. For the frequency range from 0.1 mHz to 4 Hz the out-of-loop measurement showed relative power fluctuations below $2 \cdot 10^{-4}/\sqrt{\text{Hz}}$.

Figure 4.6 shows the performance of the power stabilization for different operating conditions. The top trace shows the free-running power fluctuations of the LISA laser demonstrator, while the lowest trace shows the power fluctuations with active stabilization, measured at the error point (in-loop). The free-running power fluctuations show approximately a $1/f$ -slope with relative power fluctuations of $2 \cdot 10^{-5}/\sqrt{\text{Hz}}$ at 1 Hz. Such a $1/f$ -slope (flicker-noise) is often observed at low frequencies. The in-loop noise shows an approximately white noise level of $3 \cdot 10^{-6}/\sqrt{\text{Hz}}$. Due to the unity gain frequency of 4 Hz and the fact that the free-running power fluctuations were obtained from the actuator signal, the trace “free-running” drops below the traces showing the stabilized results. Strictly speaking, the trace showing the free-running power fluctuations is only valid for frequencies below the unity-gain frequency of 4 Hz. The free-running power noise and the in-loop power noise showed comparable results when the remaining traces were measured.

The trace below the free-running power fluctuations shows the residual power fluctuations of the stabilized laser measured out-of-loop when the photodetectors were not temperature-stabilized. A suppression of laser power fluctuations of up to one order of

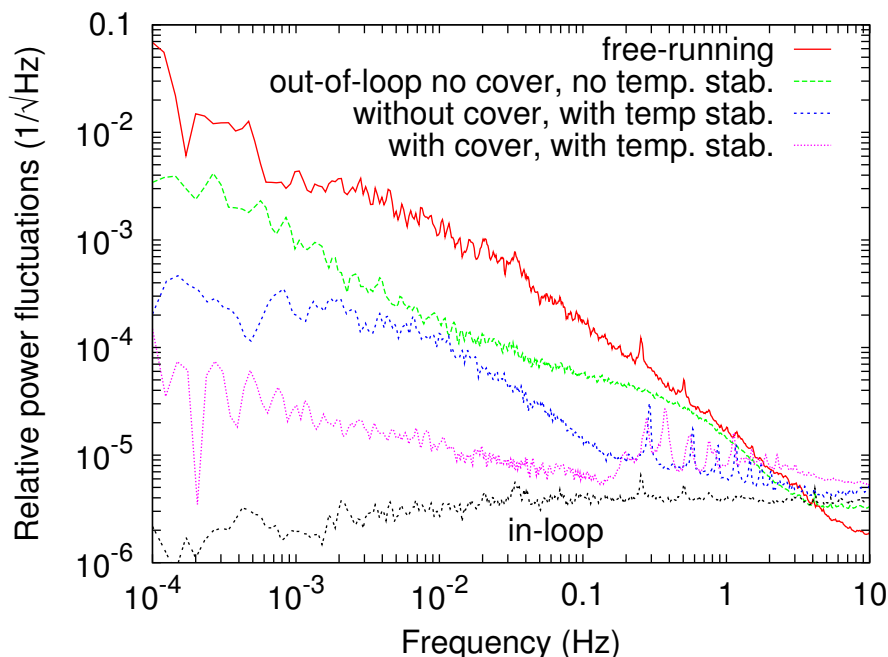


Figure 4.6.: Relative power fluctuations achieved under different operating conditions.

magnitude is visible. With temperature stabilization of the photodiodes, the curve labelled “without cover, with temp. stab.” results as out-of-loop measurement of the laser power fluctuations with a maximum suppression of two orders of magnitude. The spikes between 0.3 Hz and 3 Hz were caused by the pump module. The trace labelled “with cover, with temp. stab.” was obtained by surrounding the experiment with a cover, thus reducing convection. A suppression of laser power fluctuations of up to three orders of magnitude has been measured.

One effect of air convection are temperature fluctuations. A reduction in convection (by shielding the experiment) reduced the air temperature variations as can be seen in Figure 4.7. The top trace shows the measured temperature fluctuations at the power stabilization setup without shielding against temperature fluctuations. From 0.1 mHz to 10 mHz the temperature fluctuations showed an approximately flat noise level of $0.6 \text{ K}/\sqrt{\text{Hz}}$. With shielding against convection, the noise level was reduced by approximately one order of magnitude. For frequencies above 10 mHz both traces show a roll-off that is likely to be caused by the low-pass frequency response of the temperature sensor, and the fact that the ambient air temperature variations themselves show a roll-off towards higher frequencies.

The sensor of the photodetector temperature control loop measured the temperature of the copper heat sink below the Si photodiode, and the control loop kept this temperature constant to better than $2 \text{ mK}/\sqrt{\text{Hz}}$ as shown by the lowest trace in Fig. 4.7. The efficiency of the Si photodiode however, is given by the temperature of its pin junction, which in turn is affected by the temperature of the copper heat sink and the temperature of the air above the photodiode. Hence, ambient air temperature fluctuations still do

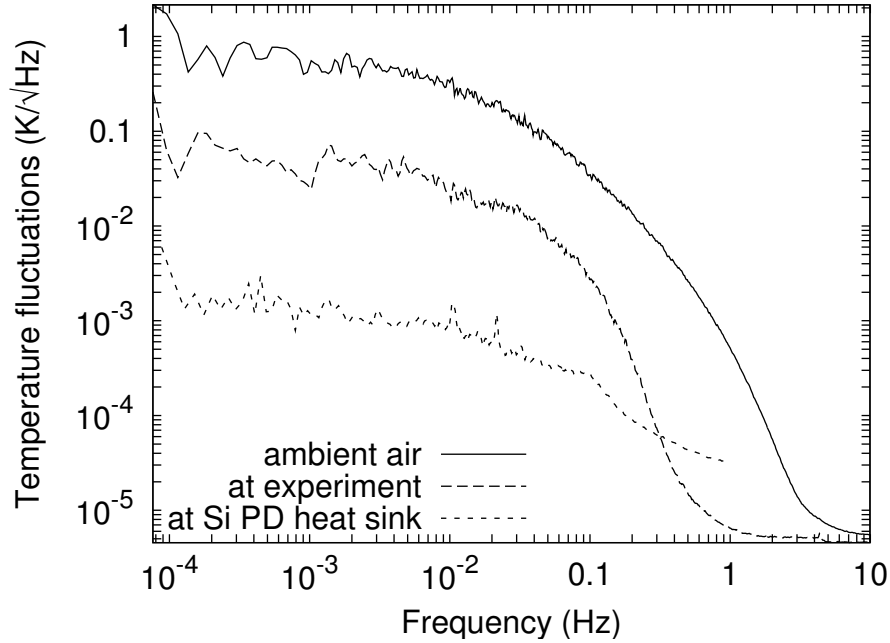


Figure 4.7.: Measured temperature fluctuations at the power stabilization setup with and without cover.

affect the temperature of the active area. The temperature stabilization reduces the coupling coefficient as can be seen by comparing the traces with and without temperature stabilization.

Power stability measurements have been performed using different kinds of photodetectors. Here, the other parameters were kept constant. The photodetectors were temperature-stabilized and the setup enclosed by a cover to reduce air convection. Figure 4.8 shows the relative power fluctuations of the free-running LISA laser demonstrator and out-of-loop signals measured using Ge, InGaAs, and Si photodiodes. Si and Ge photodiodes showed similar performance, and, contrary to expectations, InGaAs photodiodes showed reduced performance (up to one order of magnitude higher power fluctuations). In Section 4.4 a number of possible noise sources will be investigated in order to identify the limiting noise sources in the case of InGaAs photodiodes.

4.4. Noise sources

A number of noise sources can affect the performance of a power stabilization control loop. Currently, only little information has been available on the limiting noise sources for power stabilization control loops working in the frequency range from 0.1 mHz to 1 Hz.

Detailed noise investigations have been performed with two goals:

1. List and characterize possible noise sources

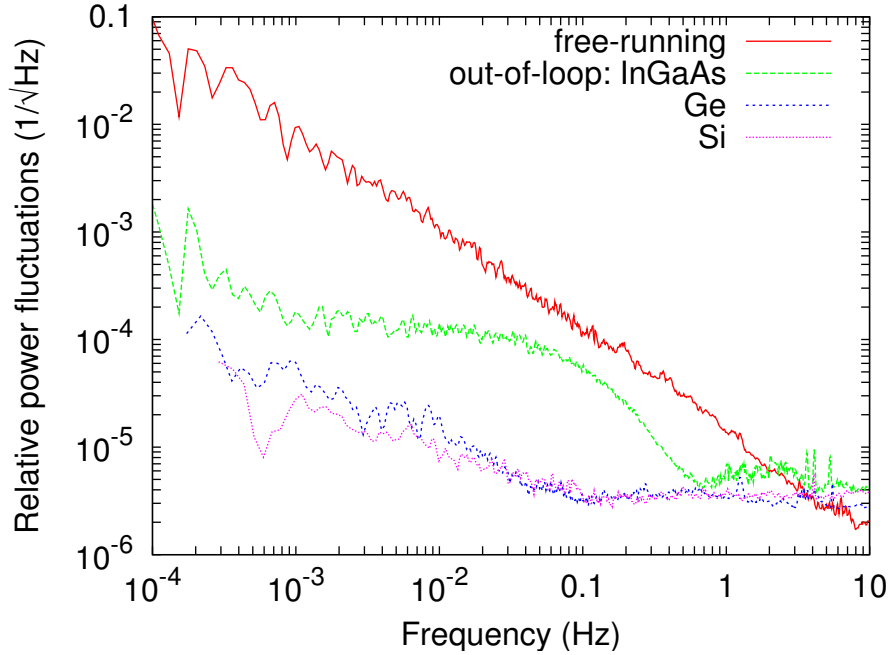


Figure 4.8.: Relative power fluctuations achieved with different photodiodes.

2. Determine limiting noise sources when InGaAs photodiodes were used

Important noise sources have been identified and characterized in order to show the different limitations in further improved power stabilization setups. Practically of most concern were the temperature dependencies of photodiode efficiency (Section 4.4.3) and the temperature dependency of beam splitting ratio (Section 4.4.5) of the beam sampling devices used to sample a small fraction of the beam.

Other noise sources that were investigated include the inevitable shot noise (Section 4.4.1), photodiode dark current (Section 4.4.2), and position dependent photodiode efficiencies (Section 4.4.4).

As shown in Fig. 4.8, the power stabilization using InGaAs photodiodes showed a reduced performance compared with Ge and Si photodiodes. This result was not expected, since according to the photodiode manufacturer, InGaAs photodiodes should show a temperature dependency of their relative efficiency of a factor of 10 below the temperature coefficient for Si photodiodes and the effects of temperature fluctuations were considered to be the dominating effect. Hence, the second goal of the investigations described below was to identify the limiting noise sources for the case of InGaAs photodiodes.

The first two noise sources, shot noise (Section 4.4.1) and dark current (Section 4.4.2) were not of practical concern in the present application, they can be critical however in power stabilizations at higher Fourier frequencies.

In the following sections, the photodiodes shown in Tab. 4.1 have been investigated.

4.4.1. Shot noise

The linear spectral density s_{SN} of relative current fluctuations due to shot noise of an electrical current I is given by (see e.g. (Yariv, 1991, p. 366))

$$s_{\text{SN}} = \sqrt{\frac{2e}{I}} \quad (4.1)$$

where $e = 1.6022 \cdot 10^{-19}$ As is the electron charge. In the experiments, at least 0.5 mA photocurrent have been used, which corresponds to a shot noise limit of $2.5 \cdot 10^{-8}/\sqrt{\text{Hz}}$. This means that the measured relative power fluctuations of above $5 \cdot 10^{-7}/\sqrt{\text{Hz}}$ were not shot-noise limited.

4.4.2. Dark current

The dark current of the Si and InGaAs photodiodes has been measured by sampling the photodetector signal with an analog to digital converter and calculating spectral densities from the time series using LPSD. Due to the measurement time of 100 minutes for the InGaAs photodiodes, spectral densities could be obtained down to 1 mHz.

Figure 4.9 shows the measured dark current fluctuations for the Si and the InGaAs photodiodes. The Si photodiodes showed a mean dark current of 5.7 nA (Si1)

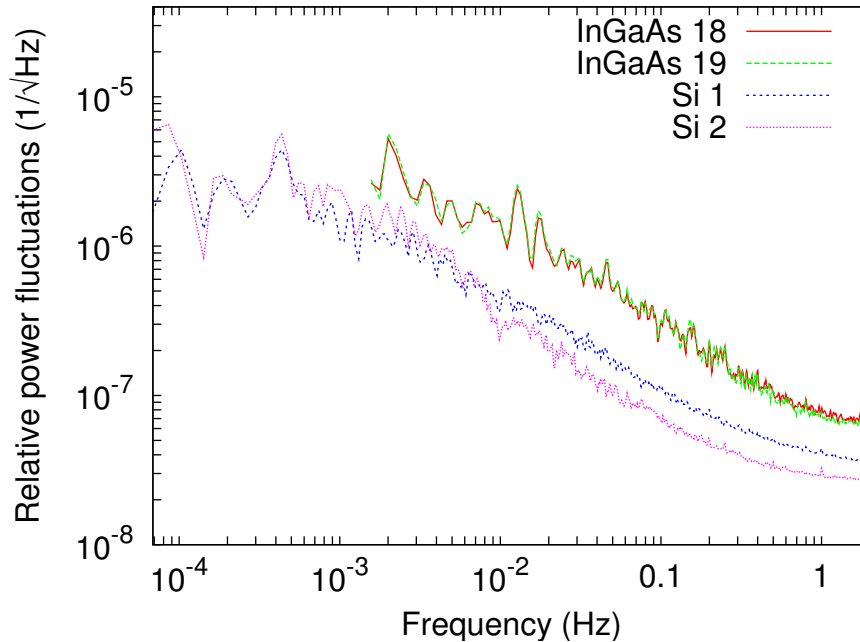


Figure 4.9.: Dark noise of Si and InGaAs photodetectors scaled as relative power fluctuations. More information on the photodiodes can be found in Table 4.1.

and 6.7 nA (Si2) without bias voltage, the InGaAs photodiodes showed dark currents of 43 nA (InGaAs18) and 180 nA (InGaAs19) with 1 V reverse bias. All photodiodes

were temperature-stabilized during the measurements. During the power stabilization measurements presented in Section 4.3, the photodiodes were used without bias voltage. Since the dark current increases with increasing bias voltage, the InGaAs traces show an upper limit of the effect of dark current. To be comparable with the power fluctuation results, the measurements have been scaled as relative power fluctuations by relating the dark currents to the photo currents used in the power stabilization experiments reported on in Sect. 4.3. There, photocurrents of 1.9 mA for InGaAs18, 1.7 mA for InGaAs19, 0.7 mA for Si1, and 0.5 mA for Si2 were used. For all photodiodes tested, the dark noise fluctuations were significantly below the measured laser power fluctuations and dark current was no limiting noise source.

4.4.3. Temperature dependent photo detection efficiency

In order to determine the effect of temperature fluctuations on the photodiode signal in a power stabilization setup, the temperature fluctuations need to be measured and the dependency of photodiode efficiency on temperature needs to be known. In this section, results are presented from measurements of temperature dependent photodiode efficiencies. Measurements of temperature fluctuations have been used to estimate their effect on the relative efficiency changes of photodiodes.

Temperature coefficients

The dependency of photodiode efficiency from temperature has been measured for Si photodiodes by illuminating them with the fraction of a collimated beam of a laser (Mephisto 500 by Innolight), setting the photodiodes at different temperatures, and recording the corresponding photodiode signals. For the InGaAs and Ge photodiodes, different techniques had to be used, because their dependency of efficiency on temperature is smaller and the direct measurement as performed for the Si photodiodes was not sensitive enough.

The temperature dependency of InGaAs photodiodes was measured by illuminating the photodiode with a few mW of optical power generated by an NPRO and measuring the transfer function from photodiode temperature to output signal using a spectrum analyzer (SRT785 by Agilent). The same results were obtained by modulating the photodiode temperature at a single frequency and measuring the photodiode response. The Ge photodiodes have been characterized using the latter method.

Table 4.3 shows the magnitudes of the photodiode temperature coefficients and the specifications given by the photodiode manufacturers.

The Si photodiodes showed a 1%/K efficiency increase with increasing temperature. The sign of the coefficient can be explained by the spectral efficiency curve of semiconductor photodiodes that shifts towards larger wavelengths as temperature increases (Donati, 2000, p. 145). Since the laser wavelength of 1064 nm is on the falling edge of the efficiency curve, a shift towards larger wavelengths for increasing temperatures increases the photodiode efficiency.

Photodiode	Specification (%/K)	Measurement (%/K)
Si	0.35	1
InGaAs	0.1	0.2
Ge	0.2	0.2

Table 4.3.: Magnitudes of relative photodiode efficiency temperature coefficients.

The measured coefficient was larger than the specified value, because the Si photodiodes were used at a wavelength near the edge of the efficiency curve where the efficiency varies strongest with temperature. Other manufacturers specify wavelength dependent temperature coefficients, e. g. Hamamatsu specifies a temperature coefficient of 0.8%/K at 1064 nm for a Si PIN diode series³.

The two InGaAs photodiodes showed temperature efficiency coefficients with opposite signs, which is in agreement with the specifications given by Hamamatsu⁴, the temperature coefficient of the same Ge photodiode showed different signs when measured at different wavelengths. These results indicate that a second mechanism must be present that influences the photodiode efficiency. A possible candidate is an optical etalon. It might be formed by the glass window or the semiconductor material itself. Due to the high refractive index of the semiconductor materials (Si: 3.5, Ge: 4.4 at 1100 nm) (Donati, 2000, p. 116) the Fresnel reflection coefficients are high (18% at 1100 nm). Even with a single-layer anti-reflection coating centered at 650 nm, reflection coefficients of 10% remain at 1100 nm (Donati, 2000, p. 117). More detailed investigations have however not been performed. The largest coefficient measured for both InGaAs and Ge photodiodes was 0.2%/K relative efficiency change.

Noise projections

The effect of temperature variations at the InGaAs photodiodes is shown in Fig. 4.10. Temperature fluctuations shown in Fig. 4.7 have been multiplied by the temperature coefficient for InGaAs photodiodes shown in Table 4.3. The top trace shows relative power fluctuations caused by ambient air temperature fluctuations measured at the power stabilization setup. The trace has been labelled upper limit, since temperature induced efficiency changes cannot exceed the temperature fluctuations of the ambient air for the low level of optical power that was used. The trace below is the power stabilization out-of-loop measurement also shown in Fig. 4.8. The bottom trace has been obtained from the in-loop temperature fluctuations of the InGaAs photodetector. Since the InGaAs photodetector only contained one temperature sensor, an out-of-loop temperature measurement was not possible. Instead, the out-of-loop temperature fluctuations of the Si photodetector have been used to obtain the remaining trace.

The InGaAs photodiodes contained a built-in TEC within their housing. Hence, the

³http://www.hamamatsu.de/assets/pdf/parts_S/S1223_series.pdf

⁴The datasheet of the G8605 states a temperature coefficient of $\pm 0.1\%/K$ at 1064 nm wavelength.

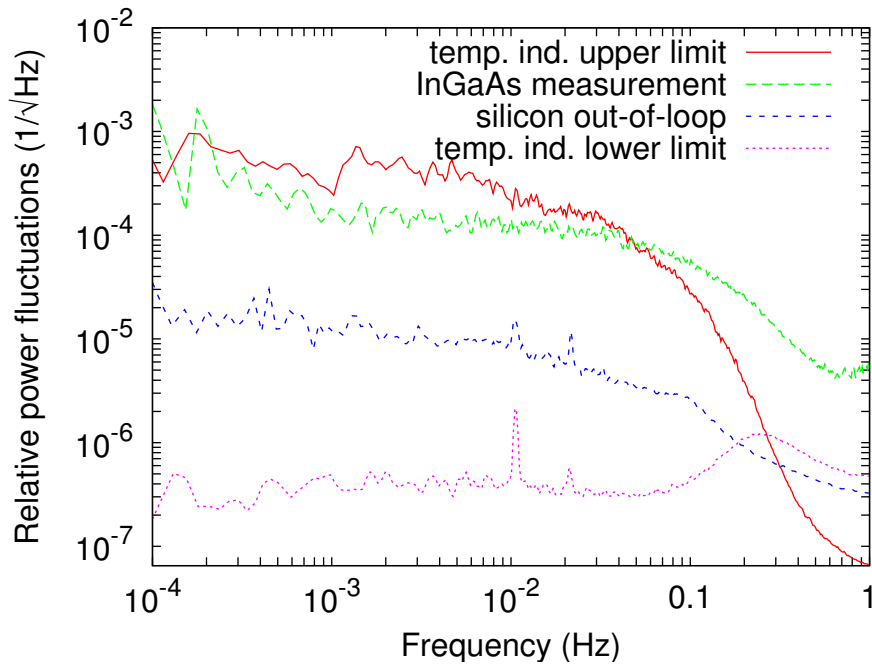


Figure 4.10.: Projection of InGaAs photodiode temperature noise to photodetector output signal fluctuations.

coupling of chip temperature to TEC temperature should be stronger than the coupling of ambient air temperature fluctuations to chip temperature fluctuations. Relative signal changes due to temperature fluctuations of the photodiode chip should be closer to one of the two lower traces than to the top trace. The fact that the power stabilities measured with the InGaAs photodiodes are closer to the upper limit of temperature-induced power fluctuations, indicates that these power stabilities were not temperature-limited. Based on the measured temperature coefficients for the photodiodes, InGaAs and Ge diodes should show a superior performance compared to Si diodes.

4.4.4. Position dependent photo detection efficiency

In this section, the effect of beam jitter on photodetection will be discussed. First, photodetectors with spatially uniform efficiency distributions will be considered and the effect of the finite aperture on the photodiode signal analyzed.

In the second part of this section, real photodiodes are considered. The spatial efficiency distributions of six photodiodes have been measured and the effect of beam jitter on the photodetector signal has been analyzed numerically.

Beam clipping

Due to their finite size, photodetectors form an aperture in the detection of light. Often, a photodiode radius significantly larger than the beam radius is chosen. Then, the aperture

effect is small and, in many applications, negligible. In the present application, however, apertures that leave a fraction of as little as 10^{-4} of the optical power undetected, can be detrimental to the performance of the photodiode. If beam jitter is present, the fraction of light power that is converted to current changes due to the aperture effect of the photodiode. This effect is estimated and requirements are given for beam radius w , photodiode radius R , and allowed beam jitter $d \ll R$, so that relative power fluctuations below x result.

The ratio p of power outside the aperture formed by the photodiode to the total power is given by

$$p = \exp\left(-2\frac{R^2}{w^2}\right) \quad (4.2)$$

where R is the radius of the photodiode and w the beam radius. When beam jitter is present, the photodiode signal can change by up to p . If relative fluctuations x of at most p in the detection signal can be tolerated, then from $x > p$ one obtains

$$w < R \cdot \sqrt{\frac{-2}{\ln(x)}} \quad (4.3)$$

For $R = 2.5$ mm and $x < 10^{-5}$ one obtains a requirement for the beam radius $w < 1$ mm for beam jitter small compared to the photodiode radius.

Spatial photodiode inhomogeneity

Preliminary measurements⁵ have shown beam displacements below 100 μm . If their effect on photodiode signals has to be estimated, the spatial resolution of photodiode inhomogeneities must be significantly smaller than the measured displacements.

Up to date, photodiode spatial efficiency measurements with a spatial resolution below 100 μm have not been performed. Table 4.4.4 gives an overview of the measurements reported on previously and the one performed in the present work. Spatial inhom-

Photodiodes	Probe beam diameter (mm)	Wavelength (nm)	Reference
Ge, InGaAs	0.5	1047	Stock et al. (1991)
Hamamatsu S1337	0.5	647	Lei and Fischer (1993)
Ge from Table 4.1	> 2.0	1100	Larason and Bruce (1998)
see Table 4.1	< 0.02	1059	this work

Table 4.4.: Comparison of spatial photodiode inhomogeneity measurements.

ogeneities of a Ge photodiode and an InGaAs photodiode at 1047 nm wavelength have been investigated (Stock et al., 1991). The probe beam diameter measured 0.5 mm and

⁵Preliminary beam jitter measurements have been performed employing non-temperature-stabilized Si quadrant photodiodes that will not be shown in this work. Instead, such measurements will be repeated using temperature-stabilized quadrant photodiodes.

variations in the percent range over the inner 3 mm of a 5 mm diameter Ge photodiode were found. It was found that the spatial uniformity of photodiodes depends on wavelength (Larason and Bruce, 1998), significantly when approaching the bandgap. Judson J16TE2-8A6-R05M-SC photodiodes showed efficiency variations up to 2% at 1100 nm, measured with a 2.5 mm \times 2.0 mm beam. Hamamatsu S1337 (pn, IR enhanced) photodiodes showed variations in efficiency of 0.1% over the inner 7 mm at 647 nm wavelength, measured with 0.5 mm probe beam diameter (Lei and Fischer, 1993).

It has been reported that integrating spheres smooth the spatial response with the cost of reducing the absolute responsivity by a factor of about 1/300 (Stock et al., 1991). Trap detectors offer increased spatial uniformity (at the 10^{-4} level) (Fox, 1991; White and Bittar, 1993).

Photodiode spatial efficiency measurements

The photodiode under investigation was mounted on two orthogonal translation stages that were used to raster the photodiode active area. The laser diode was mounted on a third translation stage for precise alignment of the laser diode focal plane.

A single-mode double heterostructure laser diode (RLT1060-10MG by Roithner Lasertechnik) was used with a collimating lens (C110, $f=6.3$ mm, $NA=0.4$ by Thorlabs). The laser diode was temperature-stabilized and operated at a wavelength of 1058.28 nm. The laser diode was operated at 4 mW of output power using a constant current driver. The beam was elliptical with beam radii in both axes of not more than 10 μ m. The photodiode surface was scanned line by line with a resolution of 10 μ m in both axes. A scan of 10 \times 10 mm² required 7 hours.

Figure 4.11 shows results of spatial photodiode efficiency measurements. The photodiode efficiencies have been color-coded as function of beam position. The efficiency is normalized to the highest signal measured on the photodiode and only the fraction of the photodiode is shown where the efficiency is at least 90%. The two spots on Ge1 as well as the many spots on Ge2 were identified as dirt and mainly non-removable defects in or on the glass above the photodiode chip. The spot on Ge2 at the upper left edge was identified as a defect on the photodiode surface. Overall variations of the efficiency of up to 4% within the inner 4 mm of the active area have been measured (for photodiode diameters of 5 mm).

Most of the spots seen on InGaAs18 and InGaAs19 are dirt or mainly non-removable defects within the glass of the photodiode (dirt is very unlikely, since the photodiodes were carefully cleaned directly before being placed in the clean test housing, but cannot be excluded, since no clean room was available). On InGaAs18, one defect on the photodiode surface was found. The inner 4 mm showed efficiency variations of 3%.

Si2 has not been aligned fully parallel with respect to the axes in the figure. In comparison to the Ge photodiodes, the Si efficiency distributions seem more noisy. This might be caused by the lower absorption in the Si photodiodes and their lower efficiency that leads to a lower signal-to-noise ratio. The spot on the upper right area of Si2 in Fig. 4.11 has been identified as a defect in the cover glass of the photodiode and the few remaining spots on Si1 and Si2 were identified as non-removable defects in or on

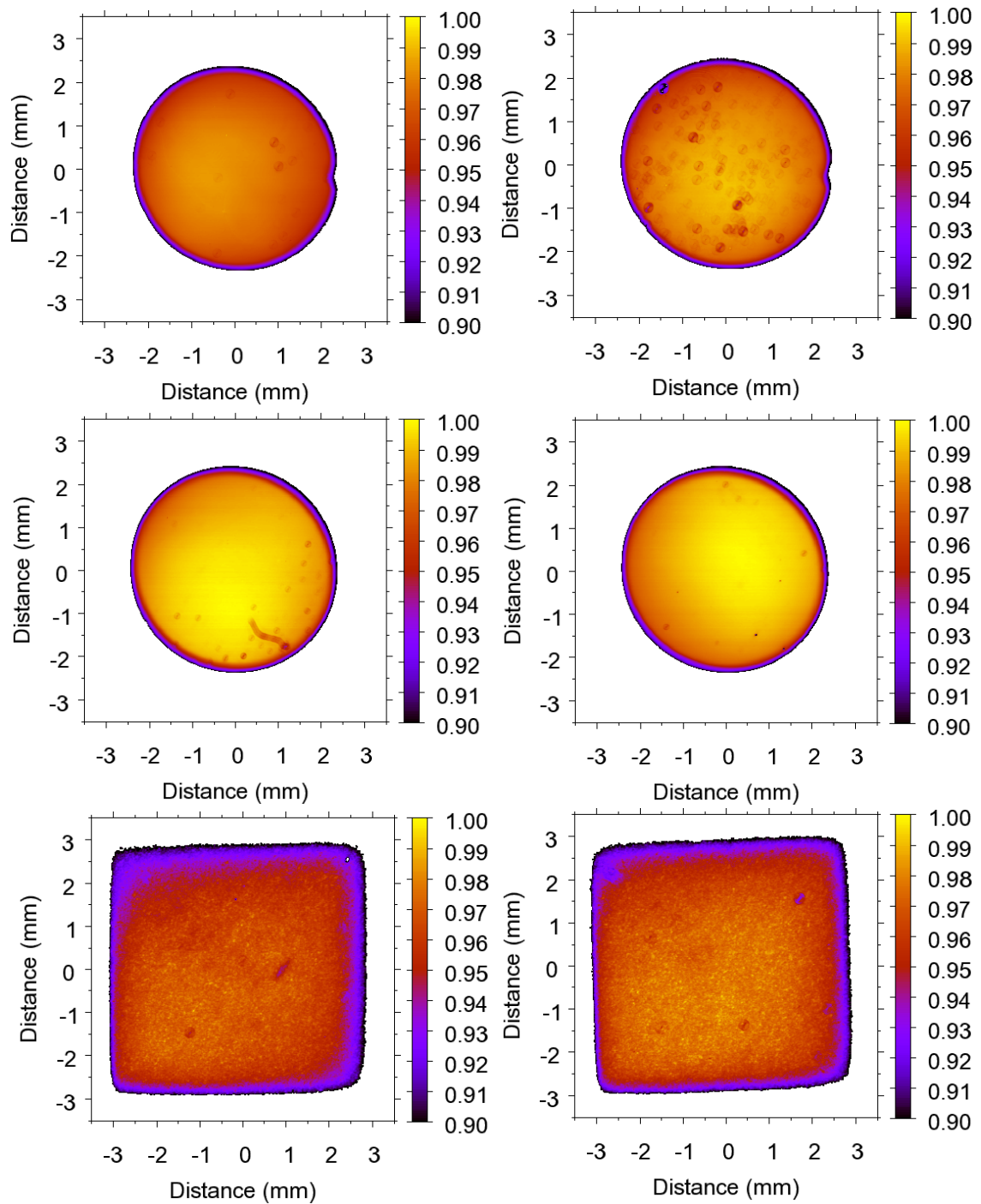


Figure 4.11.: Spatial efficiency distribution of photodiodes; from left to right; top: Ge1 and Ge2, middle: InGaAs18 and InGaAs19, bottom: Si1 and Si2.

the glass or dirt. Variations of the efficiency of up to 4% within the inner 4 mm were measured.

As an example, Figure 4.12 shows a horizontal scan through the center of Ge1. The

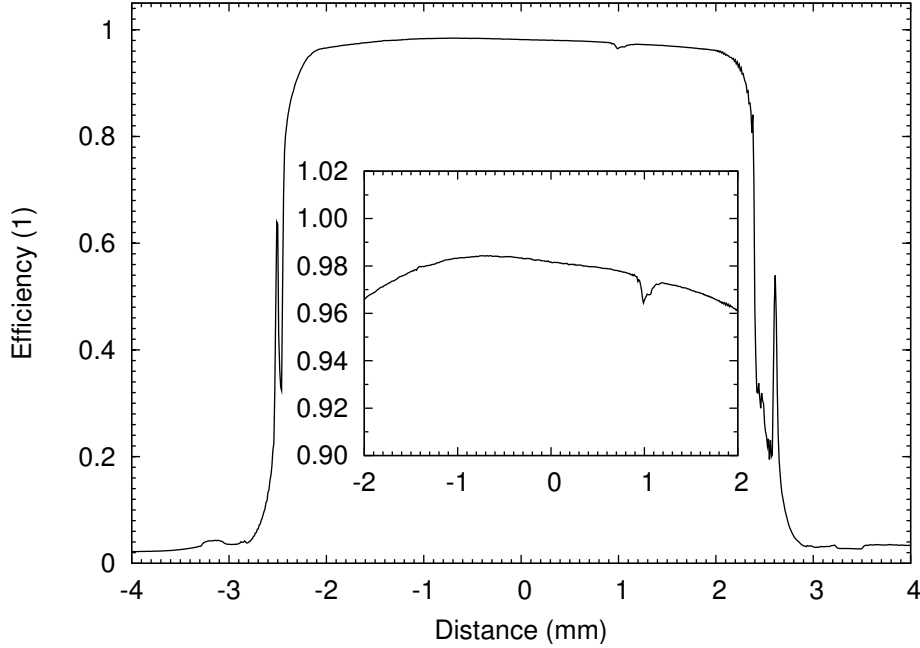


Figure 4.12.: Horizontal scan of Ge1 photodiode efficiency through center.

sharp decrease in efficiency towards the outer sides of the photodiode was caused by the ring electrode surrounding the active area. The subsequent “efficiency spikes” stem from photoactive material outside the ring electrode or from the vertical edge of the active material below the ring electrode. As can be seen from the inset, the efficiency varies by up to 3% within the inner 4 mm of the photodiode (for photodiode diameters of 5 mm).

Convolution calculations

In the following, the measured photodiode efficiency data have been used to predict the influence of beam jitter on the photodiode signal. A Gaussian beam with intensity distribution

$$I(x, y) = \frac{2P}{\pi w^2} \exp\left(-\frac{2}{w^2} ((x - x_0)^2 + (y - y_0)^2)\right) \quad (4.4)$$

where w is the beam radius (intensity drop to $1/e^2$), P the total power in the beam, and (x_0, y_0) its center has been folded with the measured photodiode efficiency data $\mu(x, y)$

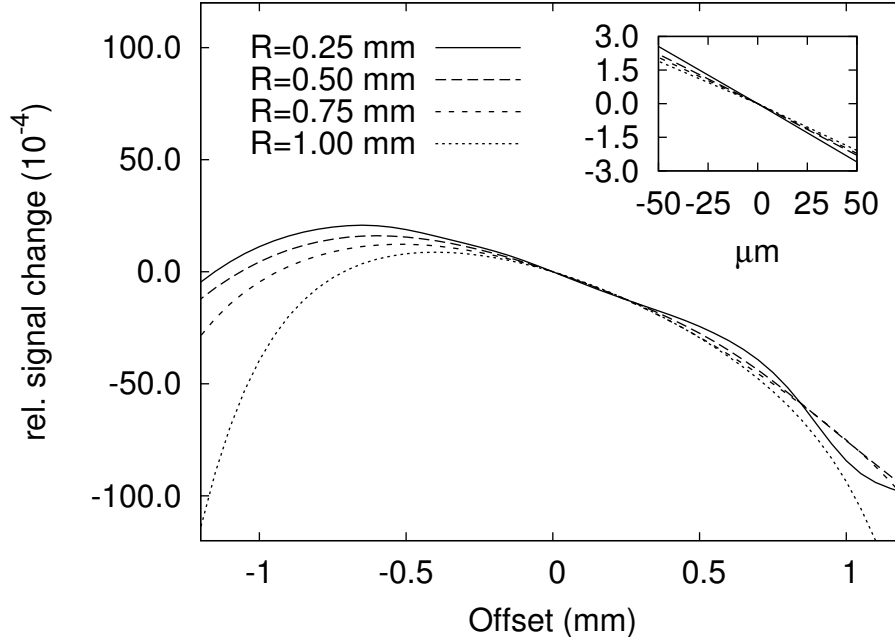


Figure 4.13.: Relative signal change of photodiode Ge1 when Gaussian beam is translated horizontally around the photodiode center. The photodiode showed its maximum efficiency not at the center (compare with Fig. 4.11).

according to

$$\begin{aligned}
 S(x, y) &= \sum_{i=i_0-D/2}^{i_0+D/2} \sum_{j=j_0-D/2}^{j_0+D/2} \bar{I}(i, j) \mu(i, j) \\
 x &= a \cdot i - 5 \text{ mm} \\
 y &= a \cdot j - 5 \text{ mm}
 \end{aligned} \tag{4.5}$$

where $a = 10 \mu\text{m}$ is the distance between neighboring data points in the efficiency measurement. D is the width and height of the data array used for convolution and $\bar{I}(x, y)$ the mean intensity of the Gaussian beam within the area covered by one data point ($10 \mu\text{m} \times 10 \mu\text{m}$) at position (x, y) . The mean intensity has been calculated using a version of the popular trapezoid formula (Press et al., 1992, Sect. 4.2) where the intensities of four points on the edges of the square area have been averaged to obtain the mean intensity within the area. An area of 500×500 data points was used to calculate the photodiode signals. For this area, only a fraction of 6×10^{-5} of the total power was outside the region used for the calculation, which is sufficient for the present application.

Convolutions of Gaussian beams and photodiode efficiency data have been calculated along a horizontal line through the center of photodiode Ge1 and the relative differences to the convolution result in the photodiode center are shown in Figure 4.13. The main graph shows the relative signal changes of the photodiodes for the inner 2.4 mm, whereas the insets show the relative signal change for the inner $100 \mu\text{m}$ as blow-up. All convo-

lutions have been performed for four different beam radii, namely 0.25 mm, 0.5 mm, 0.75 mm, and 1 mm.

The figure shows a stronger signal decrease towards the outer edges of the photodiode for larger beams than for smaller beams, which can be attributed to the aperture formed by the photodiode and the photodiode efficiency decrease towards the outer edges. Photodiode Ge1 showed signal variations of up to 1% for beam movements over the inner 2.4 mm for all beam radii investigated.

4.4.5. Temperature dependent beam splitting ratio

Not only the detection efficiency of photodiodes depends on temperature, also the ratio under which a sample of an optical beam is separated from the main beam can depend on temperature. In this section, the temperature dependencies of different beam sampling devices are analyzed and the contribution of temperature fluctuations to power fluctuations are given.

Temperature coefficients

A 1% output coupling mirror manufactured in e-beam technology and an 0.3% output coupling mirror manufactured by ion beam sputtering (IBS) have been investigated experimentally. The temperature dependency of the reflection coefficient of glass plates has been calculated. The results are shown in Table 4.5.

device	coefficient (1/K)
1% e-beam output coupler	$3 \cdot 10^{-3}$
0.3% IBS output coupler	$< 1.6 \cdot 10^{-4}$
quartz wedge	$4.8 \cdot 10^{-5}$

Table 4.5.: Temperature coefficients for beam samplers; relative transmission change per temperature change for output couplers, relative reflectance change per temperature change for quartz wedge.

For the e-beam mirror a relative transmission coefficient of 0.3%/K has found (Steier, 2004b, p. 60). The main physical effect is given by the inclusion of water in the dielectric layers. With varying temperature, the water contents varies, thus altering the layer thickness and hence the mirror reflectivity.

The IBS mirror was characterized using a spectrometer (Lambda 19 by Perkin Elmer). Transmission spectra were recorded at 7 temperatures between 25.6 °C and 154.4 °C. To increase the measurement resolution, the transmission of the output coupling mirror was measured relative to a 1 mm NG3 filter with 12% transmission. The spectrum at 26.5 °C has been subtracted from the spectra at higher temperatures. It was found that the transmission structure moves to longer wavelength for higher temperatures. An upper limit for the temperature dependency of the transmission at a

wavelength of 1064 nm was found with $1.6 \cdot 10^{-4}/\text{K}$. This upper limit was dominated by the measurement accuracy of the spectrometer.

Not only mirrors can be used for beam sampling, also glass wedges have shown good performance (Fischer and Lei, 1993; Fischer, 2004). The reflection coefficient at a single interface between air and glass is given by the Fresnel equations. If the dependency of the refractive index of glass and air on temperature is known, the dependency of the reflection coefficient on temperature can be readily calculated. Quartz glass has a refractive index of $n = 1.45$ and a $dn/dT = 11.9 \cdot 10^{-6}/\text{K}$ at $1 \mu\text{m}$ wavelength⁶. The dependency of the refractive index of air on temperature was taken from Birch and Downs (1993). For 6° angle of incidence, a temperature coefficient of

$$\frac{\Delta R}{\Delta T}(\text{SiO}_2) \approx 4.8 \cdot 10^{-5}/\text{K} \quad (4.6)$$

has been obtained for quartz glass. This is significantly below the upper limit that could be specified for the IBS output coupler and even a factor of 60 below the temperature coefficient measured for the e-beam output coupler.

Quartz glass wedges showed the smallest temperature dependency of the beam sampling devices that were investigated. Due to this fact, they have been used as beam samplers in the power stabilization experiments described in this Chapter.

Noise projections

Figure 4.14 shows noise projections derived from temperature fluctuations at the power stabilization setup (see Fig. 4.7) and the coefficients listed in Table 4.5. A factor of $\sqrt{2}$ has also been included since two independent beam samplers add a factor of $\sqrt{2}$ to the noise of a single device. For comparison, the measured power fluctuations from Section 4.3 have been included.

For frequencies below 0.1 Hz the fluctuations induced by the e-beam output couplers would be above the measured power fluctuations. The results obtained would not be possible with the e-beam output couplers that have been characterized. If the IBS output couplers from Table 4.5 had been used, they would limit the measured power fluctuations. The noise contributions of the quartz wedges that have been used, is approximately one order of magnitude below the measured fluctuations.

⁶Source: <http://www.crystran.co.uk/siodata.htm>

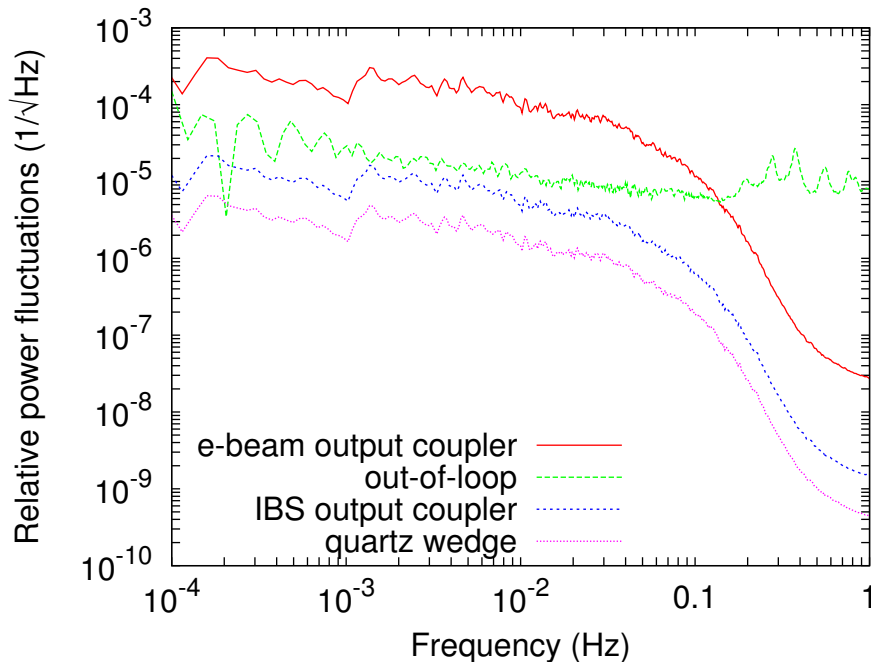


Figure 4.14.: Projection of temperature fluctuation at beam sampler to relative power fluctuations.

4.5. Conclusions

In conclusion, the output power of the NPRO-based LISA laser demonstrator has been stabilized by sampling a small fraction of the output power with a photodiode, comparing its signal with a stable voltage reference, and feeding back the amplified difference signal to the pump power. A level of relative power fluctuations below $2 \cdot 10^{-4}/\sqrt{\text{Hz}}$ for frequencies ranging from 0.1 mHz to 1 Hz could be achieved. Temperature-stabilized Si photodiodes and quartz glass wedges were used for beam detection and beam sampling, respectively. When Si photodiodes were used, the measured power stability was temperature limited for frequencies below 20 mHz and loop-gain limited for frequencies above 0.1 Hz. An important experimental condition was the reduction of air convection at the experiment. This led to reduced temperature fluctuations that in turn led to the power fluctuations shown in Fig. 4.5.

Several noise sources and limitations have been characterized and their noise contributions have been plotted in Fig. 4.15. For comparison, the power fluctuations of the LISA laser demonstrator have been added to the graph. Currently, the loop gain was limited by the loop filter design (a single integrator) and the unity-gain frequency of 4 Hz. In previous measurements (not shown) a unity-gain frequency of 40 kHz has been demonstrated, which corresponds to an increase in loop gain of four orders of magnitude already. A further increase is possible by different loop filter designs. Loop gain is not considered to be problematic.

The temperature induced noise contributions of photodiode, quartz wedge and volt-

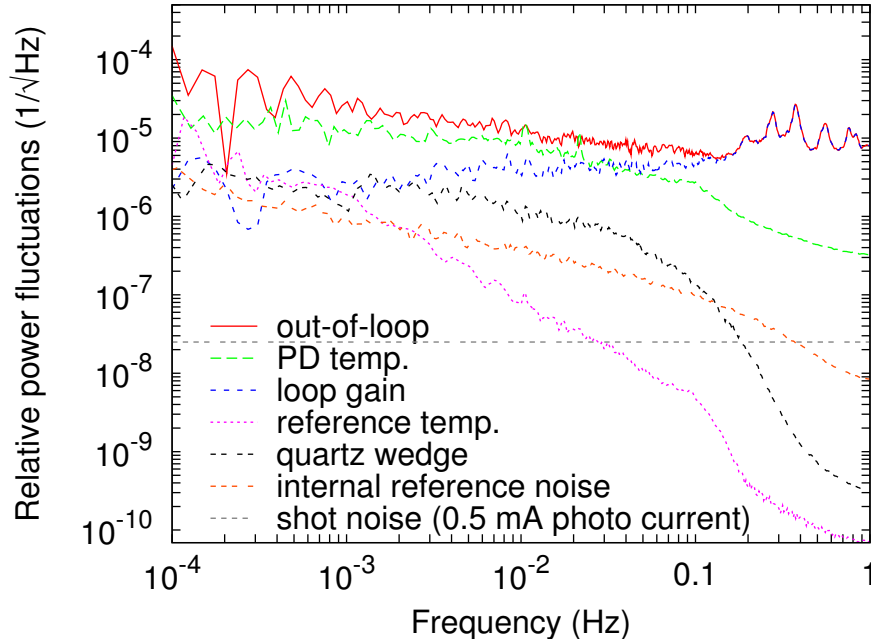


Figure 4.15.: Summary of limiting noise sources in power stabilization.

age reference can also be reduced. The photodiode temperature stability should improve when the setup was placed in a vacuum chamber. The temperature stabilities of quartz wedge and voltage reference can be improved by implementing active temperature stabilizations. The photodetector relative shot noise can be reduced by increasing the photocurrent according to Eq. (4.1).

Currently, I am not aware of a method to reduce the internal noise of the AD587 voltage reference. Measurements are performed (Steier, 2004a) in order to investigate the influence of temperature fluctuations on the internal noise of AD587 voltage references and the suitability of other references for LISA.

The effect of beam jitter and spatially inhomogeneous photodiode efficiencies on laser power stability will be investigated using temperature-stabilized quadrant photodiodes. So far, only non-temperature-stabilized Si quadrant photodiodes were available.

In summary, the laser demonstrator for LISA based on a high-power NPRO was stabilized in output power. Temperature dependent photodiode efficiencies and temperature dependent beam sampling ratios for different photodiodes (Si, Ge, InGaAs) and different beam samplers (e-beam output coupler, IBS output coupler, quartz glass wedge) were characterized. Quartz glass wedges and Si or Ge photodiodes are well-suited for use with LISA. The output power fluctuations of the laser demonstrator could be reduced to a level below the LISA specification.

5. Frequency stabilization

The free-running frequency fluctuations of the laser candidates for LISA were significantly higher than the upper limit of allowed frequency fluctuations, as has been discussed in Chapter 3. A reduction of free-running frequency fluctuations of at least six orders of magnitude is necessary to meet the requirement of $30 \text{ Hz}/\sqrt{\text{Hz}}$ for frequencies from 1 mHz to 1 Hz (ESA-SCI 11, 2000, p. 76).

Laser frequency stabilization to a Fabry Perot cavity has been reported (Ueda and Uehara, 1992; Uehara and Ueda, 1993). Two lasers were locked to the same cavity and spectral densities of frequency fluctuations were given for frequencies above 10 Hz. Dirscherl et al. (1992) have reported frequency stabilization of a dye laser to a Fabry-Perot cavity. An independent cavity was used for analysis of laser frequency fluctuations and $10 \text{ Hz}/\sqrt{\text{Hz}}$ at 10 Hz residual frequency fluctuations were measured. Young et al. (1999) have frequency stabilized a dye laser at 563 nm to two independent cavities and given Allan deviations for averaging times up to 32 s.

In previous experiments, the low-frequency noise of Nd:YAG lasers locked to optical resonators at room temperature was dominated by thermal fluctuations of the reference cavities (Sampas et al., 1993a,b; McNamara et al., 2000).

Beat experiments between lasers that were frequency-locked to Fabry Perot cavities made of Ultra-Low Expansion glass (ULE by Corning) or Zerodur (Schott) with thermal expansion coefficients of typically better than $5 \times 10^{-8}/\text{K}$ have been reported (Sampas et al., 1993a; McNamara et al., 2000; Uehara and Ueda, 1994; Ruoso et al., 1997). Thermal decoupling of these resonators from the laboratory atmosphere by placing them in vacuum housings has yielded beat frequency drifts of 22 MHz over 48 hours (Uehara and Ueda, 1994) and 40 MHz over 60 hours (Ruoso et al., 1997). A reduction of beat frequency fluctuations has been achieved by Sampas et al. (1993b) by actively temperature stabilizing the vacuum housing to about 0.1 K. The beat-frequency changes obtained during a five day period were less than 1 MHz.

Although excellent long-term frequency stabilities have been achieved with cryogenic resonators (Seel et al., 1997; Storz et al., 1998; Braxmaier et al., 2002), their use is not possible on board the LISA satellites, since it is technically difficult to include cryostats that maintain temperatures of 4 K on board of satellites orbiting the sun. In addition, their additional mass would dramatically increase the cost of the mission.

The frequency drifts that have been reported, however, do not describe the frequency fluctuations in the detail required for LISA. Here, spectral densities of frequency fluctuations for frequencies between 1 mHz and 1 Hz are necessary.

5.1. Experiments

Figure 5.1 shows a schematic of the optical setup. Beams from two laser systems were

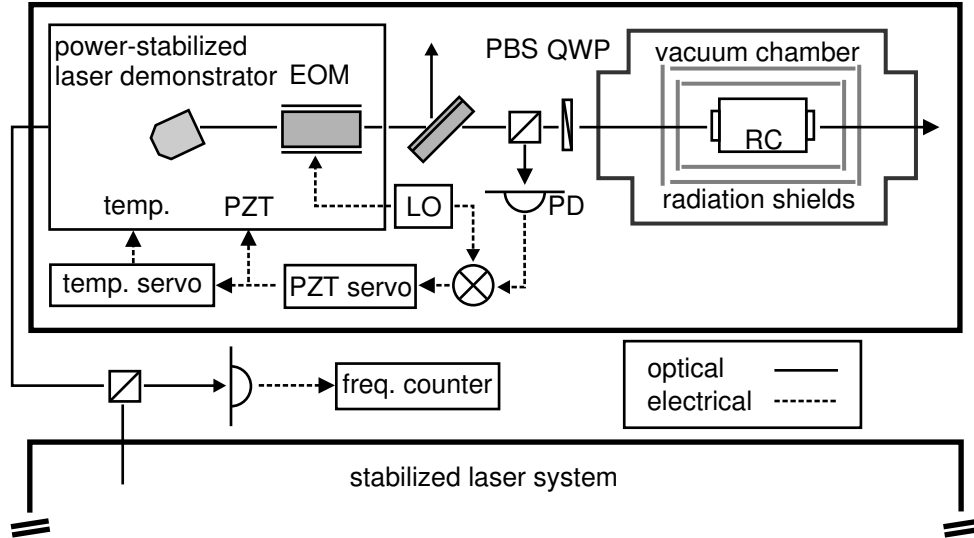


Figure 5.1.: Combined power- and frequency stabilization setup of the LISA laser demonstrator and a reference system; polarizing beam splitter PBS, quarter-wave plate QWP, reference cavity RC, photodiode PD, local oscillator LO.

brought to interference on a fast photodiode and the photodiode signal was fed into a frequency counter (SRS 620 Option 01 by Stanford Research Systems). One laser system consisted of the LISA laser demonstrator and the other of a reference NPRO (labelled M2). The laser demonstrator was operated at an output power of 800 mW, the reference laser M2 was operated at 100 mW of output power¹. Both lasers were locked to the transmission peak of their own thermally shielded reference cavity. From the LISA laser demonstrator, 400 μ W of optical power were transmitted through the reference cavity and 178 μ W through the second cavity from the reference NPRO. For the laser demonstrator, a coupling efficiency of 70% to a cavity TEM₀₀ mode was achieved, for the second laser (M2), 40% of the light were coupled into its reference cavity.

The cause for the reduced coupling efficiency to cavity 2 could not be identified yet. Mode-mismatching between laser mode and cavity mode was excluded by varying the positions of the mode-matching lenses (not shown in Fig. 5.1). TEM₀₀ operation of the laser was verified by coupling the radiation of this laser into cavity 1 with significantly higher efficiency.

The standard Pound-Drever-Hall reflection technique for frequency stabilization was used (Drever et al., 1983; Black, 2001). A resonant EOM (model 4003 by New Focus)

¹The laser demonstrator had to be operated at a slightly reduced output power, since the pump module had lost output power. Instead of 4.4 W of pump power, only 3.9 W of pump power were available

Measurement approach	Cavity 1	Cavity 2
error signal fit	10060	3000
transfer function	8100	2200
linewidth	10060	2100

Table 5.1.: Finesse measurements at optical cavities.

generated phase modulation sidebands 10 MHz away from the optical carrier frequency (12 MHz for the second system) with a modulation index of 0.5 (0.3 for the second system). The light reflected from the cavity was monitored by a fast Si-photodiode with a tuned preamplifier (Heinzel, 1999, Appendix B). The signal from the photodiode was mixed with the local oscillator that drove the EOM to generate the error signal. A loop filter with three damped integrators (with a corner frequency of 100 Hz) acted on a PZT mounted on the laser crystal to correct for fast frequency fluctuations. A second control loop used the PZT voltage as error signal and acted on the crystal temperature via its temperature controller to compensate for long-term frequency drifts. The unity gain frequencies of the PZT control loops were measured as 22 kHz for the laser demonstrator and 12.5 kHz for the reference laser with phase margins of 52° and 30° , respectively. The phase margins were sufficiently large for stable operation of both control loops over many days without loss of frequency lock. It will be shown in Section 5.2 that the loop gain that was achieved with the loop filter design and the control loop bandwidth was more than sufficient to achieve the required frequency stability.

A laser power stabilization as described in Chapter 4 was incorporated into the setup. The second laser used a power stabilization with essentially the same performance.

The reference cavities consisted of a cylindrical spacer made of ULE with a diameter of 8 cm, a length of 21 cm and a central bore of 1 cm diameter. Two small bores were drilled perpendicular to the central bore for evacuation. A plane mirror and a concave mirror with -1 m radius of curvature were optically contacted to the ends of the spacer. The cavities were manufactured by Research Electro-Optics (USA).

The cavity linewidth and hence, for a given free-spectral range, the cavity finesse is an important parameter for the frequency stabilization error signal generation. For a fixed free-spectral range of the cavity, the error signal slope increases linearly with the finesse of the cavity. A high error signal slope allows a precise coupling of the laser frequency to a resonance frequency of the cavity.

The finesse has been measured for both cavities using three different methods that produced consistent results. Table 5.1 shows the measured finesse values of both optical cavities. The results labelled “error signal fit” have been obtained by applying a sawtooth signal to the PZT of the free-running laser while the laser frequency was centered around a resonance frequency of the reference cavity. The PZT voltage ramp and the resulting frequency stabilization error signal were recorded and the analytical error signal function (Black, 2001) has been fitted to the measured error signal with the vertical scaling, the PZT efficiency, and the finesse as fit parameters. For the first cavity, a finesse of 10060 has been obtained which agrees with the manufacturer’s specification of 10000.

The corresponding measurement for cavity 2 yielded a finesse of 3000. This result was significantly lower and unexpected since both cavities were manufactured to the same specifications. The finesse of cavity 2 had been measured previously (21.02.2003) using the “transfer function”-method that is explained below and a finesse of 9400 had been obtained.

To verify the results, the finesse of both cavities was measured again using the “transfer function” method. While the laser frequency was locked to a transmission peak of the reference cavity, a sinusoidal signal was inserted into the control loop and its transfer function was measured from the PZT signal to the error signal. This transfer function includes the characteristics of the PZT and a pole (a low-pass) caused by the storage time of the cavity. The measured transfer function was fitted with a single pole and a delay. A pole frequency of 44 kHz was determined as fit parameter. It should be noted that a precise determination of the pole frequency would require data extending the frequency range up to 100 kHz, which were not available. Since the pole frequency is the half-width of the cavity linewidth, a finesse estimation of 8100 can be calculated for cavity 1. The corresponding measurement for cavity 2 resulted in 159.6 kHz linewidth and a finesse of 2200.

A third consistency check was performed by a direct linewidth measurement. The laser frequency was modulated by a sawtooth signal. With the known PZT efficiencies of 1.9 MHz/V for the laser demonstrator and 2.7 MHz/V for M2 and a sawtooth signal applied to the laser PZTs, the linewidths were estimated using the error signal. For the first cavity, a linewidth of 36 kHz which corresponds to a finesse of 10060 and for the second cavity, a linewidth of 169 kHz corresponding to a finesse of 2100 were estimated.

From March 2003 to October 2004 the finesse of cavity 2 decreased by a factor of 3 to 4. Within this time, the cavity was removed from the vacuum chamber and subjected to manual handling that was necessary due to relocation of the experimental setup. Contamination of the cavity mirrors is a likely cause for the decrease in finesse.

5.2. Results

Figure 5.2 shows the results obtained from frequency stabilization of the LISA laser demonstrator. The top trace shows the free-running frequency noise of the NPRO-based laser demonstrator. Free-running means that the pump diodes were driven by a constant current source and the temperature of the laser crystal mount was actively stabilized. The trace was obtained from the beat-note between free-running laser demonstrator and frequency-stabilized reference laser M2.

The trace “M1-M2” shows the beat-note between two identical power-stabilized and frequency-stabilized reference lasers (the first laser was labelled M1, the second M2) that was obtained in a setup where laser M1 instead of the laser demonstrator was locked to cavity 1 and M2 was locked to cavity 2 and the beat frequency between both lasers was recorded. The difference frequency between laser demonstrator and M2 has been labelled “HSL-M2”. It showed essentially the same frequency fluctuations as measured between M1 and M2. The laser demonstrator (labelled HSL for “High Stability Laser”) seemed

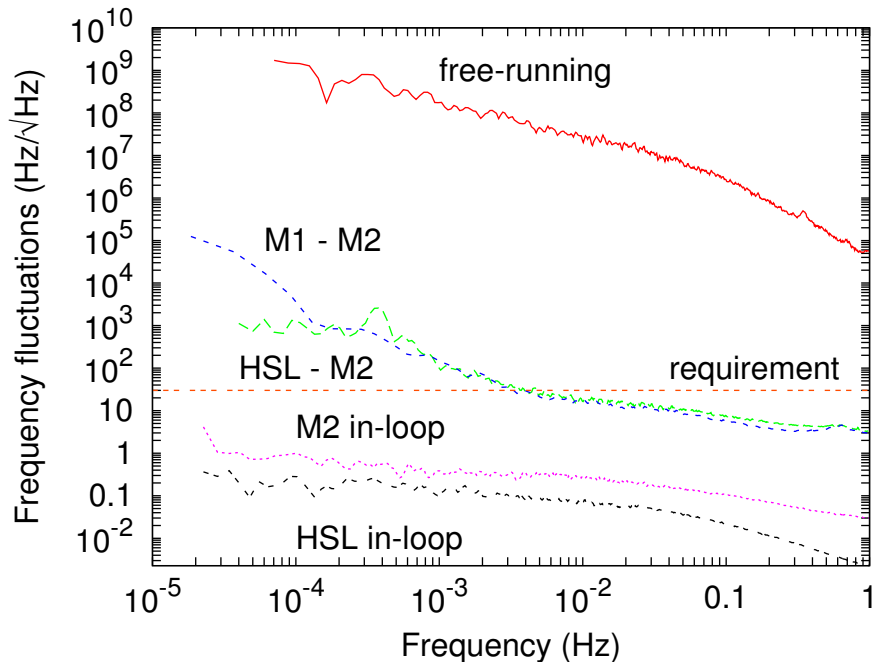


Figure 5.2.: Frequency fluctuations of the LISA laser demonstrator (labelled HSL) and reference laser (labelled M2) and frequency fluctuations of two reference lasers (M1 and M2).

to respond stronger to temperature changes than M1 and M2 since the peak at 0.4 mHz visible in the beat frequency of HSL and M2 was at the same frequency as the peak of laboratory air fluctuations caused by the air conditioning. The frequency fluctuations between M1 and M2 did not show this peak. Residual amplitude modulation of the EOM due to temperature fluctuations is a possible noise source as is discussed in Section 5.3.5. M1 and M2 used both model 4001 EOMs by New Focus while the laser demonstrator used model 4003, which includes a resonant circuit that was built externally in the case of M1 and M2.

The two lowest traces show the frequency fluctuations of M2 and laser demonstrator relative to their reference cavity, measured at the error points of the frequency stabilizations. Both in-loop signals were significantly below the frequency fluctuations obtained from the difference frequency measurement, which shows that the frequency stability was not loop-gain limited.

5.3. Noise sources

Various noise sources can affect the frequency stability of the laser by either disturbing the reference frequency or by disturbing the lock of laser frequency to reference frequency. In Sections 5.3.1 and 5.3.2, disturbances of the reference frequency are discussed and in Sections 5.3.3 to 5.3.5 disturbances of the laser frequency lock to the reference frequency

are discussed.

5.3.1. Temperature fluctuations

In order to estimate the effect of temperature fluctuations at the frequency references on the beat frequency, in a first step the temperature coefficients of both reference frequencies (determined by the length of the reference cavities) were measured. In a second step, the temperature fluctuations of the ambient air were measured and the measured temperature noise was projected to frequency noise as described below.

Temperature coefficients

In order to investigate the effect of temperature variations on the resonance frequency of the reference cavities, the temperature of one vacuum chamber containing one cavity was modulated at 0.1 mHz while both lasers were frequency-locked to the two cavities and the resulting beat-note change was measured. At a modulation frequency of 0.1 mHz, a temperature coefficient of frequency change of 94 Hz/K resulted for temperature modulation of vacuum chamber 1. In the corresponding measurement for cavity 2, a coefficient of 156 Hz/K was obtained.

Noise projections

Temperature measurements (not shown) clearly demonstrated that on long time scales (10000 seconds), the temperature fluctuations seen by both vacuum chambers were identical. From the measured temperature fluctuation time series a temperature fluctuation spectral density has been calculated. This spectral density has been multiplied by the difference of the temperature coefficients for both cavities.

Figure 5.3 shows this noise projection from temperature fluctuations to laser frequency fluctuations as trace labelled “induced by correlated temperature fluctuations”. The measured frequency fluctuations between the laser demonstrator and a reference laser (labelled “beat-note”) and the requirement on frequency stability have also been shown. For the noise projection, the temperature fluctuations of the ambient air were multiplied by the difference of both coefficients.

Figure 5.3 shows that the noise projection trace is a factor of 10 or even more below the measured frequency fluctuation trace, which shows that temperature fluctuations did not limit the frequency stability of the laser demonstrator.

5.3.2. Power fluctuations

When both lasers were locked to their reference cavity, a variation of one laser power resulted in a variation of the beat frequency. More specifically, a variation of the power transmitted through one of the reference cavities resulted in a beat frequency change. The light oscillating within the optical cavity heated the mirror coatings. Changes in the power transmitted through the cavity caused a change in temperature at the mirror

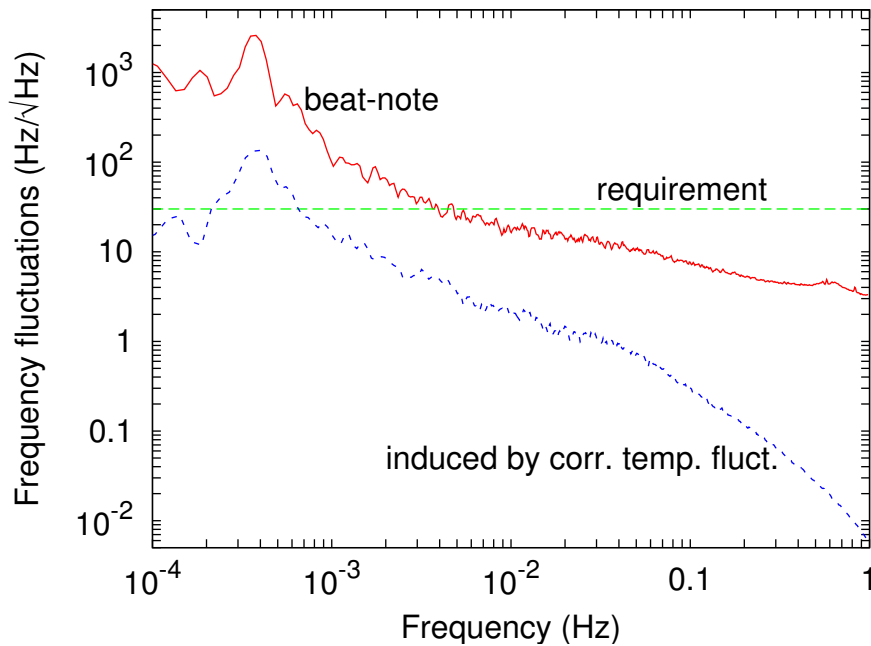


Figure 5.3.: Influence of ambient air temperature fluctuations on frequency fluctuations of frequency-stabilized laser.

coatings, thereby shifting the resonance frequency of the cavity. Since beam jitter between laser beam and cavity affects the coupling efficiency, and hence the optical power oscillating in the cavity, beam jitter can couple into the beat frequency as is being investigated by Sascha Skorupka.

Again, two steps were taken to assess the influence of laser power fluctuations on the beat frequency fluctuations between both lasers (laser demonstrator and reference laser M2). In a first step, the coefficient between beat frequency change per power change was measured and in a second step, the power fluctuations of the laser were measured and projected to frequency fluctuations.

Power coefficients

In order to determine the dependency of the beat frequency from the power transmitted through the reference cavity, the setup shown in Fig. 5.1 was used. In contrast to the measurements presented in Section 5.2 significantly more laser power was incident in the reference cavity to enhance the effect of varying laser powers in the cavity. Also, an additional half-wave plate (HWP1) was inserted between laser and PBS. Between photodetector and PBS, a second half-wave plate (HWP2) and a second PBS were inserted. HWP1 was used to change the optical power incident on the cavity. To tackle with this side effect HWP2 and the additional PBS were inserted. They allowed power variations at the photodetector independent from power variations in the cavity.

Figure 5.4 shows the beat frequency change as function of laser power that was

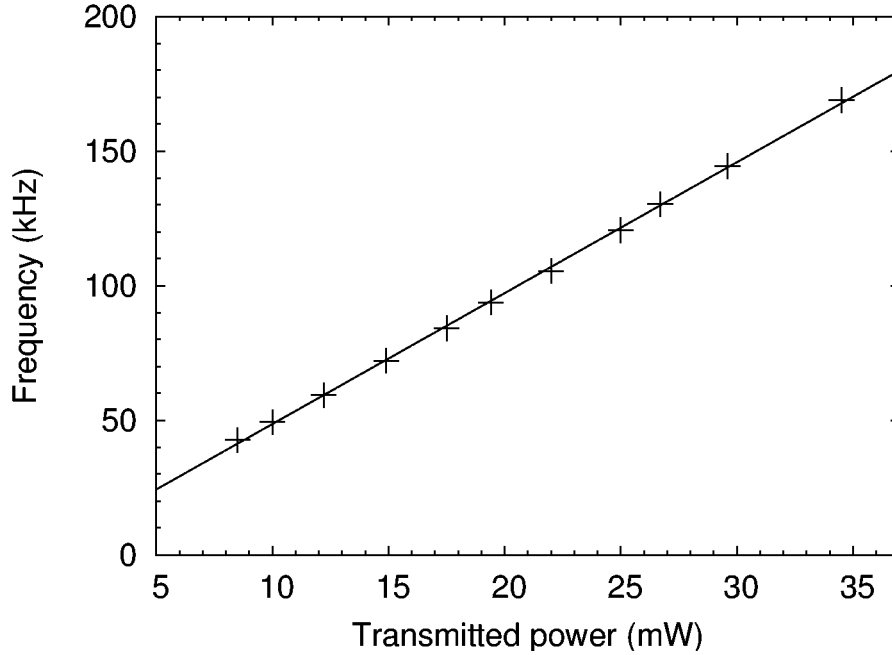


Figure 5.4.: Reference frequency shift for varying powers transmitted through reference cavity 1. The slope of frequency change per transmitted laser power measured 4.9 kHz/mW.

transmitted through cavity one when HWP1 was used to change the power incident on the cavity (and the photodiode). A slope of 4.9 kHz/mW of transmitted power was measured.

Since rotation of HWP1 simultaneously varied the power incident on the cavity and the power incident on the photodiode, a second measurement was performed to test, whether the frequency changes depended on the power on the photodiode or in the cavity. Figure 5.5 shows the time-series that was obtained. Within the first 30 min HWP1 was used to vary the power on the photodiode and in the cavity. The power transmitted through cavity 1 was reduced by approximately 13 mW for five times and increased by approximately the same amount. The actual average values (in mW) of the transmitted power are given in the graph. They have been measured using a power meter (LM2 + Fieldmaster by Coherent) placed behind the reference cavity. From the ten power changes displayed in Fig. 5.5 an average laser frequency change per change in transmitted laser power of $4.9 \text{ kHz/mW} \pm 0.1 \text{ kHz/mW}$ has been derived. This coefficient is identical to the one obtained by measuring the laser frequency for different laser powers incident on the cavity.

Between 30 min and 40 min, the power incident on the photodiode was reduced and increased by rotating HWP2 three times, while the power incident in the cavity remained constant. Although the power was reduced to the same level as when HWP1 was rotated, no change in frequency was visible. Hence it was shown that the power used for frequency stabilization changes the beat frequency. It was measured that an increase in transmitted

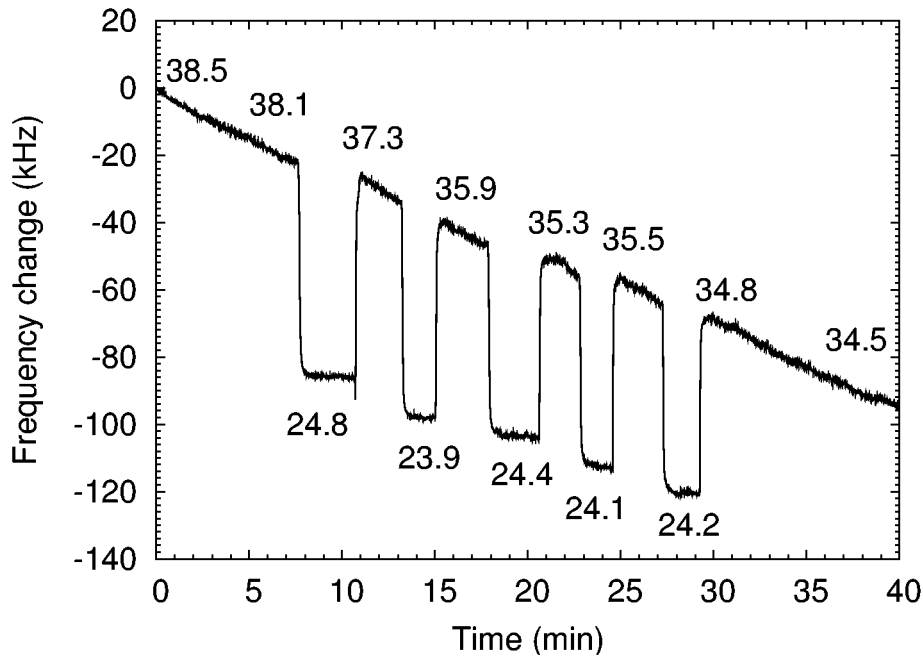


Figure 5.5.: Time-series of beat frequency between lasers locked to reference cavities. The numbers indicate the power in mW transmitted through cavity 1. A laser frequency change per transmitted laser power of $4.9 \text{ kHz/mW} \pm 0.1 \text{ kHz/mW}$ was derived.

power increased the reference frequency of the cavity. This effect has been reported by Stoehr (2004) and Young et al. (1999). Stoehr (2004) reported the same sign that was measured here.

In the following, the measured coefficient will be used to estimate the effect of laser power variations on the beat frequency.

Noise projections

In order to estimate the effect of power variations on frequency variations of the frequency-stabilized laser, the measured relative power fluctuations shown in Fig. 4.5 have been multiplied with the power that was transmitted through the cavity to obtain the absolute power variations of the laser ($400 \mu\text{W}$ have been used in Section 5.2). These values were multiplied by the coefficient of 4.9 kHz/mW and are shown in Fig. 5.6 along with the measured frequency fluctuations from Fig. 5.2. The frequency fluctuations induced by the unstabilized power fluctuations were at least a factor of three below the measured beat-note. The frequency fluctuations induced by the stabilized laser power fluctuation were more than two orders of magnitude below the measured frequency fluctuations. Hence, the measured frequency fluctuations were not limited by laser power fluctuations.

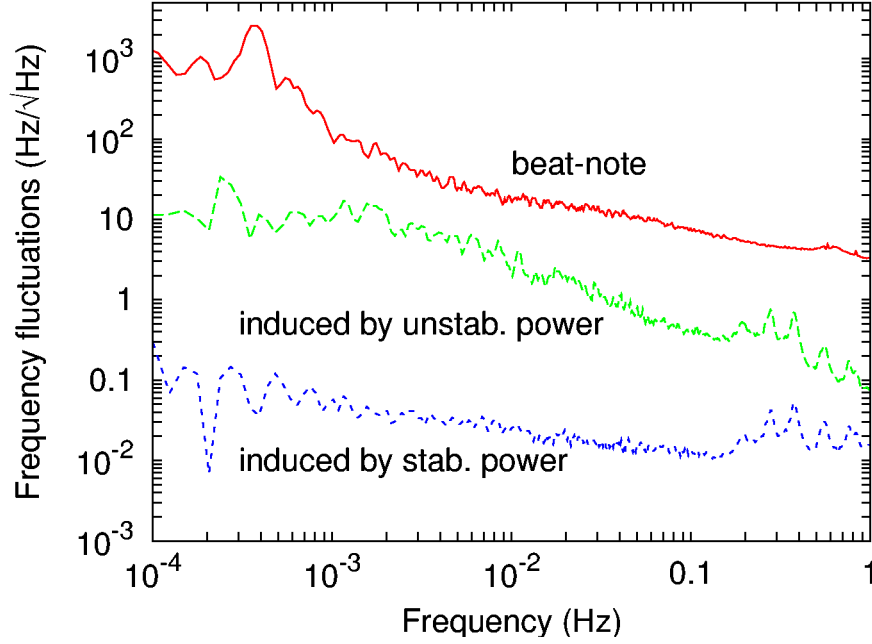


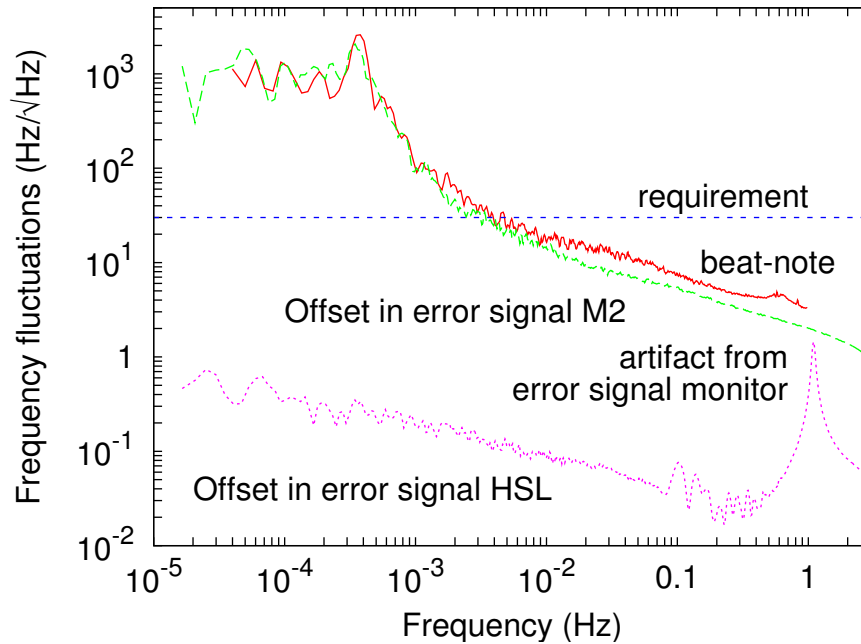
Figure 5.6.: Influence of laser power fluctuations on frequency fluctuations of frequency-stabilized laser.

5.3.3. Shot noise

Laser power fluctuations at the modulation frequency of 10 MHz for the NPRO-based laser demonstrator (12 MHz for M2) pose a limit on the frequency stability. The shot noise of the photocurrent is however inevitable. The linear spectral density of shot-noise limited frequency fluctuations is given by (Black, 2001)

$$s_f = \frac{\sqrt{hc^3}}{8} \frac{1}{FL\sqrt{\lambda P_c}} \quad (5.1)$$

where $h = 6.626 \cdot 10^{-34}$ Js is Planck's constant, $c \approx 3 \cdot 10^8$ m/s is the speed of light, F the finesse of the cavity, L the cavity length, λ the wavelength, and P_c the power within the carrier. A quantum efficiency of unity has been assumed. The wavelength of the light was 1064 nm, the cavity length measured 21 cm which resulted in a free-spectral range of 714 MHz, the finesse has been measured as 9400 for cavity 1 and 2400 for cavity 2, and about 400 μ W for the first cavity and 178 μ W in the second cavity have been used. The resulting frequency fluctuations (using 178 μ W and a finesse of 2400) reads 2.4 mHz/ $\sqrt{\text{Hz}}$, which is more than three orders of magnitude below the lowest measured frequency fluctuations of 3 Hz/ $\sqrt{\text{Hz}}$ (see trace "HSL-M2" in Fig. 5.2). This means that the measurement is not limited by shot-noise in the Pound-Drever-Hall frequency stabilization scheme.



bht

Figure 5.7.: Contributions of error signal offsets to frequency fluctuations.

5.3.4. Error signal offsets

Figure 5.7 shows the measured frequency fluctuations of the laser demonstrator (labelled HSL) and reference laser M2 and frequency fluctuations induced by varying error signal offsets. The trace labelled “beat-note” shows the measured frequency fluctuations between HSL and reference laser M2 when both lasers were frequency-locked to independent cavities.

The traces labelled “Offset in error signal” were obtained by placing a high-reflective mirror between optical cavity and QWP in Figure 5.1. Then, all light normally incident in the cavity is reflected to the photodiode and the error signal is independent from the laser frequency. It is visible that offsets in the HSL frequency error signal were considerably below the measured frequency fluctuations. The peak at 1 Hz was an artifact originating from the HSL error signal monitor. Frequency fluctuations induced by offsets in the frequency error signal of reference laser M2 showed essentially the same noise level as the measured beat frequency fluctuations of both lasers. This indicates that the beat frequency fluctuations of both lasers were limited by offsets induced in the frequency error signal of reference laser M2.

Possible origins for such offsets are

- drifts of the photodiode resonance frequency,
- drifts in the error signal offset compensation, or
- residual amplitude modulation in the EOM.

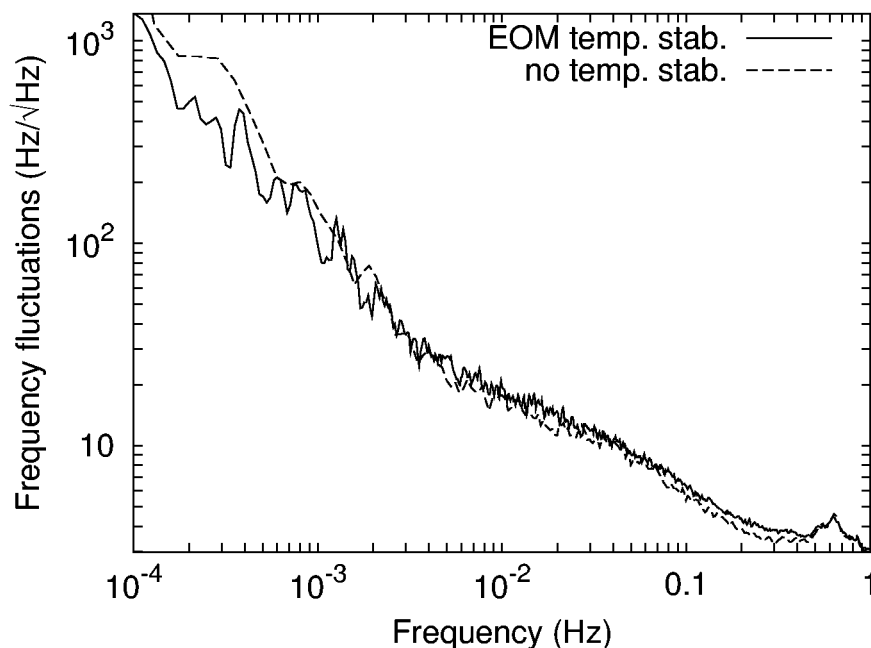


Figure 5.8.: Effect of EOM temperature drift on beat frequency.

The photodetector included a resonant preamplifier. Temperature changes might change its resonance frequency which resulted in a phase change of the photodetector response. This in turn leads to an offset in the error signal that translates to a change in frequency.

In order to remove static offsets from the error signal, a voltage was added to it. Changes of this compensating voltage would also lead to frequency changes of the laser. However, the added voltage was sufficiently stable.

EOMs are known to produce parasitic polarization modulation that translates to power modulation at polarizing elements such as polarizing beam splitters. The effect is commonly referred to as “residual amplitude modulation (RAM) that will also be utilized here. Corresponding investigations will be described in the following section.

5.3.5. Residual amplitude modulation

Preliminary experiments have shown that the amount of RAM depends on the temperature of the EOM. Wong and Hall (1985) list temperature-dependent birefringence variations of the phase modulator crystal, scattering, and etalon effects as causes for RAM. Investigations of RAM showed that a frequency dependent and a frequency independent component can be found (Whittaker et al., 1985).

Temperature stabilizations for the EOMs were built and beat measurements between the reference lasers performed with and without EOM temperature stabilization. Figure 5.8 shows the results. For Fourier frequencies above 0.6 mHz the frequency fluctuations with and without EOM temperature stabilization were identical. For lower fre-

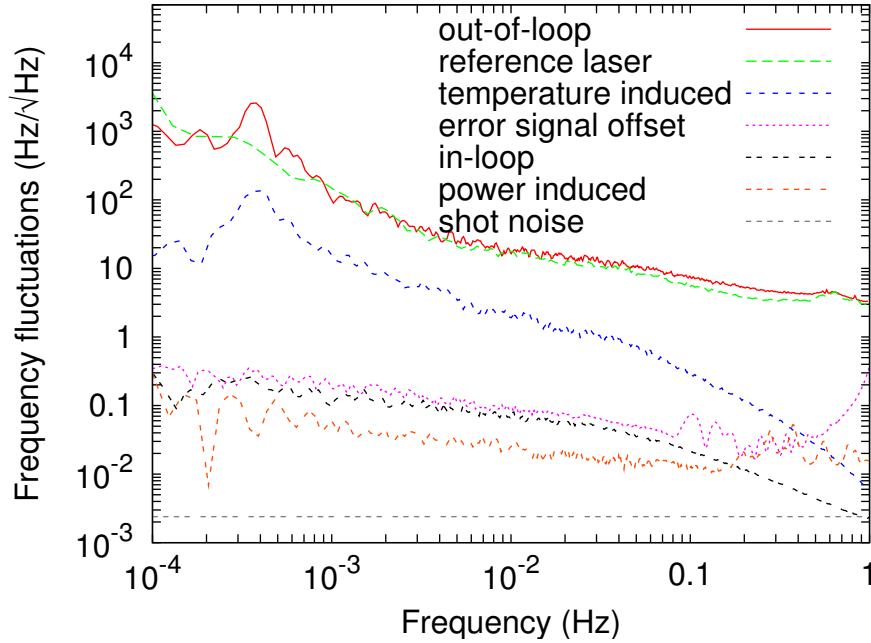


Figure 5.9.: Summary of limiting noise sources in frequency stabilization.

quencies an increase of less than a factor of two was visible in the frequency fluctuations in the case of unstabilized EOM temperature. Since 0.6 mHz is already outside the LISA specification for frequency fluctuations, the slight increase in frequency fluctuations can be ignored.

In the measurement band down to 1 mHz, EOM temperature fluctuations were not the limiting noise source for laser frequency fluctuations.

5.4. Conclusions

In conclusion, the requirements concerning the frequency stability of the LISA laser demonstrator have been fulfilled down to 3 mHz and detailed noise investigations have been performed. In the remaining frequency band from 1 mHz to 3 mHz, frequency fluctuations of up to $100 \text{ Hz}/\sqrt{\text{Hz}}$ have been found. The shot noise limit of Pound-Drever-Hall frequency stabilization was calculated for the parameters used in the experiments, the effect of temperature fluctuations at the reference cavities was measured, the effect of power fluctuations in one of the cavities was investigated, varying offsets in the error signals were found, and the effect of residual amplitude modulation was characterized.

The different noise sources have been summarized in Fig. 5.9. The top trace shows the measured frequency fluctuations of the laser demonstrator and a reference system. This measurement was limited by the stability of the reference system. In order to improve the frequency stability of the laser demonstrator, the reference systems requires improvement. In Section 5.3.4 it was shown that error signal offset drifts of the reference

system need to be reduced to improve its frequency stability. It was also shown that the optical cavity showed a significantly reduced finesse compared to the other cavity. An increase in finesse of a factor of four would result in a factor of four decrease in frequency fluctuations due to varying error signal offsets.

The next noise source was approximately one order of magnitude below the measured frequency fluctuations and was given by the temperature fluctuations at the reference cavity. One should note that the trace represents an upper limit. For frequencies above 0.1 mHz, the temperature dependency might well be significantly weaker than plotted here, because the filter function of the thermal shield surrounding the cavity has not been taken into account. The temperature stability at 0.1 mHz can be improved by actively temperature stabilizing the vacuum chambers.

The next lower limit to the frequency stability of the laser demonstrator was given by varying offsets in the error signal. Their causes need to be investigated and measures taken to reduce this noise source. Active stabilization of RAM as presented by Wong and Hall (1985) might be an effective measure to reduce its noise contribution.

The loop gain of the frequency stabilization limits the frequency stability to values of approximately $0.2 \text{ Hz}/\sqrt{\text{Hz}}$. The loop gain can be increased by adding integrators to the loop filter, thus reducing the in-loop noise contribution.

The trace labelled “power induced” represents induced frequency changes from light that was power-stabilized to the level shown in Fig. 4.5. Currently, the power of the light incident in the cavity has been stabilized. If beam jitter between cavity and laser beam is present in the LISA measurement window, then the power transmitted through the cavity should be stabilized instead of the power incident on the cavity. Another measure to decrease the power-induced frequency fluctuations is to further decrease the power used for stabilization.

In summary, the laser demonstrator for LISA based on a high-power NPRO was stabilized in frequency to a thermally shielded Fabry-Perot cavity and an upper limit for its frequency stability was determined through beat measurements with an independently stabilized laser system. The LISA requirements of $30 \text{ Hz}/\sqrt{\text{Hz}}$ have been met for frequencies above 3 mHz. For frequencies between 1 mHz and 3 mHz, residual frequency fluctuations of up to $100 \text{ Hz}/\sqrt{\text{Hz}}$ were measured. The measurement was limited by the frequency stability of the reference system.

6. Summary and outlook

The space-based interferometric gravitational wave detector LISA will be able to detect gravitational waves with frequencies ranging from 0.1 mHz to 1 Hz that are inaccessible to ground-based detectors. For this purpose, LISA requires a highly stable laser source emitting 1 W of polarized output power in single longitudinal and transverse mode. At the beginning of this work, no such laser was available, the properties of existing lasers in the LISA measurement band were unknown, and no measurement equipment was available.

First, the means of noise characterization in the LISA frequency range down to 0.1 mHz had to be developed. The spectral measurements in this work were performed by calculating spectral densities from previously digitally sampling data. An improved algorithm was developed that is especially well-suited for large amounts of data and the usage of a logarithmically scaled frequency axis, both of which were necessary in this work. The novel technique based on discrete Fourier transforms calculates spectral densities with a logarithmically uniform frequency axis and an increasing number of averages towards higher frequencies. This approach allows spectral estimation at very low frequencies that are inaccessible to commercial spectrum analyzers and it produces spectral estimates that are more accurate than those of the standard method.

Then, a diode-pumped laser demonstrator for LISA based on a stand-alone high-power NPRO was designed, implemented, and characterized. It showed 1.2 W of polarized output power from 4.4 W of pump power, which represents 20% more output power than required in single longitudinal and transversal mode. For the first time, the free-running (unstabilized) relative power and frequency fluctuations of a high-power NPRO have been characterized in the LISA measurement band. Free-running relative power fluctuations of up to $10^{-2}/\sqrt{\text{Hz}}$ have been measured for frequencies ranging from 0.1 mHz to 1 Hz. Frequency fluctuations of the free-running laser of up to $2 \cdot 10^8 \text{ Hz}/\sqrt{\text{Hz}}$ for Fourier frequencies between 1 mHz and 1 Hz have been measured. The pump current of the laser demonstrator was used as power actuator and a PZT glued onto the laser crystal and the laser crystal temperature were used as frequency actuators. In terms of output power, beam quality, and polarization, the unstabilized laser demonstrator fulfilled the LISA requirements.

So far, the baseline design selection for LISA has been followed and the second laser concept, a fiber amplifier seeded by a low-power laser, has not been considered. This concept is, however, attractive in terms of power scalability. To date, the excess power and frequency noise produced by a fiber amplifier in the LISA measurement band were unknown and suitable actuators for power and frequency have also not been

identified yet. Hence, an Ytterbium-doped fiber amplifier seeded by a low-power NPRO was investigated. Sensitive power- and frequency-noise measurements of the amplifier were performed and actuators for power and frequency stabilization have been identified and characterized. The amplifier emitted 1 W of polarized output power in a single longitudinal and transverse mode from 10 mW of seed power. For the first time, the power and excess frequency fluctuations produced by a fiber amplifier were measured in the LISA measurement band. Relative output power fluctuations of up to $8 \cdot 10^{-3}/\sqrt{\text{Hz}}$ were measured that were up to a factor of 40 above the requirements of $2 \cdot 10^{-4}/\sqrt{\text{Hz}}$ for frequencies between 0.1 mHz and 10 Hz. The setup was sensitive enough to measure excess frequency noise of the fiber amplifier of less than $0.1 \text{ Hz}/\sqrt{\text{Hz}}$ for frequencies between 0.1 mHz and 1 Hz. Suitable actuators for output power and frequency have been identified: the seed laser pump current and the amplifier pump current for the amplifier output power and the frequency actuators of the seed laser (PZT, laser crystal temperature) for the frequency of the amplified radiation. In terms of output power, beam quality, and polarization, the master-oscillator power-amplifier system meets the LISA specifications.

In a master-oscillator power-amplifier concept employing a fiber amplifier, the use of a fiber seed oscillator is attractive in terms of a compact and rugged all-fiber system. A DFB fiber laser with a wavelength of 1063.8 nm has been investigated. It emitted up to 7.9 mW of polarized output power in single longitudinal and transverse mode. For the first time, the free-running frequency fluctuations of a fiber laser were measured in the LISA frequency range. The level of free-running frequency fluctuations was between the levels of frequency fluctuations shown by a high-power NPRO and a low-power NPRO. Also for the first time, the frequency dependent frequency actuator efficiency was measured and a bandwidth four times smaller than encountered in NPROs was found. It was necessary to stabilize the laser frequency to the resonance frequency of a stable Fabry-Perot cavity and the smallest deviations between reference frequency and laser frequency were obtained for frequency-stabilized fiber lasers, i. e. the closest lock of laser frequency to reference frequency was achieved. The fiber laser demonstrated its potential as seed laser in a power-oscillator master-amplifier laser system for LISA. The frequency actuator bandwidth should be increased to enable even more precise locking to a stable reference, a power modulation input is required to stabilize the output power to an external reference, and investigations of the noise properties are necessary when the power is amplified to the 1 W level.

Both the single-stage high-power NPRO and the amplifier seeded by a low-power NPRO are suitable for LISA. Since further investigations of the amplifier system required an improved setup, the LISA baseline was followed and the stand-alone laser was stabilized in power. A small fraction of its output power was sampled with a photodetector, its signal compared with a stable voltage reference and the appropriately amplified difference signal fed back to the laser pump power. Several noise sources were investigated, the most important being the internal noise of electronic references and temperature dependencies of both the photodetector efficiency and the beam splitting ratio at the beam samplers. Two grades of an electronic reference were investigated and both found to be suitable for LISA. Three different photodiodes were characterized and

it was found that the temperature dependency of Si photodiodes was more than five times stronger than was measured for InGaAs and Ge photodiodes. As beam sampling devices, output couplers manufactured with an electron beam technique and with ion beam sputtering were investigated and calculations were performed for glass plates. The reflection coefficient of glass plates showed the lowest temperature dependency. The output power of the NPRO-based LISA laser demonstrator has been stabilized by using glass wedges and temperature-stabilized photodetectors. The best performances were obtained with Si or Ge photodiodes. The power fluctuations of the laser demonstrator could be reduced to a level below $2 \cdot 10^{-4}/\sqrt{\text{Hz}}$ for frequencies ranging from 0.1 mHz to 1 Hz. In this frequency range, this represents the lowest power fluctuations reported to date. When Si photodiodes were used, the measured power stability was temperature limited for frequencies below 20 mHz and loop-gain limited for frequencies above 0.1 Hz.

The NPRO-based laser demonstrator has also been frequency-stabilized to a Fabry-Perot cavity using the Pound-Drever-Hall technique. Its frequency stability was characterized using beat frequency measurements with a second laser that was stabilized to an independent cavity. Several noise sources have been investigated including the effect of temperature fluctuations at the reference cavities and the effect of power fluctuations in the cavities. The requirements concerning the frequency stability of the LISA laser demonstrator have been fulfilled down to 3 mHz. In the remaining frequency band from 1 mHz to 3 mHz, frequency fluctuations of up to $100 \text{ Hz}/\sqrt{\text{Hz}}$ have been obtained, up to a factor of 3 above the requirements. The frequency fluctuations measured are among the lowest that have been reported world-wide in the LISA measurement band. The measurements of frequency stability were limited by the stability of the reference system: Varying offsets in its error signal were measured and it was also shown that the optical cavity showed a significantly reduced finesse compared to the other cavity.

The list of noise sources given in Section 5.4 can be used to further lower the residual laser frequency fluctuations of the beat signal, starting with the removal of the error signal drifts in the reference laser system. In terms of the actual laser source, no specific advantage was found for either a single-stage high-power NPRO or a fiber amplifier seeded by a low-power NPRO. They seem both suitable for LISA. Since space-qualified low-power NPROs are available commercially from Tesat Spacecom¹ and a fiber amplifier emitting 1 W has also been developed, it might technologically be advantageous to investigate the performance of the Tesat devices with respect to LISA, and depending on the outcome, change the baseline from single-stage high-power laser to master-oscillator power-amplifier (MOPA) system. A drawback of a MOPA system might be the radiation hardness of the doped fiber within the amplifier – this issue needs to be investigated or verified. An advantage of a master-oscillator power-amplifier is its scalability to higher output powers in contrast to a single-stage NPRO.

¹http://www.tesat.de/shared/Navig_engl/prod_laser.html

Bibliography

- Alex Abramovici and Jake Chapsky. *Feedback Control Systems: A Fast Track Guide for Scientists and Engineers*. Kluwer Academic Publishers, 2000. 111, 113, 114
- J. W. Armstrong, F. B. Eastabrook, and Massimo Tinto. Time delay interferometry. *Class. Quantum Grav.*, 20:S283–S289, 2003. 10
- Steven J. Augst, T. Y. Fan, and Antonio Sanchez. Coherent beam combining and phase noise measurements of ytterbium fiber amplifiers. *Opt. Lett.*, 29:474–476, 2004. 22
- G. A. Ball, G. Hull-Allen, and J. Livas. Frequency noise of a Bragg grating fibre laser. *Electron. Lett.*, 30:1229–1230, 1994. 37
- Christoph Becher and Klaus-J. Boller. Low-intensity-noise operation of Nd:YVO₄ microchip lasers by pump-noise suppression. *J. Opt. Soc. Am. B*, 16:286–295, 1999. 47
- K. P. Birch and M. J. Downs. An Updated Edlén Equation for the Refractive Index of Air. *Metrologia*, 30:155–162, 1993. 68
- Eric D. Black. An introduction to Pound-Drever-Hall laser frequency stabilization. *Am. J. Phys.*, 69:79–87, 2001. 72, 73, 80
- Eric D. Black and Ryan N. Gutenkunst. An introduction to signal extraction in interferometric gravitational wave detectors. *Am. J. Phys.*, 71:365–378, 2003. 1
- R. B. Blackman and R. B. Tukey. *The measurement of power spectra*. Dover Publications, 1959. 4
- C. Braxmaier, H. Müller, O. Pradl, J. Mlynek, and A. Peters. Tests of Relativity Using a Cryogenic Optical Resonator. *Phys. Rev. Lett.*, 88:010401, 2002. 71
- J.C. Brown. Calculation of a constant Q spectral transform. *J. Acoustical Soc. Am.*, 89:425–434, 1991. 4
- J.C. Brown and M.S. Puckette. An efficient algorithm for the calculation of a constant Q transform. *J. Acoustical Soc. Am.*, 92:2698–2701, 1992. 4

- P. Burdack, M. Tröbs, M. Hunnekuhl, C. Fallnich, and I. Freitag. Modulation-free sub-Doppler laser frequency stabilization to molecular iodine with a common-path, two-color interferometer. *Opt. Express.*, 12:644–650, 2004. 27
- C. L. Carnal and Robert W. Rochelle. Power spectrum estimation with logarithmically uniform frequency resolution: A survey. In *Conference Proceedings of IEEE Southeastcon 84*, pages 418–421, 1984. 4
- W. H. Chung, H. Y. Tam, M. S. Demokan, P. K. A. Wai, and C. Lu. Frequency Stabilization of DBR Fiber Grating Laser Using Interferometric Technique. *IEEE Phot. Techn. Lett.*, 13:951–953, 2001. 37, 39
- Livia Conti, Maurizio De Rosa, and Francesco Marin. Low-amplitude-noise laser for AURIGA detector optical readout. *Appl. Opt.*, 39:5732–5738, 2000. 47, 116
- P. Corredera, M. L. Hernanz, J. Campos, A. Corróns, A. Pons, and J. L. Fontecha. Absolute power measurements at wavelengths at 1300 nm and 1550 nm with a cryogenic radiometer and a tuneable laser diode. *Metrologia*, 37:519–522, 2000. 47
- G. A. Cranch. Frequency noise reduction in erbium-doped fiber distributed-feedback lasers by electronic feedback. *Opt. Lett.*, 27:1114–1116, 2002. 36
- K. Danzmann and Albrecht Rüdiger. LISA technology – concepts, status, prospects. *Class. Quantum Grav.*, 20:S1–S9, 2003. 1, 9, 10
- Timothy Day. *Frequency stabilized solid state lasers for coherent optical communications*. PhD thesis, Stanford University, 1990. 16
- Emmanuel Desurvire. *Erbium-doped fiber amplifiers : principles and applications*. John Wiley & Sohns, Inc., 1994. 33
- J. Dirscherl, B. Neizert, R. Wegener, and H. Walther. A dye laser spectrometer for high resolution spectroscopy. *Opt. Commun.*, 91:131–139, 1992. 71
- Silvano Donati. *Photodetectors : devices, circuits, and applications*. Prentice Hall, 2000. 49, 59, 60
- Richard C. Dorf. *Modern Control Systems*. Addison Wesley, 1992. 31
- R. W. P. Drever, J. L. Hall, F. V. Kowalski, J. Hough, G. M. Ford, A. J. Munley, and H. Ward. Laser Phase and Frequency Stabilization Using an Optical Resonator. *Appl. Phys. B*, 31:97–105, 1983. 36, 37, 40, 72
- ESA-SCI 11, 2000. LISA: System and Technology Study Report, ESA document ESA-SCI 11, 2000. 1, 2, 9, 10, 11, 47, 71
- A. Fellegara, M. Artiglia, S. B. Andreasen, A. Melloni, F. P. Espunes, and S. Wabnitz. COST 241 intercomparison of nonlinear refractive index measurements in dispersion shifted optical fibres at $\lambda = 1550 \text{ nm}$. *Electron. Lett.*, 33:1168–1170, 1997. 28

-
- Joachim Fischer. personal communication, 2004. 68
- Joachim Fischer and Fu Lei. Photodiode nonlinearity measurement with an intensity stabilized laser as radiation source. *Appl. Opt.*, 32:4187–4190, 1993. 47, 68
- N. P. Fox. Trap Detectors and their Properties. *Metrologia*, 28:197–202, 1991. 63
- Andreas Freise. *The Next Generation of Interferometry: Multi-Frequency Optical Modelling, Control Concepts and Implementation*. PhD thesis, University of Hannover, 2003. 111
- I. Freitag, A. Tünnermann, and H. Welling. Power scaling of diode-pumped monolithic Nd:YAG lasers to output powers of several watts. *Opt. Commun.*, 115:511–515, 1995. 2, 10, 11
- Ingo Freitag. *Entwicklung und Charakterisierung einer Laserstrahlquelle für den interferometrischen Nachweis von Gravitationswellen*. PhD thesis, University of Hannover, 1994. 12, 15, 116
- Giacomo Giampieri, Ronald W. Hellings, Massimo Tinto, and James E. Faller. Algorithms for unequal-arm Michelson interferometers. *Opt. Commun.*, 123:669–678, 1996. 10
- S. L. Gilbert. Frequency stabilization of a tunable erbium-doped fiber laser. *Opt. Lett.*, 16:150–152, 1991. 36, 39
- Jean-Francois Giovannelli, Guy Demoment, and Alain Herment. A Bayesian Method for Long AR Spectral Estimation: A Comparative Study. *IEEE Trans. on Ultrasonics, Ferroelectrics, and Frequency Control*, 43:220–233, 1996. 4
- C. C. Harb, M. B. Gray, H.-A. Bachor, R. Schilling, P. Rottengatter, I. Freitag, and H. Welling. Suppression of the Intensity Noise in a Diode-Pumped Neodymium:YAG Nonplanar Ring Laser. *IEEE J. Quantum Electron.*, 30:2907–2913, 1994. 47, 54, 116
- Charles C. Harb, Timothy C. Ralph, H. Huntington, David E. McClelland, and Hans-A. Bachor. Intensity-noise dependance of Nd:YAG lasers on their diode-laser pump source. *J. Opt. Soc. Am. B*, 14:2936–2945, 1997. 47
- Frederic J. Harris. On the Use of Windows for Harmonic Analysis with the Discrete Fourier Transform. *Proc. IEEE*, 66:51–83, 1978. 103, 104, 106, 109
- G. Heinzel, A. Rüdiger, and R. Schilling. Spectrum and spectral density estimation by the Discrete Fourier transform (DFT), including a comprehensive list of window functions and some new flat-top windows, 2002. 100, 104, 108, 109
- Gerhard Heinzel. *Advanced optical techniques for laser-interferometric gravitational-wave detectors*. PhD thesis, University of Hannover, 1999. 31, 73

- Michèle Heurs. *Gravitational waves in a new light: Novel stabilisation schemes for solid-state lasers*. PhD thesis, University of Hannover, 2004. 47
- Michèle Heurs, Volker M. Quetschke, Benno Willke, and Karsten Danzmann. Simultaneously suppressing frequency and intensity noise in a Nd:YAG nonplanar ring oscillator by means of the current-lock technique. *Opt. Lett.*, 29:2148–2150, 2004. 16, 30, 47
- S. Höfer, A. Liem, J. Limpert, H. Zellmer, A. Tünnermann, S. Unger, S. Jetschke, H.-R. Müller, and I. Freitag. Single-frequency master-oscillator fiber power amplifier system emitting 20 W of power. *Opt. Lett.*, 26:1326–1328, 2001. 22
- Michael Hunnekuhl. *Entwicklung weit frequenzabstimmbarer einfrequenter Laserstrahlquellen für Raumfahrtanwendungen*. PhD thesis, University of Hannover, 2004. 10, 15, 16, 23, 116
- Thomas J. Kane. Intensity Noise in Diode-Pumped Single-Frequency Nd:YAG Lasers and its Control by Electronic Feedback. *IEEE Phot. Techn. Lett.*, 2:244–245, 1990. 10, 47, 116
- Thomas J. Kane and Robert L. Byer. Monolithic, unidirectional single-mode Nd:YAG ring laser. *Opt. Lett.*, 10:65–67, 1985. 2, 10, 11
- Thomas J. Kane and Emily A. P. Cheng. Fast frequency tuning and phase locking of diode-pumped Nd:YAG ring lasers. *Opt. Lett.*, 13:970–972, 1988. 116
- Katsuaki Kasai and Mitsuo Ishizu. Amplitude and Frequency Stabilization of a cw Nd:YAG Ring Laser. *Jpn. J. Appl. Phys.*, 33:L230–L232, 1994. 47, 116
- T. C. Larason and S. S. Bruce. Spatial uniformity of responsivity for silicon, gallium nitride, germanium, and indium gallium arsenide photodiodes. *Metrologia*, 35:491–496, 1998. 62, 63
- Fu Lei and Jochim Fischer. Characterization of Photodiodes in the UV and Visible Spectral Region Based on Cryogenic Radiometry. *Metrologia*, 30:297–303, 1993. 62, 63
- A. Liem, J. Limpert, H. Zellmer, and A. Tünnermann. 100-W single-frequency master-oscillator fiber power amplifier. *Opt. Lett.*, 28:1537–1539, 2003. 21
- D. J. Manolakis, V.K. Ingle, and S.M. Kogon. *Statistical and Adaptive Signal Processing : spectral estimation, signal modeling, adaptive filtering and array processing*. McGraw-Hill, 2000. 4, 106
- P. W. McNamara, H. Ward, and J. Hough. Laser frequency stabilisation for LISA: experimental progress. *Adv. Space Res.*, 25:1137–1141, 2000. 71
- Alan C. Nilsson, Eric K. Gustafson, and Robert L. Byer. Eigenpolarization Theory of Monolithic Nonplanar Ring Oscillators. *IEEE J. Quantum Electron.*, 25:767–790, 1989. 11, 12

-
- F. Nocera. LIGO laser intensity noise suppression. *Class. Quantum Grav.*, 21:S481–S485, 2004. 21
- Namkyoo Park, Jay W. Dawson, and Kerry J. Vahala. Frequency locking of an erbium-doped fiber ring laser to an external fiber Fabry-Perot resonator. *Opt. Lett.*, 18:879–881, 1993. 36, 39
- Michael Peterseim. *Entwicklung und Stabilisierung des Lasersystems für die wissenschaftliche Weltraummission LISA*. PhD thesis, University of Hannover, 1999. 2, 37
- William H. Press, Brian P. Flannery, Saul A. Teukolsky, and William T. Vetterling. *Numerical Recipes in C : The Art of Scientific Computing*. Cambridge University Press, 2nd edition, 1992. 66
- Volker Quetschke. *Korrelation von Rauschquellen bei Nd:YAG Lasersystemen*. PhD thesis, University of Hannover, 2003. 16, 30, 116
- Etienne Rochat. *High power optical fiber amplifiers for coherent inter-satellite communication*. PhD thesis, University of Neuchatel, 2000. 22
- T. S. Rose, M. S. Hopkins, and R. A. Fields. Characterization and Control of Gamma and Proton Radiation Effects on the Performance of Nd:YAG and Nd:YLF Lasers. *IEEE J. Quantum Electron.*, 31:1593–1602, 1995. 9
- U. Roth, Thomas Graf, E. Rochat, K. Haroud, Jürg E. Balmer, and Heinz P. Weber. Saturation, Gain, and Noise Properties of a Multipass Diode-Laser-Pumped Nd:YAG CW Amplifier. *IEEE J. Quantum Electron.*, 34:1987–1991, 1998. 22
- Peter Rottengatter. *Simultane Frequenz- und Amplitudenstabilisierung monolithischer Nd:YAG Miniatur-Ringlaser hoher Leistung*. PhD thesis, University of Hannover, 1998. 47
- S. Rowen, A. M. Campbell, K. Skeldon, and J. Hough. Broadband intensity stabilization of a diode-pumped monolithic miniature Nd:YAG ring laser. *J. Mod. Optics*, 41:1263–1269, 1994. 47
- E. Rugi, P. Mueller, and P. Lambelet. Scalable high brightness laser pump for aerospace applications. In *European Conference on Lasers and Electro Optics (CLEO/Europe)*, June 2003. 13
- G. Ruoso, R. Storz, S. Seel, S. Schiller, and J. Mlynek. Nd:YAG laser frequency stabilization to a supercavity at the 0.1 Hz level. *Opt. Commun.*, 133:259–262, 1997. 71
- N. M. Sampas, E. K. Gustafson, and R. L. Byer. Long-term stability of two diode-laser-pumped nonplanar ring lasers independantly stabilized to two Fabry-Perot interferometers. *Opt. Lett.*, 18:947–949, 1993a. 71

- N. M. Sampas, R. Liu, E. K. Gustafson, and R. L. Byer. Frequency stability measurements of two non-planar ring oscillators independently stabilized to two Fabry-Perot interferometers. In Y. C. Chung, editor, *Frequency-stabilized lasers and their applications*, volume 1837, pages 278–288. SPIE, 1993b. 71
- Stefan Seel, Rafael Storz, Giuseppe Ruoso, Jürgen Mlynek, and Stephan Schiller. Cryogenic Optical Resonators: A New Tool for Laser Frequency Stabilisation at the 1 Hz Level. *Phys. Rev. Lett.*, 78:4741–4744, 1997. 71
- Frank Seifert. Entwicklung einer quantenrauschbegrenzten Leistungsstabilisierung für ein Präzisionslasersystem. Master’s thesis, Universität Hannover, Hannover, 2002. 47
- Benjamin S. Sheard, Malcolm B. Gray, David E. McClelland, and Daniel A. Shaddock. Laser frequency stabilization by locking to a LISA arm. *Phys. Lett. A*, 320:9–21, 2003. 10
- Barry L. Shoop, Bardia Pezeshki, Joseph W. Goodman, and James S. Harris, Jr. Laser-Power Stabilization Using a Quantum-Well Modulator. *IEEE Phot. Techn. Lett.*, 4: 136–139, 1992. 47
- Frank Steier. personal communication, 2004a. 70
- Frank Steier. Methoden zur thermo-optischen Charakterisierung optischer Komponenten. Master’s thesis, Universität Hannover, Hannover, 2004b. 67
- K. D. Stock, R. Heine, and H. Hofer. Influence of Inhomogeneity of NIR-Photodiodes on Calibrations at 1047 nm. *Metrologia*, 28:207–210, 1991. 62, 63
- Hardo Stoehr. *Diodenlaser mit Hertz-Linienbreite für ein optisches Calcium-Frequenznormal*. PhD thesis, University of Hannover, 2004. 79
- R. Storz, C. Braxmaier, K. Jäck, O. Prادل, and S. Schiller. Ultrahigh long-term dimensional stability of a sapphire cryogenic optical resonator. *Opt. Lett.*, 23:1031–1033, 1998. 71
- D.T. Teaney, V.L. Moruzzi, and F.C. Mintzer. The tempered Fourier transform. *J. Acoustical Soc. Am.*, 67:2063–2067, 1980. 4
- D.J. Thompson. Spectrum Estimation and Harmonic Analysis. *Proc. IEEE*, 70:1055–1096, 1982. 4
- R.O.R.Y. Thompson. Spectral Estimation from Irregularly Spaced Data. *IEEE Trans. Geoscience Electr.*, Ge-9:220–233, 1971. 4
- Massimo Tinto, Frank B. Estabrook, and J. W. Armstrong. Time-delay interferometry for LISA. *Phys. Rev. D*, 65:082003–1–12, 2002. 10

-
- M. Tröbs, M. Hunnekuhl, P. Burdack, U. Hinze, C. Fallnich, S. Skorupka, G. Heinzl, K. Danzmann, M. Bode, and I. Freitag. Beat measurements of single-frequency lasers independently frequency-locked to thermally shielded high-finesse cavities. In *OSA Trends in Optics and Photonics (TOPS) Vol. 68, Advanced Solid-State Lasers, OSA Technical Digest*, pages WD4-1–WD4-3, 2002. 42
- Ken-ichi Ueda and Noboru Uehara. Laser Diode Pumped Solid State Lasers for Gravitational Wave Antenna. *Proc. SPIE*, 1837:336–345, 1992. 71
- Noboru Uehara and Ken-ichi Ueda. 193-mHz beat linewidth of frequency-stabilized laser-diode-pumped Nd:YAG ring lasers. *Opt. Lett.*, 18:505–507, 1993. 71
- Noboru Uehara and Ken-ichi Ueda. Frequency Stabilization of Two Diode-Pumped Nd:YAG Lasers Locked to Two Fabry-Perot Cavities. *Jpn. J. Appl. Phys.*, 33:1628–1633, 1994. 71
- Peter D. Welch. The Use of Fast Fourier Transform for the Estimation of Power Spectra: A Method Based on Time Averaging Over Short, Modified Periodograms. *IEEE Trans. Audio and Electroacoust.*, AU-15:70–73, 1967. 4, 97
- P. Weßels, M. Auerbach, and C. Fallnich. Narrow-linewidth master oscillator fiber power amplifier system with very low amplified spontaneous emission. *Opt. Commun.*, 205:215–219, 2002. 21
- Peter Weßels. *Intensity noise and beam quality of fiber amplifiers at 1 μm* . PhD thesis, University of Hannover, 2004. 23, 32
- M. G. White and A. Bittar. Uniformity of Quantum Efficiency of Single and Trap-configured Silicon Photodiodes. *Metrologia*, 30:361–364, 1993. 63
- E. A. Whittaker, M. Gehrtz, and G. C. Bjorklund. Residual amplitude modulation in laser electro-optic phase modulation. *J. Opt. Soc. Am. B*, 2:1320–1326, 1985. 82
- B. Willke, S. Brozek, K. Danzmann, V. Quetschke, and S. Gossler. Frequency stabilization of a monolithic Nd:YAG ring laser by controlling the power of the laser-diode pump source. *Opt. Lett.*, 25:1019–1021, 2000. 15, 16, 30, 47, 116, 119
- N. C. Wong and J. L. Hall. Servo control of amplitude modulation in frequency-modulation spectroscopy: demonstration of shot-noise-limited detection. *J. Opt. Soc. Am. B*, 2:1527–1533, 1985. 82, 84
- Amnon Yariv. *Optical electronics*. Saunders College Publishing, 4th edition, 1991. 58
- B. C. Young, F. C. Cruz, W. M. Itano, and J. C. Bergquist. Visible Lasers with Subhertz Linewidths. *Phys. Rev. Lett.*, 82:3799–3802, 1999. 71, 79
- I. Zawischa, M. Brendel, K. Danzmann, C. Fallnich, M. Heurs, S. Nagano, V. Quetschke, H. Welling, and B. Willke. The GEO600 laser system. *Class. Quantum Grav.*, 19:1775–1781, 2002. 21

- I. Zawischa, K. Plamann, C. Fallnich, H. Welling, H. Zellmer, and A. Tünnermann. All-solid-state neodymium-based single-frequency master oscillator fiber power-amplifier system emitting 5.5 W of radiation at 1064 nm. *Opt. Lett.*, 24:469–471, 1999. 21
- Jing Zhang, Hong Chang, Yiaojun Jia, Hongxiang Lei, Runlin Wang, Changde Xie, and Kunchi Peng. Suppression of the intensity noise of a laser-diode-pumped single-frequency ring Nd:YVO₄-KTP green laser by optoelectronic feedback. *Opt. Lett.*, 26: 695–697, 2001. 47

A. Improving spectral estimation on logarithmic frequency axes

A popular method for spectral estimation with uniform frequency resolution for the case of abundant equidistant samples is the so-called ‘overlapped segmented averaging of modified periodograms’. Here a periodogram means the discrete Fourier transform (DFT) of one segment of the time series, while modified refers to the application of a time-domain window function and averaging is used to reduce the variance of the spectral estimates. This method is attributed to Welch (Welch, 1967) and is also known under various acronyms such as WOSA (for ‘windowed overlapped segmented average’).

Modern data acquisition equipment easily allows the collection of very long time series. This leads to spectra covering several decades of frequency which are often plotted on a logarithmic frequency axis in order to display a maximum of information. The results from a direct application of the WOSA method are, however, equidistant in the frequency domain. A trade-off is necessary between frequency resolution of the spectrum and the number of averages. Especially with a logarithmically scaled frequency axis spanning several decades the problem becomes obvious: While at low frequencies a narrow frequency resolution is necessary, this resolution leads to an inconvenient density of data-points at higher frequencies, where instead better averaging is desirable.

While the WOSA method uses the same frequency resolution for every Fourier frequency, the new method named LPSD (for Logarithmic frequency axis Power Spectral Density) adjusts the frequency resolution for every Fourier frequency in the estimate. The property of the WOSA method that the distance between adjacent Fourier frequencies equals the resolution bandwidth, is approximately maintained.

In this Appendix, the LPSD method is described. In Section A.1 segmentation of the time series, subtraction of the average value of each segment, multiplication with a window function, computation of the discrete Fourier transforms, and calculation and averaging of their squared magnitudes, all of which are common to both the classical WOSA and the new method are reviewed. In Section A.2 the novel method of selecting equally spaced Fourier frequencies on a logarithmically spaced axis is described. The main difference between the WOSA method and the LPSD method is that the WOSA method computes scalar products of the modified time series with a complete set of complex exponentials using integer frequency bins while the new method uses individual non-integer bins in the frequency domain. Section A.3 discusses the effects of segment overlapping and in Section A.4 the effects of non-integer bins on the estimate are studied. Section A.5 contains the important topic of proper calibration of spectral estimates.

Symbol	Comment
α	parameter for Kaiser window
$a(j, k)$	average value of segment k
$A(j, k, m(j))$	discrete Fourier transform of $G(j, k, l)$
C	normalization factor for spectral estimate
$C_{PS}(j)$	calibration coefficient for power spectrum estimation
$C_{PSD}(j)$	calibration coefficient for power spectral density estimation
$D(j)$	segment offset
ENBW	equivalent noise bandwidth
$f(j)$	Fourier frequencies in spectral estimate, $j = 0, \dots, J - 1$
f_{\max}	largest frequency in spectral estimate
f_{\min}	smallest frequency in spectral estimate
f_s	sampling frequency of the time-series
g	$g = \log(f_{\max}) - \log(f_{\min})$
$G(j, k, l)$	data segment minus segment average multiplied by window function
J	actual number of Fourier frequencies $f(j)$ in spectral estimate
J_{des}	desired number of Fourier frequencies $f(j)$ in spectral estimate
j	index $j = 0, \dots, J - 1$ of Fourier frequencies $f(j)$
$K(j)$	number of averages for Fourier frequency $f(j)$
K_{des}	desired number of averages
K_{\min}	minimum number of averages
L	constant number of data in one segment
$L(j)$	number of data in one segment
l	data index within one segment $l = 0, \dots, L(j) - 1$
$m(j)$	frequency index, $m(j) = f(j)/r(j)$
N	total number of data
n	index of data $x(n)$, $n = 0, \dots, N - 1$
$P(f(j))$	spectral estimate for Fourier frequency $f(j)$
r	constant resolution bandwidth
$r(j)$	frequency resolutions in spectral estimate, $j = 0, \dots, J - 1$
$r'(j), r''(j), r'''(j)$	preliminary frequency resolution
r_{avg}	smallest frequency resolution with K_{des} averages
r_{\min}	frequency resolution corresponding to K_{\min} averages
S_1	constant sum of all window values
$S_1(j)$	sum of all window values
S_2	constant sum of all squared window values
$S_2(j)$	sum of all squared window values
$w(j, l)$	window function for Fourier frequency $f(j)$
$x(n)$	time series of equidistant samples $n = 0, \dots, N - 1$
$x_k(j, l)$	data segment k , $k = 0, \dots, K(j) - 1$, $l = 0, \dots, L(j) - 1$
ξ	segment overlap
$z(j, l)$	abbreviation for definition of Hanning window

Table A.1.: Commonly used symbols.

Section A.6 discusses the effect of aliasing for small frequency bins and in Section A.7 a step-by-step list for the implementation of the LPSD algorithm is given.

A.1. The WOSA method

Consider the N equidistant samples $x(n)$, $n = 0 \dots N - 1$ of a signal x that have been sampled with sampling frequency f_s . Furthermore, take a set of J Fourier frequencies $f(j)$, $j = 0 \dots J - 1$ at which the periodogram of x will be evaluated. The bandwidth at each of the frequencies is denoted $r(j)$ and is not necessarily constant (see Section A.2). Then, for each j (i.e. for each Fourier frequency $f(j)$) the following is done:

The data are divided into overlapping segments of length $L(j)$ with the starting points of these segments $D(j)$ samples apart as is illustrated in Fig. A.1. Here, the

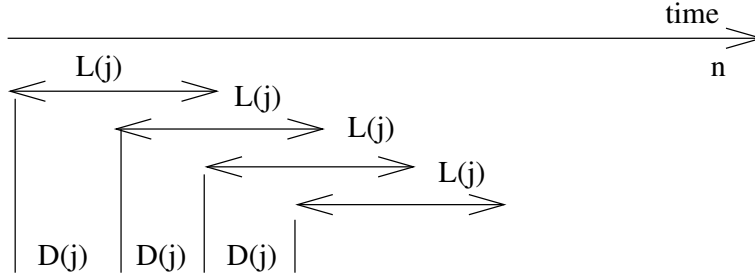


Figure A.1.: Segmentation of the data stream.

segment length $L(j)$ depends on sampling frequency f_s and resolution bandwidth $r(j)$:

$$L(j) = f_s / r(j). \quad (\text{A.1})$$

Note that the $r(j)$ must be chosen in such a way that $L(j)$ are integers. The $D(j)$ depend on the fractional overlap ξ ($0 \leq \xi < 1$) of the segments:

$$D(j) = (1 - \xi) \cdot L(j). \quad (\text{A.2})$$

The data of segment k is given by $\{x(l + kD(j)), \quad l = 0, \dots, L(j) - 1\}$. Suppose $K(j)$ such segments ($k = 0, \dots, K(j) - 1$) are given. It is easily shown that $K(j)$ is given by

$$K(j) = \text{floor} \left(\frac{N - L(j)}{L(j)(1 - \xi)} + 1 \right), \quad (\text{A.3})$$

where $\text{floor}()$ takes the largest integer smaller or equal to its argument. For each segment the mean value

$$a(j, k) = \frac{1}{K(j)} \sum_{l=0}^{L(j)-1} x(l + kD(j)) \quad k = 0, \dots, K(j) - 1 \quad (\text{A.4})$$

is calculated that will be subtracted from each segment to reduce spectral leakage (see also Section A.3).

In order to calculate a spectral estimate, a data window $w(j, l)$, $l = 0 \dots, L(j) - 1$, is selected and the windowed sequences ($k = 0, \dots, K(j) - 1$)

$$G(j, k, l) = [x(l + kD(j)) - a(j, k)] w(j, l), \quad l = 0, \dots, L(j) - 1, \quad (\text{A.5})$$

are formed where the mean has been subtracted separately for each segment.

A brief discussion of windowing and segment overlapping can be found in Section A.3 and a detailed discussion is given in Heinzl et al. (2002). Then the scalar products $A(j, k)$ of these sequences with the complex exponential of the appropriate Fourier frequency $f(j)$ are computed:

$$A(j, k) = \sum_{l=0}^{L(j)-1} G(j, k, l) \exp(-2\pi i \frac{m(j)l}{L(j)}) \quad k = 0, \dots, K(j) - 1 \quad (\text{A.6})$$

with

$$m(j) = f(j)/r(j) \quad (\text{A.7})$$

being the bin number ¹, further discussed in Section A.4 below.

The squared magnitudes of the complex scalar products $|A(j, k)|^2$ are obtained. Finally, the spectral estimate at the Fourier frequency $f(j)$ is the average of these squared magnitudes, i. e.

$$P(f(j)) = \frac{C}{K(j)} \sum_{k=0}^{K(j)-1} |A(j, k)|^2, \quad (\text{A.8})$$

where C is a normalization factor that will be discussed in Section A.5, and the relation between Fourier frequency $f(j)$ and frequency bin number $m(j)$ is given by

$$f(j) = m(j) \cdot \frac{f_s}{L(j)}. \quad (\text{A.9})$$

A.2. Fourier frequencies, frequency resolutions, and bins

If J_{des} Fourier frequencies $f(j)$ are to be spaced equally on a logarithmic axis ranging from f_{min} to f_{max} , the logarithms of the frequencies obey the linear equation

$$\log(f(j)) = \log(f_{\text{min}}) + \frac{j}{J_{\text{des}} - 1} (\log(f_{\text{max}}) - \log(f_{\text{min}})) \quad (\text{A.10})$$

with $j = 0, \dots, J_{\text{des}} - 1$, and the frequency limits being bounded by

$$\frac{f_s}{N} \leq f_{\text{min}} < f_{\text{max}} \leq \frac{f_s}{2} \quad (\text{A.11})$$

¹Note that for each Fourier frequency $f(j)$ the data is segmented differently, such that a Fast Fourier Transform (which provides results for all frequency bins with a given segmentation) is usually inefficient, and direct computation of Eq. (A.6) is often faster.

according to the total length of the time series and the Nyquist criterion, respectively. Using the abbreviation

$$g := \log(f_{\max}) - \log(f_{\min}) \quad (\text{A.12})$$

Eq. (A.10) can be rewritten to

$$f(j) = f_{\min} \cdot \exp\left(\frac{jg}{J_{\text{des}} - 1}\right). \quad (\text{A.13})$$

In analogy to the WOSA method a frequency resolution $r(j)$ at Fourier frequency $f(j)$ is aimed for that equals the difference to the next higher Fourier frequency² $f(j+1)$

$$r'(j) = f(j+1) - f(j) \quad (\text{A.14})$$

which is solved for the preliminary estimate $r'(j)$:

$$r'(j) = f_{\min} \exp\left(\frac{jg}{J_{\text{des}} - 1}\right) \left(\exp\left(\frac{g}{J_{\text{des}} - 1}\right) - 1 \right) \approx f(j) \frac{g}{J_{\text{des}} - 1}. \quad (\text{A.15})$$

As will be shown, for common values of N and J_{des} , it is typically not possible to produce spectral estimates at Fourier frequencies $f(j)$ according to Eq. (A.13) and frequency resolutions according to Eq. (A.15). In the following $N = 10^6$, $J_{\text{des}} = 1000$, $f_s = 2 \text{ Hz}$, $f_{\min} = f_s/N = 2 \text{ }\mu\text{Hz}$, and $f_{\max} = f_s/2 = 1 \text{ Hz}$ will be used as example. This leads to a desired frequency spacing of $r'(0) = 26 \text{ nHz}$ between the first two Fourier frequencies which is much smaller than the smallest possible frequency resolution $f_s/N = 2 \text{ }\mu\text{Hz}$.

It turns out that typically for the higher Fourier frequencies, suitable parameters $r(j)$ and $K(j)$ can be found without restrictions, while in the lower end of the spectrum the aim of equally spaced Fourier frequencies on the logarithmically scaled axis needs to be abandoned. To allow a tradeoff between the number of averages and the uniformity of the Fourier frequencies on the logarithmic axis, an additional parameter in the algorithm is introduced, the desired number of averages K_{des} , with typical values of $K_{\text{des}} \approx 100$. This corresponds to a frequency resolution

$$r_{\text{avg}} = \frac{f_s}{N} \cdot (1 + (1 - \xi)(K_{\text{des}} - 1)) \quad (\text{A.16})$$

that also depends on the overlap of the segments and is a constant for each run of the full algorithm. With an overlap of $\xi = 0.3$, $K_{\text{des}} = 100$, and the example values mentioned above, $r_{\text{avg}} = 141 \text{ }\mu\text{Hz}$ follows. This means that only for frequency resolutions (spacing between adjacent Fourier frequencies) above $141 \text{ }\mu\text{Hz}$ it is possible to obtain the desired number of averages.

²For any reasonable number of Fourier frequencies on the x-axis it makes no practical difference whether the distance to the next higher frequency, the distance to the next lower frequency or their average is used.

The smallest possible frequency resolution r_{\min} is given by f_s/N . If it is desired to use at least K_{\min} averages for each Fourier frequency ($K_{\min} \geq 1$), then one should use

$$r_{\min} = \frac{f_s}{N} \cdot (1 + (1 - \xi)(K_{\min} - 1)) \quad (\text{A.17})$$

instead.

The procedure to determine suitable Fourier frequencies and corresponding frequency resolutions is as follows:

1. Start at f_{\min} , let $j = 0$, $f(j = 0) = f_{\min}$.
2. Determine the frequency resolution $r'(j)$ according to Eq. (A.15). Then compute

$$r''(j) = \begin{cases} r'(j) & : r'(j) \geq r_{\text{avg}} \\ \sqrt{r_{\text{avg}} \cdot r'(j)} & : r_{\min} \leq r'(j) < r_{\text{avg}} \\ r_{\min} & : r'(j) < r_{\min} \end{cases} \quad (\text{A.18})$$

For $r'(j) \geq r_{\text{avg}}$, one can obtain both the desired spacing on the logarithmic axis and reach or exceed the desired number of averages. If, on the other hand, $r'(j) < r_{\min}$, the minimum number of averages cannot be achieved, and one has no choice but to use r_{\min} as frequency resolution. Finally, if $r_{\min} \leq r'(j) < r_{\text{avg}}$ a heuristic compromise between an equally spaced logarithmic frequency axis and the desired number of averages is chosen.

3. From $r''(j)$ the closest integer segment length $L(j)$ is calculated by

$$L(j) = \text{round} \left(\frac{f_s}{r''(j)} \right). \quad (\text{A.19})$$

4. The final frequency resolution $r(j)$ is obtained from the integer segment length $L(j)$ by

$$r(j) = \frac{f_s}{L(j)} \quad (\text{A.20})$$

and the frequency bin number $m(j)$ from Eq. (A.7). Note that $m(j)$ can be non-integer (see Section A.4).

5. The next Fourier frequency is given by

$$f(j + 1) = f(j) + r(j). \quad (\text{A.21})$$

If $f(j + 1) < f_{\max}$ one increases j by 1 and goes to step 2.

6. Finally, the actual number of Fourier frequencies obtained is given by $J = j + 1$. Since usually for the lower frequencies one has $r'(j) < r_{\text{avg}}$ in step 2, this will be less than were aimed for. The spacing of Fourier frequencies at the upper end of the spectrum, however, corresponds to $J = J_{\text{des}}$.

A.3. Windowing and overlap of segments

Each segment of length $L(j)$ is multiplied with a window function before being subjected to the DFT. One common feature of the variety of window functions (see e.g. Harris (1978)) is that they have a maximum in the middle and tend to zero near the beginning and the end. The effect on the data is two-fold: the benefit of a window function is to make the modified data quasi-continuous. This reduces spectral leakage, i. e. the transfer of power from one frequency bin to neighboring frequencies. The other effect is that the data in the middle have a stronger weight than the data at the beginning and at the end, which is undesirable in principle, because all data intrinsically have the same importance. The remedy is to use overlapping segments as is illustrated below.

As an example of a window function the Hanning window defined by (see Harris (1978))

$$w(j, l) = \frac{1 - \cos(z(j, l))}{2} = \cos^2\left(\frac{z(j, l) - \pi}{2}\right) \quad \text{with} \quad (\text{A.22})$$

$$z(j, l) = \frac{2\pi \cdot l}{N} \quad \text{and} \quad l = 0, \dots, L(j) - 1.$$

is used.

For normalization purposes two sums are defined, specific to a window function, that are needed for calibrating the spectral estimates (see Section A.5):

$$S_1(j) = \sum_{l=0}^{L(j)-1} w(j, l), \quad (\text{A.23})$$

$$S_2(j) = \sum_{l=0}^{L(j)-1} w^2(j, l). \quad (\text{A.24})$$

When the time series of data is divided into non-overlapping segments that are multiplied with a window function, one has a situation as illustrated in Fig. A.2. Due

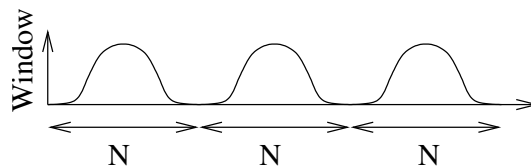


Figure A.2.: Non-overlapping segmented data stream with window.

to the fact that the window function is typically very small or zero near its boundaries, a significant portion of the data is effectively ignored in the analysis. This is clearly not optimal in cases where the data has been produced at great expense and maximal information is to be extracted from it. The situation can be improved by letting the segments overlap as illustrated in Fig. A.3. The amount of overlap is a tradeoff between

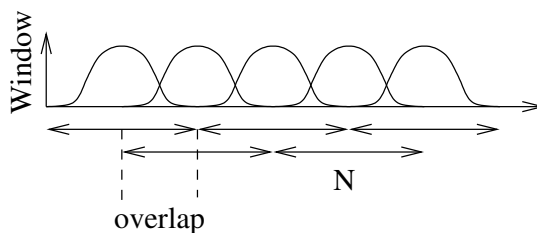


Figure A.3.: Data stream with overlapping segments and window.

computational effort and flatness of the data weighting. A detailed discussion of segment overlap, along with a comprehensive list of window functions and some new flat-top windows can be found in Heinzel et al. (2002).

A.4. Non-integer frequency bin numbers

Both the WOSA and the LPSD method for spectral estimation calculate scalar products of windowed data segments with complex exponentials. The main difference between WOSA and LPSD is that the former uses a complete set of integer bin numbers while the latter uses individual non-integer bin numbers in the frequency domain. The transfer function of several windows for integer and non-integer bin numbers has been investigated. Since the phase information in the spectral estimate is discarded, it is ignored in this discussion. The transfer function magnitude $|H(f)|$ has been calculated using

$$H(f) = \sum_{l=0}^{L-1} \sin\left(\frac{2\pi fl}{L}\right) w(l) \exp\left(\frac{-2\pi ilm}{L}\right), \quad (\text{A.25})$$

where f is the frequency of the sinusoidal test function in units of bins, $w(l)$ the window function under investigation, and m the frequency bin number of interest. Figure A.4 shows the magnitude of the frequency response of a Hanning window to a sinusoidal input signal for frequencies ranging from 0 to 15, for fixed frequency bin numbers of 6 and 6.23.

At the respective bin number, the window-function responses equal 0 dB, as is expected. Further away, the responses drop and side-lobes are visible. The drop in frequency response between the main lobe and the highest side lobes is called peak side lobe level (PSLL). For the Hanning window this is -31.5 dB for both the integer and the non-integer case.

The PSLL is an important characteristic of a window function: it describes the amount of suppression of spectral leakage of peaks to neighboring frequencies. To obtain spectra without artifacts, a window function with an appropriate PSLL must be chosen. For Figs. 2.1–2.3 and A.5–A.7 a Kaiser window (Harris, 1978) with its parameter $\alpha = 3.826$ corresponding to a PSLL of -90 dB has been used.

Figure A.4 shows that the frequency response for non-integer bin numbers slightly differs from the integer case, but since these differences only occur below the PSLL of the window, they have no effect on the spectrum estimate and can be neglected.

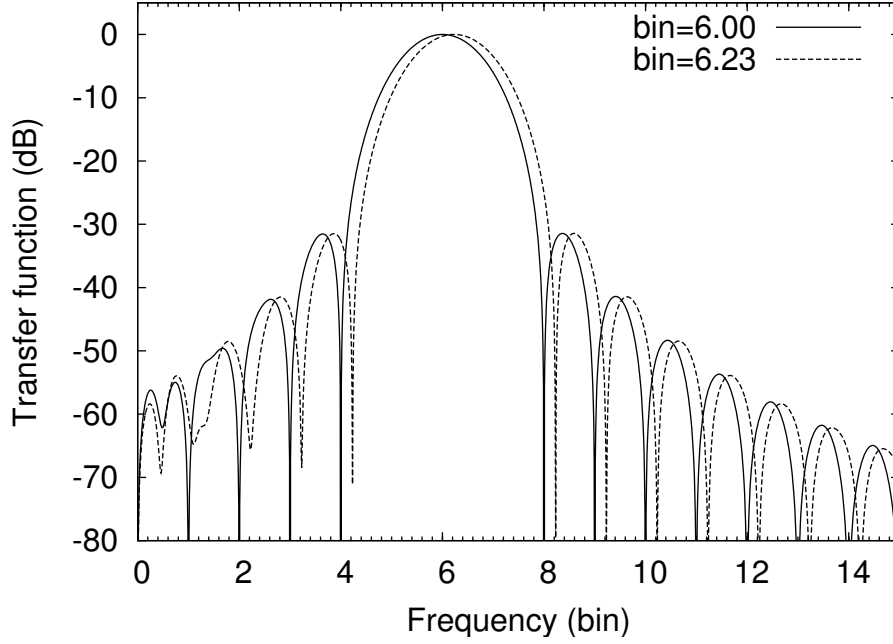


Figure A.4.: Magnitude of the Hanning window frequency response for sinusoidal signals.

Abbrev.	Name	Relation for constant ENBW	Unit
PSD	power spectral density		V^2/Hz
PS	power spectrum	$PS = PSD \cdot ENBW$	V^2
LSD	linear spectral density	$LSD = \sqrt{PSD}$	$V/\sqrt{\text{Hz}}$
LS	linear spectrum	$LS = \sqrt{PS} = LSD \cdot \sqrt{ENBW}$	V

Table A.2.: Naming convention for spectra. ENBW is the equivalent noise bandwidth, defined in Eq. (A.26).

This comparison has been performed for many window functions and bin numbers and consistently found that no significant differences exist between integer and non-integer bins, provided that the bin number is higher than the effective half-width of the window transfer function in the frequency domain, measured at the PSL.

A.5. Calibration of spectral estimates

The result of any spectral estimation algorithm can be scaled as spectral density or spectrum. Spectral densities are commonly used to estimate the incoherent content of a measured quantity, e. g. a noise floor or a wide-band signal. Spectra, on the other hand, are used to measure the amplitude of sinusoidal peaks. Table A.2 shows four commonly used calibrations for spectral estimates and their relationships. Spectral densities and

spectra with constant frequency resolution can be converted to each other when the equivalent noise bandwidth ENBW is known. It is computed as

$$\text{ENBW} = r \cdot \text{NENBW} = \text{NENBW} \cdot \frac{f_s}{L} = f_s \frac{S_2}{(S_1)^2}, \quad (\text{A.26})$$

where

$$\text{NENBW} = \frac{LS_2}{(S_1)^2} \quad (\text{A.27})$$

is the normalized equivalent noise bandwidth (Harris, 1978), r the frequency resolution used to calculate the estimate, f_s the sampling frequency, $L = f_s/r$ the length of the Fourier transforms and S_1 and S_2 window-function-specific sums defined by Eqs. (A.23, A.24) in Section A.3.

The calibration coefficient for power spectrum estimation $C_{\text{PS}}(j)$ is hence given by

$$C_{\text{PS}}(j) = \frac{2}{(S_1(j))^2} \quad (\text{A.28})$$

and the corresponding coefficient $C_{\text{PSD}}(j)$ for power spectral density is defined as

$$C_{\text{PSD}}(j) = \frac{2}{f_s S_2(j)}, \quad (\text{A.29})$$

where the sums defined in Eqs. (A.23) and (A.24) have been used. The linear quantities LSD and LS can be found by taking the square root of PSD or PS, respectively, after averaging has been completed.

For Figs. A.5–A.7 (and previously for Figs. 2.1–2.3) the measured input voltage noise of an operational amplifier sampled with a digital voltmeter has been used. For illustrative purposes, two sinusoidal signals, both with $20 \mu\text{V}_{\text{rms}}$ amplitude and frequencies of 1.23×10^{-4} Hz and 2.5×10^{-2} Hz, and a 3.5 dB notch at 0.16 Hz have additionally been introduced by digital processing of the measured data.

Figure A.5 shows a linear spectrum estimate of the time series by the WOSA method. The peak height is $20 \mu\text{V}_{\text{rms}}$ at the correct frequencies.

Figure A.6 shows a linear spectrum estimate of the same time series by the WOSA method, but this time two different frequency resolutions have been used. As a result, the noise floor shows a discontinuity at 5 mHz. The peak heights have however been preserved.

Figure A.7 shows the result of the new LPSD method. Peak heights have been preserved and due to the continuous adjustment of the frequency resolution, the noise floor is continuous.

A.6. Aliasing for small frequency bins

It is well known that windowing of data segments is necessary in the WOSA method to reduce the bias of the spectral estimate (Manolakis et al., 2000). When calculating one-sided spectral estimates containing only positive Fourier frequencies windowing causes

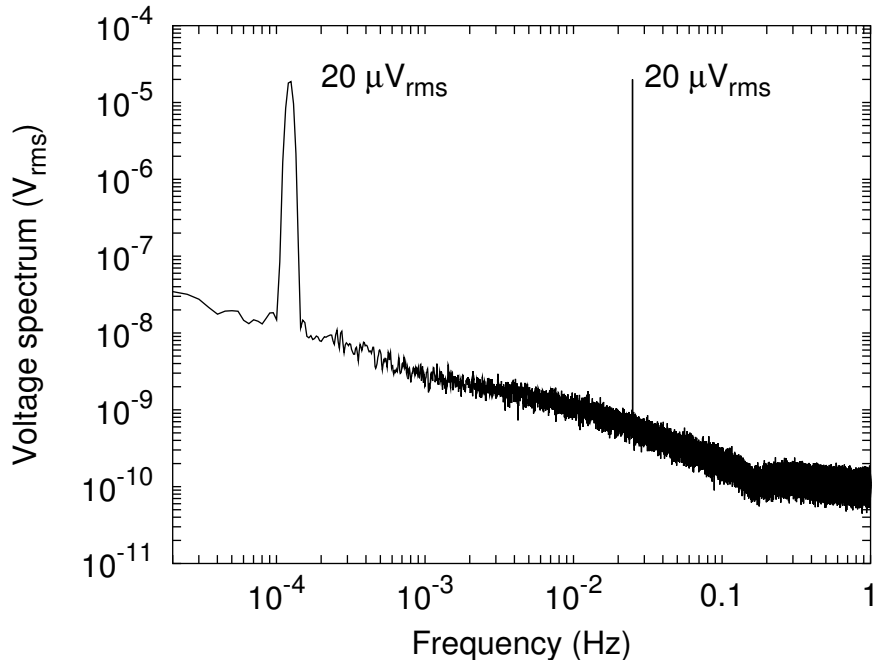


Figure A.5.: Spectrum estimate obtained by Welch's method of Windowed, Overlapped Segmented Average (WOSA); $5 \mu\text{Hz}$ resolution, 10 averages.

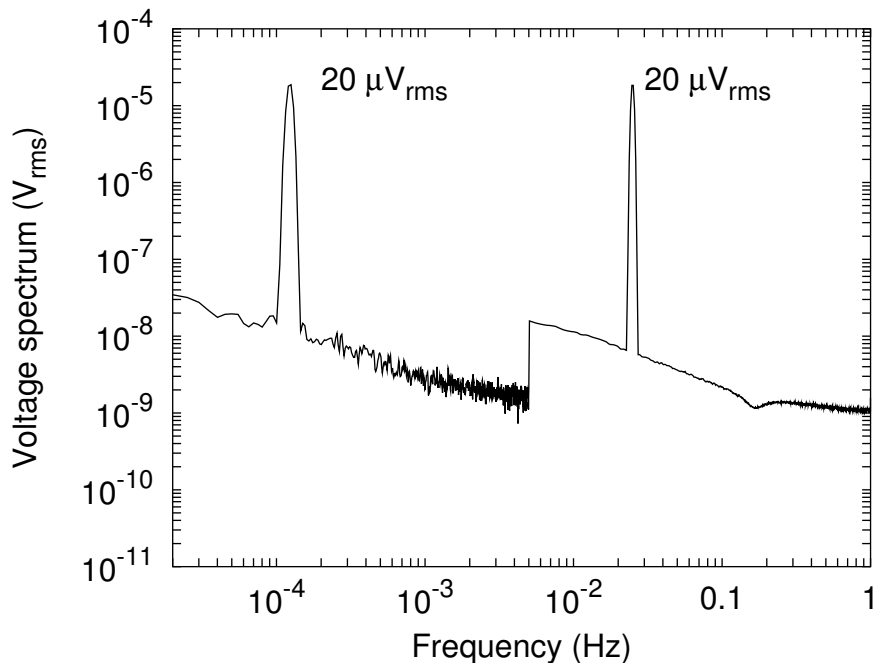


Figure A.6.: Spectrum estimate obtained by combining the results of the WOSA method with two different frequency resolutions; $5 \mu\text{Hz}$ and $500 \mu\text{Hz}$ resolution, 10 and 1266 averages. Peak heights are preserved, but the noise floor shows a discontinuity due to the change of resolution bandwidth.

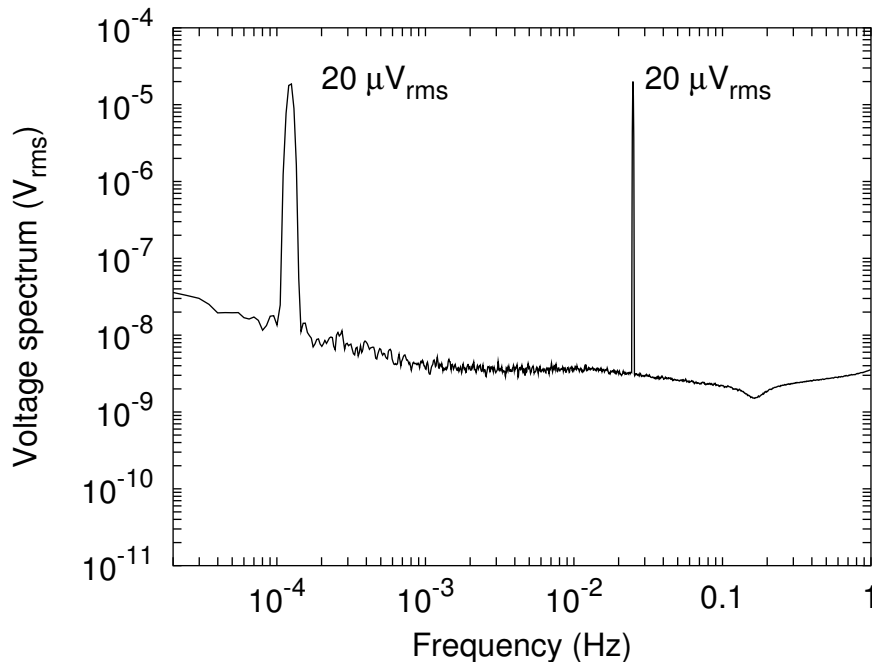


Figure A.7.: Spectrum estimate obtained by the new LPSD method. The resolution bandwidth is adjusted to the frequency to obtain more averages at higher frequencies; 5 μHz to 5.4 mHz resolution, 10 to 12982 averages.

a bias at low frequency bins – a fact that is also well known: one cannot trust the lowest frequency bins on the spectrum analyzer. The bias stems from aliasing of power from negative bins and bin zero to the lowest positive frequency bins. Aliasing from bin zero can be eliminated by subtracting the mean data value from the segment. Aliasing from negative bins however, cannot be reduced that way. Hence the first few frequency bins should not be used. The first frequency bin that yields unbiased spectral estimates depends on the window function used. The bin is given by the effective half-width of the window transfer function. Values for a variety of windows are tabulated in Heinzel et al. (2002).

A.7. Algorithm summary

In this section the implementation of the LPSD algorithm for spectrum and spectral density estimation is summarized. It was programmed in C and executable programs for Linux and DOS/Windows have been compiled. The source code is available upon request. Readers requiring a different implementation (e.g. in Matlab, Mathcad, etc.) may use this summary as a guideline.

Input data A long stream $x(n)$, $n = 0, \dots, N - 1$ of equally spaced input data sampled with frequency f_s be given. Typical values for N range from 10^4 to $> 10^6$.

Window function Choose a window function $w(j, l)$ to reduce spectral leakage within the estimate. Lists of window functions can be found in Harris (1978) and Heinzl et al. (2002). The computations of the window function will be performed when the segment lengths $L(j)$ have been determined.

Fourier frequencies, resolutions, and bins Calculate Fourier frequencies $f(j)$ ranging from f_{\min} to f_{\max} , frequency resolutions $r(j)$, and frequency bins $m(j)$ according to steps 1 to 5 in Section A.2 with j ranging from 0 to $J - 1$. A typical value for J is 1000.

For every Fourier frequency $f(j)$ do:

Splitting of the data stream The segment length $L(j)$ is determined from the $r(j)$ calculated in the previous step by using Eq. (A.20). Split the data into segments of length $L(j)$, overlapping as desired. Remove the mean of each segment if desired.

DFT Compute the window function $w(j, l)$ with l running from 0 to $L(j) - 1$. Multiply each data segment with the window function (Eq. (A.5)), and compute the discrete Fourier transforms (Eq. (A.6)).

Averaging and calibration Average the squared magnitudes of Eq. (A.6) and apply the desired calibration factor according to Eq. (A.8). Table A.2 and Eqs. (A.28), (A.29) can be used to determine the desired calibration factor.

B. Basic properties, design, and characterization of control loops

B.1. Basics

Control loops can be used for many different applications. Their purpose is to keep a physical parameter as close as possible to a predefined value, which is often constant in the presence of disturbances acting on the physical parameter. Considering laser frequency and laser power stabilizations as examples, basic properties of control loops are described and procedures are given for designing them. From the many kinds of control loops, this text focusses on the linear and analogue type. A good textbook on linear control loops can be found in Abramovici and Chapsky (2000), and Appendix B of Freise (2003) gives a good summary on linear analogue control loops.

B.1.1. Transfer functions

To design, and characterize linear control loops, the concept of transfer functions will be used. The transfer function H of a system with input x and output y is given by $H = y/x$. The transfer function H is a complex function and it is customary to plot its magnitude and phase (see Section B.1.4) instead of its real and its imaginary part. Transfer functions are defined in the frequency domain, i. e. the transfer function and its input and output will be considered as functions of frequency instead as functions of time. The advantage of operating in the frequency domain in contrast to operating in the time domain is that the (frequency) response of a system is simply given as product of input and transfer function, whereas in the time domain the output of a system is the convolution of the input with the inverse Fourier transform of the transfer function, which is more difficult to calculate. In addition, in the frequency domain, the frequency response of two systems with transfer functions $H_1(f)$ and $H_2(f)$ is given by the product of the transfer functions $H_1(f) \cdot H_2(f)$.

B.1.2. Schematic representation of a control loop

A schematic representation of a control loop is shown in Fig. B.1. Suppose, the output power of a laser has to be stabilized. In Fig. B.1 the control path represents the laser and the controlled signal the output power. To stabilize the output power an error signal

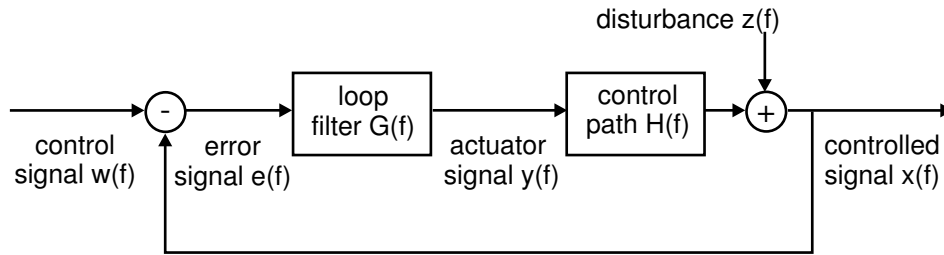


Figure B.1.: Schematic representation of a control loop; the controlled signal of the control path is subject to disturbances; to reduce them, the controlled signal is compared with a control signal and the difference (the error signal) is amplified by the loop filter and fed back to an actuator within the control path.

e is generated. It is proportional to the difference of the control signal w (the reference) and the controlled signal x . The error signal is appropriately filtered by the loop filter and fed back to the laser to modify its output power. In Fig. B.1, H denotes the transfer function of the controlled system from the actuator signal to the error signal, and G is the transfer function of the loop filter from error signal to actuator signal. The noise sources in the control path that are to be suppressed are represented by z . The point within the control loop, where the error signal is generated, is called error point. The point, where a signal is sent to the actuator within the control path, is called actuator point.

B.1.3. Noise transfer and noise suppression in control loops

Figure B.2 shows a more detailed schematic of a control loop than Fig. B.1. In addition

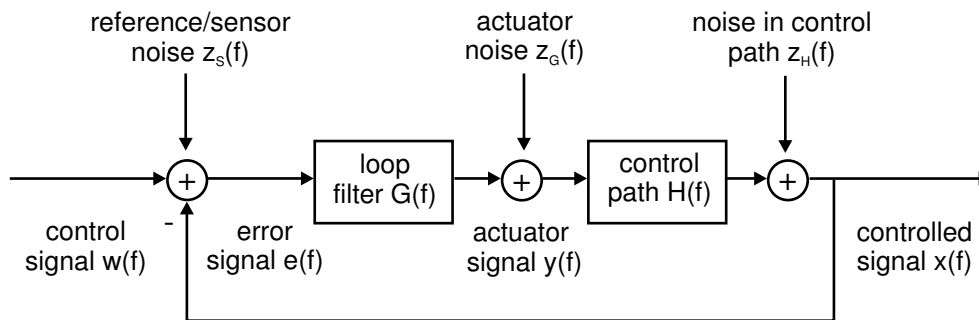


Figure B.2.: Schematic representation of a control loop with different noise sources: the noise z_H within the control loop is to be suppressed by the loop gain; z_S is reference noise or sensor noise; this noise is transferred to the controlled signal x ; z_G is for example actuator noise or other noise within the loop filter; z_G is suppressed by the loop filter gain.

to noise z_H entering the control loop in the control path, noise also enters the loop at

the error point (z_S) and at the actuator point (z_G). Noise z_S entering the loop at the error point can be noise within the reference signal w or noise entering the loop in the sensor that generates the error signal e .

The dependency of the controlled signal x from the control signal w (reference) in the presence of noise z_H is easily derived from Fig. B.2. One can see that $x = (z_H + GH)e$ and $e = w - x$, which is readily combined to Eq. (B.1):

$$x = \frac{GH}{1 + GH}w + \frac{1}{1 + GH}z_H \quad (\text{B.1})$$

H and G are the transfer functions of control path and loop filter, respectively, and the control loop includes an explicit minus sign as shown in Fig. B.2. It has been assumed that no noise is inserted into the loop at the error point ($z_S = 0$) and at the actuator point ($z_G = 0$). For large loop gains $GH \gg 1$ the controlled signal x follows the control signal w ($GH/(1 + GH) \approx 1$) and noise inserted into the loop within the control path is suppressed by the loop gain GH (since $1/(1 + GH) \approx GH$).

If noise z_S added into the loop at the error point and noise z_G added into the loop at the actuator point are considered one finds

$$x = \frac{GH}{1 + GH}w + \frac{GH}{1 + GH}z_S + \frac{H}{1 + GH}z_G + \frac{1}{1 + GH}z_H \quad (\text{B.2})$$

For large loop gains GH the controlled signal x not only follows the reference. In addition, noise within the reference or the sensor is transferred to the controlled signal. This means that great care must be taken when the reference and the sensor are designed. According to Eq. (B.2) actuator noise is suppressed by the loop filter gain, which means that the design of the actuator is less critical in terms of noise than the design of the sensor.

B.1.4. Bode diagrams and control loop stability

Control loops are mathematically described by their so-called open-loop gain GH . It can be thought of as a transfer function obtained by opening the control loop at an arbitrary point, inserting (sinusoidal) signals at that point and measuring the frequency response of the open loop.

It has proven useful and in most cases sufficient to describe control loops by Bode plots of their complex open loop gain in contrast to Nyquist diagrams (Abramovici and Chapsky, 2000, p. 20) which are not discussed here. A Bode plot of an open loop gain consists of two graphs: the magnitude and the phase – both plotted as a function of frequency. The magnitude of the open loop gain is conventionally expressed in decibel and the corresponding phase is plotted on a linear scale. Often a logarithmic frequency axis is used.

As an example Fig. B.3 shows the Bode plot of a frequency stabilization open-loop gain. The so-called unity gain frequency f_{UGF} , with $G(f_{UGF})H(f_{UGF}) = 1$ is about 8 kHz. An important figure for the stability of the control loop is its phase margin. The phase margin is the phase of the open loop gain at the unity-gain frequency. In our example, the phase margin is about 45° . A phase of zero means that disturbances in the loop are

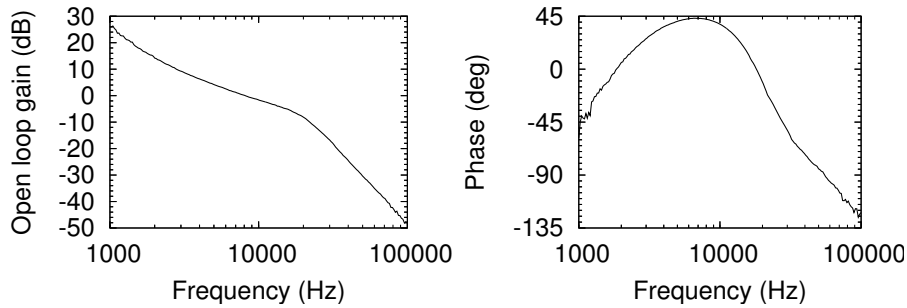


Figure B.3.: Bode plot of a frequency stabilization control loop. The plot shows the magnitude of the open loop gain in decibel and the corresponding phase on a linear scale. Unity gain frequency is approximately 8 kHz, the phase margin is approximately 45° and the gain margin is approximately 7 dB.

not counteracted, but fed forward. This situation is undesirable for control loops and the following rule of thumb has been proven useful.

To ensure stable and robust operation of the control loop, the phase margin should be 30° or more.

The so-called gain margin specifies the gain of the open-loop gain at the frequency with phase margin zero. The open loop gain of a control loop can at most be increased by the gain margin while ensuring stability of the loop. In Fig. B.3 the gain margin is approximately 7 dB.

In Abramovici and Chapsky (2000, p. 23) the effect of different phase margins is illustrated. Two control loops with the same unity gain frequency but with different phase margins (10° and 45°) are shown along with the response of the controlled variable to a unit step function command. With higher gain margin, the output follows the step function command with only a small overshoot while there is substantial overshoot and ringing in the case of small phase margin.

Gain and phase cannot however be designed independently from each other. To illustrate the connection between gain and phase a list of commonly used elements is listed in Table B.1. For every element, the transfer function and its Bode plot are shown. A real pole shows a flat transfer function for low frequencies and a roll-off with a slope of $1/f$ to higher frequencies. The phase shows lag zero at low frequencies and 90° phase lag at high frequencies. A complex pole shows a gain roll-off proportional to $1/f^2$ and 180° phase lag at high frequencies. A real zero shows a gain increase proportional to f and correspondingly a phase increase of 90° . Generally speaking, a gain roll-off results in a phase lag while increasing gain results in phase gain.

B.2. Control loop design

The task of designing a control loop includes choosing suitable actuators, finding a way to generate the error signal, and designing an appropriate loop filter. In Section B.2.1

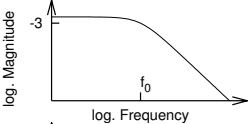
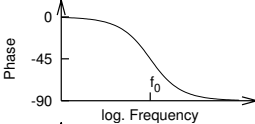
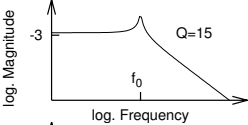
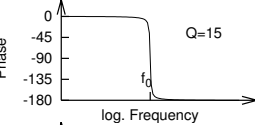
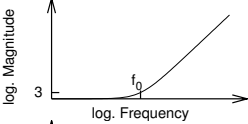
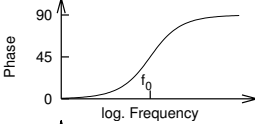
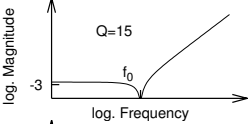
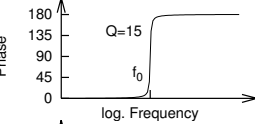
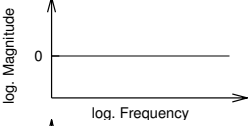
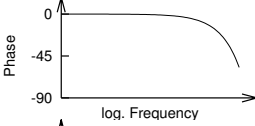
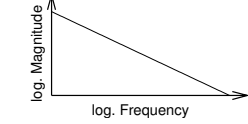
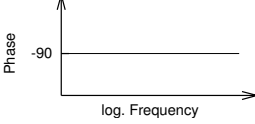
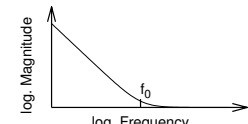
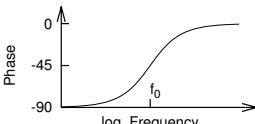
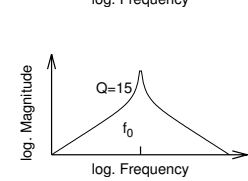
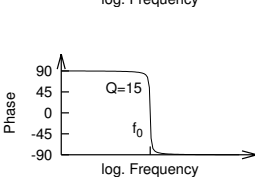
Element	Transfer function	Bode plot	
real pole	$H_{rp}(f, f_0) = \frac{1}{1 + \frac{if}{f_0}}$		
complex pole	$H_{cp}(f, f_0, Q) = \frac{1}{1 + \frac{if}{f_0 Q} - \frac{f^2}{f_0^2}}$		
real zero	$H_{rz}(f, f_0) = 1 + \frac{if}{f_0}$		
complex zero	$H_{cz}(f, f_0, Q) = 1 + \frac{if}{f_0 Q} - \frac{f^2}{f_0^2}$		
delay	$H_d(f, \delta) = \exp(-i\delta f)$		
integrator	$H_i(f) = \frac{1}{if}$		
damped integrator	$H_{di}(f, f_0) = \frac{1 + \frac{if}{f_0}}{if}$		
bandpass	$H_{bp}(f, f_0, Q) = \frac{if}{1 + \frac{if}{f_0 Q} - \frac{f^2}{f_0^2}}$		

Table B.1.: Transfer functions and Bode plots for a number of elements commonly employed in control theory.

commonly used actuators for frequency stabilization of nonplanar ring oscillators and actuators for power stabilization of lasers are presented. The remainder of this section focusses on the loop filter design.

The design of a loop filter requires the characterization of the control path. One method to do this is to calibrate the actuator signal and the error signal at DC. In the following Sections B.2.1 and B.2.2, calibration procedures for both signals are described.

In Section B.2.3 the loop filter design based on actuator and error signal calibration is described. In Section B.2.5 the design of an optimized loop filter that is based on the measurement of the transfer function from actuator signal to error signal as described in Section B.2.4 is discussed.

B.2.1. Actuator choice and calibration

Commonly used actuators for frequency stabilization of NPRO lasers are a PZT glued onto the laser crystal (Freitag, 1994; Kane and Cheng, 1988) that changes the laser frequency by stress-induced birefringence, a thermo-electric cooler that changes the overall laser crystal temperature, or pump power variations that locally change the laser crystal temperature and the laser inversion (Quetschke, 2003; Willke et al., 2000; Hunnekuhl, 2004).

A PZT glued onto the laser crystal is often used for fast frequency tuning, variations of laser crystal temperature are used to increase the dynamic range of the frequency stabilization. Pump current modulation has been used as an alternative to a PZT (Willke et al., 2000).

For power stabilization of NPROs the pump current is commonly used as actuator (Kane, 1990; Harb et al., 1994). External actuators for laser power stabilization are EOMs (Conti et al., 2000) and AOMs (Kasai and Ishizu, 1994).

To calibrate the PZT frequency actuator, i.e. to determine its efficiency η_{PZT} a signal ramp is applied to the actuator and the error signal response of the open control loop is monitored. By using markers in the error signal whose frequency difference is known and by measuring the voltage necessary to tune the laser frequency from one marker to the next, the PZT efficiency can be calculated. The type of markers used depends on the type of frequency stabilization setup the laser is used in: In the case of frequency stabilization to an optical cavity using the Pound-Drever-Hall scheme, the first sidebands provide good markers.

In a laser power stabilization setup the actuator efficiency can be measured by applying two different voltages to the actuator and measuring the corresponding laser output powers.

B.2.2. Error signal calibration

Valuable information can be obtained from the error signal of a control loop: if calibrated properly, the error signal spectral density yields a lower limit for the stability of the controlled signal. The important task of calibrating the error signal will be discussed for a frequency stabilization control loop. A commonly used actuator for a frequency

control loop is a PZT that changes the optical length of the NPRO laser cavity. A typical value for the PZT efficiency is $\eta_{\text{PZT}}=1.8 \text{ MHz/V}$. We will use this value as example in the following discussion.

A good estimate of the slope of the error signal can be obtained by applying a voltage ramp to the PZT actuator and monitoring the error signal. If the laser frequency is tuned appropriately so that the error signal slope is visible, then a good estimate for the error signal slope can be obtained using the known PZT efficiency.

Figure B.4 shows both the voltage ramp to the PZT actuator and the resulting error signal. In the example a PZT voltage range of 0.7 V is necessary to generate an error

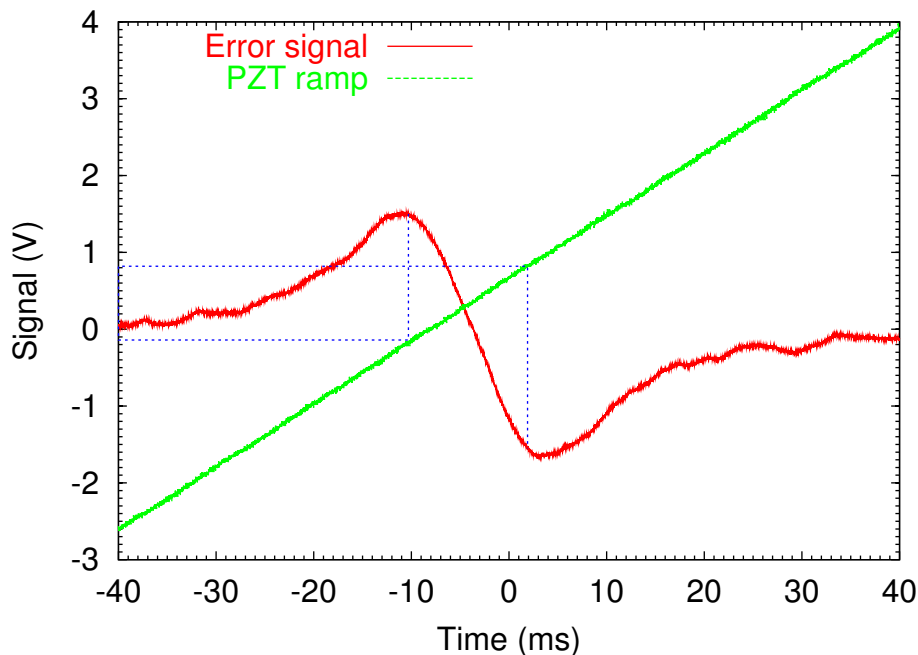


Figure B.4.: Signals used for estimation of the error signal slope in a frequency stabilization control loop; the voltage ramp is applied to the frequency actuator and the error signal is monitored.

signal difference of 2.5 V. With the knowledge of the PZT efficiency of 1.8 MHz/V the slope of the error signal is estimated to 2 V/MHz.

B.2.3. Loop filter design from little information

An optimized loop filter design requires the knowledge of the control path transfer function. Often, it is not possible to measure this transfer function (e. g. in laser frequency stabilization) without using a control loop. In those cases it is necessary to design and implement a loop filter from little information: actuator and error signal calibrations.

The procedure for such a design is sketched below:

1. Calibrate the actuator

2. Calibrate the error signal
3. Estimate the bandwidth available for stabilization
4. Calculate the desired transfer function of the loop filter

First, the actuator and the error signal are calibrated as described in the preceding sections. Let's assume, the PZT efficiency has been measured as $\eta_{\text{PZT}} = 1.8 \text{ MHz/V}$ and the error signal has a slope of $\beta_{\text{ES}} = 2 \text{ V/MHz}$. Now, the bandwidth available for a control loop needs to be estimated. Suppose, the PZT frequency actuator has a resonance at 100 kHz. Such a resonance can be modelled by a complex pole. From Table B.1 on page 115 it is visible that a phase lag of 180° is associated with such a resonance. This means that the bandwidth of a simple control loop cannot easily exceed 100 kHz in the example because the phase lag of the resonance would lead to zero phase margin. A good rule of thumb is to choose a bandwidth considerably below the PZT resonance frequency, e.g. 5 kHz.

With these figures, the transfer function H of the control path can be calculated to $H = 1.8 \text{ MHz/V} \cdot 2 \text{ V/MHz} \approx 3.6$ for frequencies below 100 kHz.

A good rule of thumb for designing control loops is

The open loop gain crosses unity gain with a slope of -20 dB per frequency decade and stays below unity gain for higher frequencies.

We choose an open loop gain of our control loop that is proportional to $1/f$ (-20 dB per frequency decade) with a unity gain frequency of 5 kHz. The open loop gain then reads

$$\text{OLG} = H \cdot G = \frac{5 \text{ kHz}}{f} \quad (\text{B.3})$$

From Eq. (B.3) we obtain the transfer function of our simple loop filter as

$$G = \frac{5 \text{ kHz}/H}{f}, \quad (\text{B.4})$$

which is an integrator.

B.2.4. Transfer function measurement

In most cases the error signal is proportional to the frequency deviation between laser frequency and reference frequency only in a small range around zero. In a well designed control loop only this linear regime around zero will be used for stabilization. When the error signal range used to calibrate the error signal exceeds this linear regime, the estimate obtained for the error signal slope does not yield the true value. The technique described in this section can be used to measure the error signal slope in the vicinity of zero. In addition, it yields the frequency dependent transfer function of the control path, which is necessary to know to design an optimized loop filter.

When the system is in lock with the simple loop filter designed in section B.2.3, a sinusoidal signal is inserted into the loop and its transfer function TF from the actuator point to the error point is measured. When the frequency dependent actuator efficiency η_{PZT} is known, the frequency dependent error signal slope β_{ES} can be calculated from the transfer function by Eq. (B.5).

$$\beta_{ES} = \frac{TF}{\eta_{PZT}} \quad (B.5)$$

When a PZT actuator is used, its efficiency does not depend on frequency below some corner frequency, in our example 100 kHz. When the current of the pump diode laser is used as frequency actuator, the corner frequency lies at a frequency below 10 Hz (Willke et al., 2000).

Figure B.5 shows the transfer function measurement schematically. Via an adder,

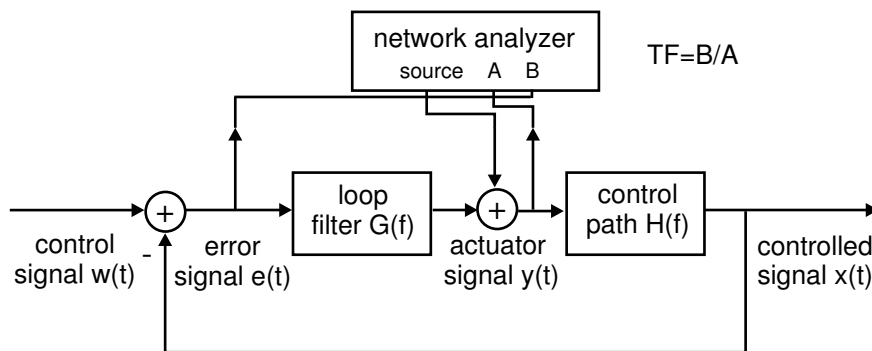


Figure B.5.: Method to measure the frequency dependent error signal slope within a control loop. When the system is in lock, a sinusoidal disturbance signal is added to the loop and the transfer function from the actuator point to the error point is measured.

a disturbance signal is inserted into the loop and its transfer function from actuator point to error point is measured using a network analyzer. The disturbance signal can be inserted anywhere in that part of the control loop that is not included in the path from actuator point to error point. Often, the actuator point or the error point are used to insert a disturbance signal.

B.2.5. Design procedure for optimized loop filters

Once it is possible to measure the control path transfer function, it is possible to design an optimized loop filter. Suppose, the transfer function shown in Fig. B.6 has been measured. It is flat for small frequencies and shows strong resonances between 70 kHz and 100 kHz. For low frequencies, the phase of the transfer function starts at zero. With increasing frequency, it “loses phase”.

This loss of phase and the resonances will be the limiting factors for the bandwidth of the control loop. We aim at a unity gain frequency between 10 kHz and 20 kHz. To

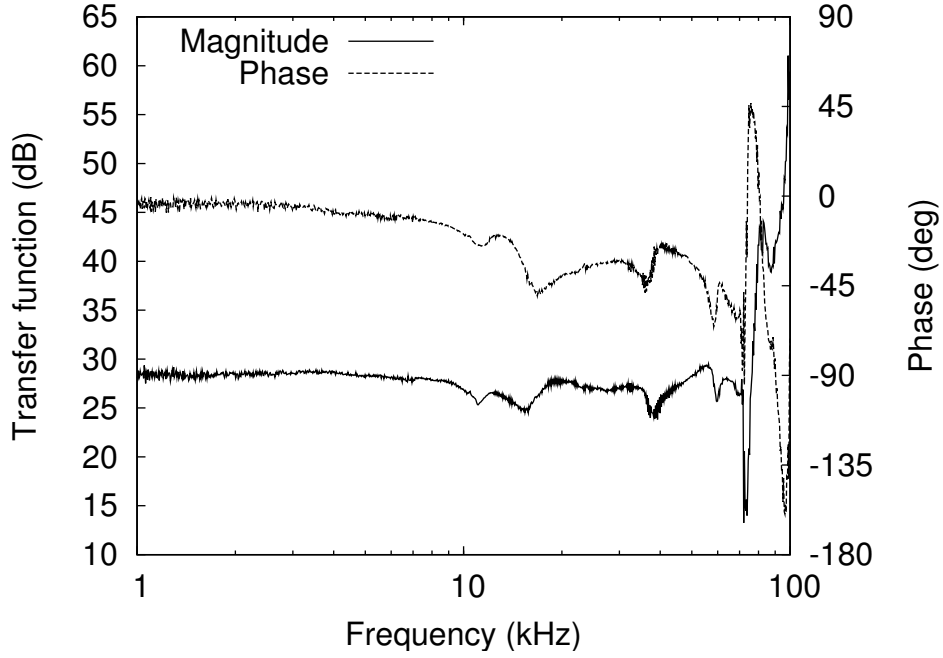


Figure B.6.: Measured transfer function of the control path.

achieve this, a low-pass filter is necessary that suppresses the PZT resonances. A two-pole low-pass filter ($Q = 1$) with a corner frequency of 20 kHz will be used. An integrator will be used to achieve the $1/f$ slope of the open loop gain around unity gain. To further increase the gain at lower frequencies, a damped integrator that rolls off at 100 Hz will be integrated. The resulting open loop gain is shown in Fig. B.7. The overall gain has been chosen so that a phase margin of 45° is maintained. A unity gain frequency of 10 kHz could be achieved.

Using the abbreviations defined in Table B.1 on p. 115 the transfer function of the loop filter can be written as

$$H(f) = 40000 \cdot H_{cp}(f, 20 \text{ kHz}, 1) \cdot H_i(f) \cdot H_{di}(f, 20 \text{ kHz}). \quad (\text{B.6})$$

B.3. Control loop characterization

Once a control loop has been built, its characteristics and its performance, i.e. its noise suppression, can be measured. We characterize a control loop by its complex open loop gain as described below. Noise suppression of a control loop is measured by giving a lower and an upper bound for the fluctuations in the controlled variable. The lower bound of noise is given by an in-loop noise measurement, the upper bound by an out-of-loop measurement.

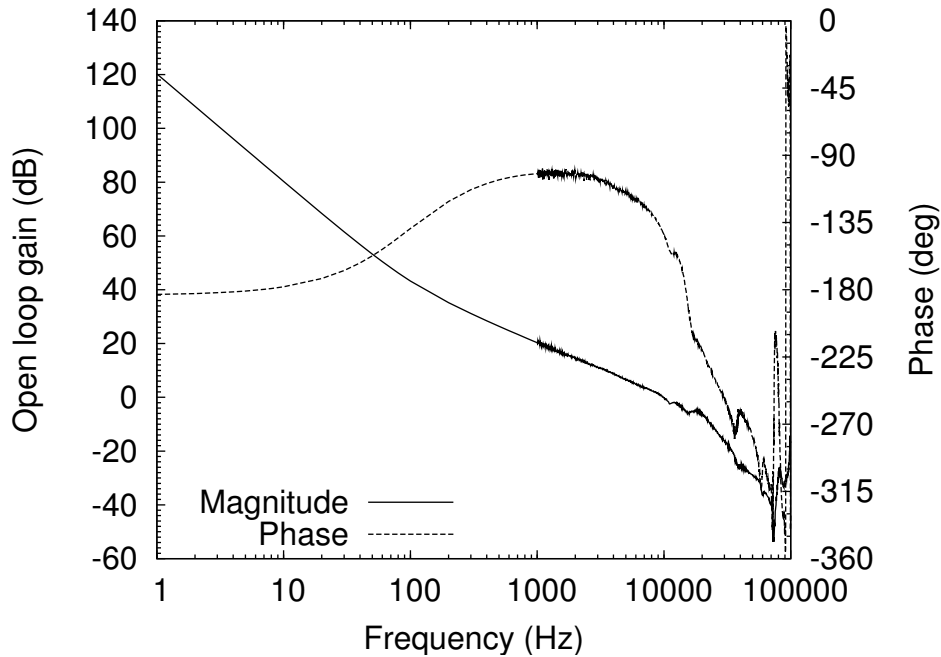


Figure B.7.: Open loop gain design based on the measured control path transfer function.

B.3.1. Open loop gain measurement

The open loop gain is defined as the gain of the open control loop. Hence, one method of measuring the open loop gain is to open the loop at an arbitrary point, insert a sinusoidal signal into the loop, measure the response at the other end of the loop and divide the response signal by the inserted signal.

Often, especially when the loop filter contains integrators, the open loop gain cannot be measured in this simple way. Due to the high gain of integrators, even small offsets would be integrated and lead to clipping. In laser frequency stabilization applications, often the error signal is only obtained in a frequency range smaller than the frequency noise of the free-running laser. This means that the open loop gain of the control loop cannot be measured with an open control loop. Instead, the control loop must be closed and working properly. Then the technique as shown in Fig. B.8 can be used to measure the open loop gain: We insert an adder at an arbitrary point within the control loop and use a network analyzer to insert a sinusoidal disturbance signal (while the control loop is in lock). To measure the open loop gain, the network analyzer divides the signal entering the adder from the loop (B) by the signal leaving the adder (A). It is easily verified that the open loop gain is given by B/A . It is important to note that the signal leaving the adder needs to be used, not the disturbance signal entering the adder from the network analyzer.

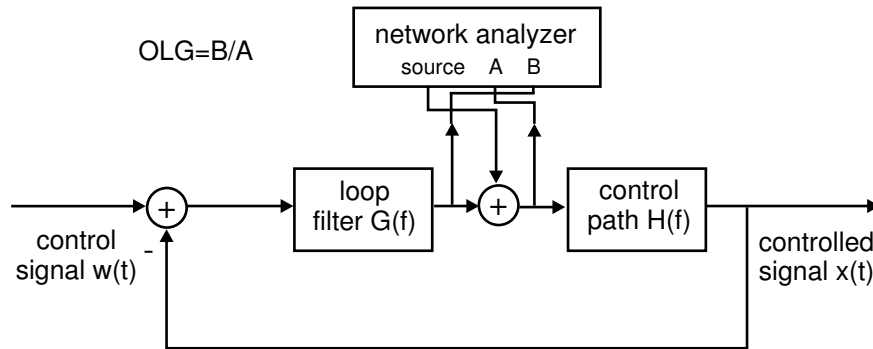


Figure B.8.: Scheme used to measure the open loop gain of a control loop.

B.3.2. In-loop noise as lower noise limit

The error signal in a control loop is a measure for the difference between control signal and controlled signal, for example reference intensity and laser intensity. Hence, we can use the in-loop error signal as lower limit for the noise of the controlled signal.

To obtain this lower noise limit we calibrate the in-loop error signal. In the case of laser intensity stabilization, the calibration factor would have units V/W . When the laser intensity is stabilized, we measure the error signal voltage noise spectral density, and divide by the calibration factor to obtain a spectral density in $W/\sqrt{\text{Hz}}$.

B.3.3. Out-of-loop noise as upper noise limit

The in-loop error signal does not measure noise in the reference signal nor noise that is inserted in the loop at the error point of the stabilization. To obtain an upper limit of the controlled signal stability, an out-of-loop measurement is required. One possibility is to generate a second, independent error signal. This method is commonly used in laser intensity stabilization. This out-of-loop error signal is calibrated and its voltage noise spectral density is measured while the control loop is working. Using the calibration factor, the voltage noise spectral density can be converted to an intensity noise spectral density. When the out-of-loop error signal is independent from the in-loop error signal, the instability of the controlled variable as measured by the out-of-loop error signal is an upper limit of the fluctuations.

Another, slightly different method that is commonly used in laser frequency stabilization applications, is to make a beat measurement between two identical, stabilized laser frequencies. When both stabilized lasers are independent, the frequency noise in the beat is an upper limit for the frequency noise of a single laser.

List of Publications

- Thesis Michael Tröbs. Light Sources for Spectroscopy. Master's thesis, University of Strathclyde, Glasgow, 1999.
- Michael Tröbs. Aufbau und Charakterisierung von neuartigen Mehrkristall-Festkörperlasern. Master's thesis, Universität Hannover, Hannover, 2000.
- Journal articles Markus Bode, Jens Meyer, Michael Tröbs, and Ingo Freitag. Hochstabile Nd:YAG Miniatur-Ringlaser im sichtbaren Spektralbereich mit aktiver Frequenzstabilisierung auf molekulares Jod. *Photonik*, 35:82–84, 2003.
- P. Burdack, M. Tröbs, M. Hunnekuhl, C. Fallnich, and I. Freitag. Modulation-free sub-Doppler laser frequency stabilization to molecular iodine with a common-path, two-color interferometer. *Opt. Express.*, 12:644–650, 2004. 27
- Ulrich Roth, Michael Tröbs, Thomas Graf, Jürg E. Balmer, and Heinz P. Weber. Proton and gamma radiation tests on nonlinear crystals. *Appl. Opt.*, 41:464–469, 2002.
- M. Tröbs, J. E. Balmer, and Th. Graf. Efficient polarized output from a unidirectional multi-rod Nd:YVO₄ ring resonator. *Opt. Commun.*, 182:347–442, 2000.
- M. Tröbs and Th. Graf. Compact, dual-configuration, single-frequency, Q-switched Nd:YAG laser. *Opt. Commun.*, 187:383–388, 2001.
- Michael Tröbs and Gerhard Heinzl. Improved spectrum estimation from digitized time series on a logarithmic frequency axis. submitted for publication to Measurement, 2004.
- Michael Tröbs, Peter Weßels, and Carsten Fallnich. Phase-noise properties of an Yb-doped fiber amplifier for LISA. accepted for publication in Optics Letters, 2004.

International conferences Th. Graf, M. Tröbs, J.-E. Balmer, and H. P. Weber. Unidirectional operation in a dual-configuration resonator with three Nd:YVO₄ rods. In *Conference Digest. 2000 Conference on Lasers and Electro-Optics Europe*, 2000.

M. Hunnekuhl, P. Burdack, M. Tröbs, U. Hinze, C. Fallnich, M. Bode, O. Dölle, I. Freitag, and K. Danzmann. Ultra-Stable Nd:YAG Ring Laser for a Space-Born LIDAR System. In *OSA Trends in Optics and Photonics (TOPS) Vol. 68, Advanced Solid-State Lasers, OSA Technical Digest*, pages WD3-1–WD3-3, 2002.

M. Tröbs and Th. Graf. Single-frequency or polarised output from dual-configuration resonators. In *Advanced Solid-State Lasers, OSA Technical Digest*, pages 119–121, 2001.

M. Tröbs, M. Hunnekuhl, P. Burdack, U. Hinze, C. Fallnich, M. Bode, I. Freitag, S. Skorupka, G. Heinzl, and K. Danzmann. Highly stable laser towards spaceborne gravitational wave detection - towards a new window into space. In *2002 Conference on Lasers and Electro-Optics*, 2002a.

M. Tröbs, M. Hunnekuhl, P. Burdack, U. Hinze, C. Fallnich, S. Skorupka, G. Heinzl, K. Danzmann, M. Bode, and I. Freitag. Beat measurements of single-frequency lasers independently frequency-locked to thermally shielded high-finesse cavities. In *OSA Trends in Optics and Photonics (TOPS) Vol. 68, Advanced Solid-State Lasers, OSA Technical Digest*, pages WD4-1–WD4-3, 2002b. 42

Curriculum vitae

Personal details

Name	Michael Tröbs
Date of birth	March 1st, 1976
Place of birth	Hannover, Germany
Nationality	German

Education

1982–1986	Primary school Wennigsen
1986–1988	Orientierungsstufe Wennigsen
1988–05/1995	Ganztagsgymnasium Barsinghausen
1995	Abitur

University education

10/1995–11/2000	Physics at University of Hannover, Germany
09/1998–09/1999	MPhil course at University of Strathclyde, Glasgow, thesis: “Light sources for spectroscopy”
11/1999–10/2000	Diploma thesis at University of Bern, thesis: “Aufbau und Charakterisierung von neuartigen Mehrkristall-Festkörperlasern”
06/2000	Master of Philosophy, University of Strathclyde
11/2000	Physik Diplom, Universität Hannover

Grant

09/1998–09/1999	Grant of the European Mobility Scheme for Physics Students
-----------------	------------------------------------------------------------

Work experience

Feb. 2001–now	Scientific employee at Laser Zentrum Hannover e. V. Germany
May 2002–now	Collaboration with Innolight GmbH

Danksagung

An dieser Stelle möchte ich allen danken, die in verschiedener Weise zum guten Gelingen dieser Arbeit beigetragen haben, auch wenn sie nicht alle explizit erwähnt werden.

Meinem Doktorvater Prof. K. Danzmann danke ich für die Betreuung der Dissertation und sein stetes Interesse an dieser Arbeit. Bei Priv. Doz. H. Lubatschowski bedanke ich mich für die bereitwillige Übernahme des Korreferates. Bei Priv. Doz. C. Fallnich bedanke ich mich für die Möglichkeit, einen großen Teil dieser Arbeit am Laser Zentrum Hannover e. V. (LZH) durchführen zu können, seine stete Diskussionsbereitschaft und die hilfreichen Anregungen zu dieser Arbeit. Von Dr. Gerhard Heinzl habe ich viel gelernt. Neben Einsichten in die Welt der Elektronik, Laserstabilisierung und Interferometrie entstand der LPSD-Algorithmus im Rahmen einer Diskussion mit ihm. Für seine exzellente, nicht nur fachliche Betreuung über Institutsgrenzen hinweg bedanke ich mich herzlich.

Bei allen jetzigen und ehemaligen Kollegen der Abteilung Laserentwicklung des LZH bedanke ich mich für die gute Zusammenarbeit und das gute Arbeitsklima. Bei Dr. Peer Burdack, Dr. Ulf Hinze und Dr. Michael Hunnekuhl bedanke ich mich für Unterstützung und die angenehme Zusammenarbeit innerhalb der „Space-Gruppe“. Teile der hier vorgestellten Arbeit entstanden, während ich an die Firma Innolight „ausgeliehen“ war. Für die gute Zusammenarbeit bedanke ich mich bei allen dortigen Kollegen, insbesondere bei Dr. I. Freitag und Dr. M. Bode. Die Experimente zur Frequenzstabilisierung wurden in Laboren des Max-Planck-Institutes für Gravitationsphysik durchgeführt. Bei den dortigen Kollegen bedanke ich mich für das gute Arbeitsklima, das bereitwillige Zusammenrücken im Büro und die freundliche Aufnahme des „Gastforschers“.

Die Zusammenarbeit in den Kellerlaboren mit Sascha Skorupka gestaltete sich angenehm und produktiv, auch bis tief in die Nacht vor wichtigen Projekttreffen. Bei Frank Seifert bedanke ich mich für die gelungene Zusammenarbeit, seine guten mechanischen und elektronischen Arbeiten im Rahmen des Fotodiodenmessplatzes und hilfreiche Diskussionen, nicht nur zu Fotodioden, Elektronik und Leistungsstabilisierungen. Frank Steiers Thermalkammer ermöglichte die temperaturabhängige Vermessung von Spiegelreflektivitäten. Bei Dr. Peter Weßels bedanke ich mich für das gemeinsame angenehme und effiziente Forschen am LZH und viele hilfreiche Diskussionen. Er gab mir Einblicke in die Welt von Faserverstärkern, deren Frequenz nur sehr wenig aber messbar rauscht. Bei Dr. Dietmar Kracht bedanke ich mich für gute Ratschläge sowohl im Rahmen dieser Arbeit als auch außerhalb. Ich schätze seine Art, die Gruppe „Solid State Photonics“ am LZH zu leiten.

Für das Korrekturlesen der Arbeit oder Teilen von dieser bedanke ich mich bei Dr.

D. Kracht, M. Botts, PD. C. Fallnich, M. Frede, Dr. G. Heinzl, F. Seifert, S. Skorupka, Dr. D. Wandt, R. Wachter und Dr. P. Weßels. Durch ihre Unterstützung hat die Arbeit einiges an Qualität gewonnen.

Meine Eltern und meine (gar nicht mehr so kleine) Schwester waren immer für mich da und haben mich gestärkt. Sandra, die seit kurzem mein Leben bereichert, hat mich auch in stressigen Zeiten motiviert und unterstützt.

Herzlichen Dank!